UNIVERSITÀ
DEGLI STUDI
FIRENZE

DIEF - Dipartimento di Ingegneria Industriale

PhD School: *Energetica e Tecnologie Industriali e Ambientali Innovative*

Scientific Area: ING-IND/09

Experimental Investigations of Effusion Cooling Systems for Lean Burn Aero-Engine Combustors

PhD Candidate: Ing. Alessio Picchi

Tutor: Prof. Ing. Bruno Facchini

Academic Relator: Dr. Ing. Lorenzo Tarchi

Industrial Relator: Ing. Fabio Turrini

PhD School Coordinator: Prof. Ing. Maurizio De Lucia

PhD School Cycle: XXVI (2011-2013)

to Irene
my sweetheart

Acknowledgements

First, I would like to express my gratitude to Prof. Bruno Facchini, for his support, the faith he put in me during these last years and for the wonderful study opportunity he offered to me.

I would acknowledge Ing. Fabio Turrini, for his competence and for his precious and motivating advices. It was a pleasure to work with you, thank you!

I would also like to thank Dr. Lorenzo Tarchi not only for his wise suggestions but more importantly for his friendship. In these years, thanks to your support, we have dealt great challenges without dread (one for all, do you remember the "frozen" experimental campaign in November 2011? I don't believe yet, we got results!).

I feel in debt with my friend Gianluca, I have shared with you good and bad times during our Ph.D. course. Despite the difficulties, together we never lost hope and now we see the finish line!! For the time spent together in THT Lab working, discussing and (often!) loosing patience; and above all for your friendship that will continue in the years: thank you very much Gianlu!

The reported work was performed within the European Projects KIAI (Knowledge for Ignition, Acoustics and Instabilities) and LEMCOTEC (Low Emissions Core-Engine Technologies). The author wish to gratefully acknowledge the Consortia for the kind permission of publishing results herein and especially for the opportunity of participating in such works. KIAI and LEMCOTEC are Project co-funded by the European Commission within the Seventh Framework Programme

Many thanks are for all my colleagues and friends that have made every day the office environment more pleasant: Alessandro, Alessio, Andrea, An-

tonio (..for his support and unbounded competence, a leading figure in these years), Carlo, Charlie (..wonderful and unforgettable memories with you in THT Lab! thank you little French!), Cosimo, Daniele, Francesco "Fransis", Leonardo, Lorenzo M., Lorenzo W., Luca, i'Maio (my front desk colleague in "Colonne", wonderful memories with you and the other "experimental" guys thank you!), Marchino, Mirko, Riccardo "RDS", Riccardo B. (thanks to you and to your thesis!!), Riccardo F. and Tommy.

Finally, I'm really grateful to my family, to Irene and to my friends to support me during these unforgettable years; I could have never achieved my objectives without you!

Per me si va ne la città dolente,
per me si va ne l'etterno dolore,
per me si va tra la perduta gente.

Giustizia mosse il mio alto fattore;
fecemi la divina podestate,
la somma sapienza e 'l primo amore.

Dinanzi a me non fuor cose create
se non etterne, e io etterno duro.
Lasciate ogne speranza, voi ch'intrate

Dante Alighieri, Divina Commedia (Inferno, Canto III)

Contents

Nomenclature

Letters

Bi	Biot number	$[-]$
BR	Blowing Ratio	$[-]$
C	Concentration mass fraction	$[-]$
C_d	Discharge Coefficient	$[-]$
d	Hole diameter	$[m]$
D	Mass Diffusion Coefficient	$[m^2/s]$
d	Hole diameter, PIV particle size	$[m]$
DR	Density Ratio	$[-]$
G	Mass flux per unit of area	$[kg/sm^2]$
HTC	Heat transfer coefficient	$[W/(m^2K)]$
I	Intensity	$[counts]$
I_{el}	Current flow	$[A]$
l	Length	$[m]$
l_{ref}	Reference dimension	$[-]$
Le	Lewis Number	$[-]$
k	Thermal conductivity	$[W/mK]$
MR	Momentum Ratio	$[-]$
Nu	Nusselt number	$[-]$
$NHFR$	Net Heat Flux Reduction	$[-]$
P	Pressure	$[Pa]$
Pr	Prandtl Number	$[-]$
$\dot{q}$	Area Specific Heat flux	$[W/m^2]$
R	Electric resistivity	$[\Omega]$

S_n	Swirl number	$[-]$
S_x	Stream-wise pitch	$[m]$
S_y	Tangential pitch	$[m]$
Sc	Schmidt number	$[-]$
St	Stokes Number	$[-]$
T	Temperature	$[K]$
U	Velocity	$[m/s]$
V	Voltage	$[V]$
VR	Velocity Ratio	$[-]$
W	Molecular weight	$[kg/kmol]$

Greeks

α	Hole inclination angle	$[deg]$
ϵ	Turbulent Diffusivity	
θ	Dimensionless Temperature	$[-]$
η_{ad}	Adiabatic Effectiveness	$[-]$
η_{ov}	Overall Effectiveness	$[-]$
ρ	Density	$[kg/m^3]$
ρ_{el}	Electric Resistivity	$[\Omega m]$

Subscripts

ad	Adiabatic case
$c; cool$	Coolant
$conv$	Convective
$dark$	UV lamp switched off
eff	Effusion
fg	Foreign gas
$Joule$	Joule Effect
$main$	Mainstream, gas side
ref	Reference condition
s	Static

T	Turbulent
t	Total
w	Wall

Acronyms

AFR	Air-Fuel Ratio
$ACARE$	Advisory council for Aeronautical Research in Europe
$CAEP$	Committee on Aviation Environmental Protection
$CSTR$	Cold Sector Test Rig
$ICAO$	International Civil Aviation Organization
IRZ	Inner Recirculation Zone
LDI	Lean Direct Injection
LP	Lean Premixed
LPP	Lean Premixed Prevaporized
NO_x	Nitrogen oxides
OPR	Overall Pressure Ratio
PIV	Particle Image Velocimetry
$PERM$	Partially Evaporated and Rapid Mixing
PSP	Pressure Sensitive Paint
$PMMA$	Poly-Methyl Methacrylate
PVC	Processing Core Vortex
RCZ	Recirculation Zone
TC	Thermocouple
TLC	Thermochromic Liquid Crystal
TRL	Technology Readiness Level

Abstract

Legislation limits concerning polluting emissions, for civil aircraft engines, are expected to become even more stringent in the future. To meet these targets, especially in terms of NOx, it is required to maintain the temperature in the combustion zone as low as possible. Lean burn swirl stabilized combustors represent the key technology to reduce NOx emissions. The high amount of air admitted through a lean-burn injection system is characterized by very complex flow structures such as recirculations, vortex breakdown and processing vortex core, that may deeply interact in the near wall region of the combustor liner. This interaction and its effects on the local cooling performance make the design of the cooling systems very challenging. In addition, since up to 70% of the overall air mass flow is utilized for fuel preparation and the initiation of lean combustion, the amount of air available for combustor liner cooling has to be strongly reduced with respect to the traditional diffusive combustor architectures.

State-of-the-art of liner cooling technology for modern combustors is represented by the effusion cooling. Effusion cooling is a very efficient cooling strategy based on the use of multi-perforated liners, where metal temperature is lowered by the combined protective effect of coolant film and heat removal through forced convection inside each hole. Beyond that, multi-perforated liners act also as passive devices to mitigate thermoacoustic phenomena which is one of the main concern regarding lean combustors operability.

A large part of the activities and the achievements deriving from the Ph.D. course are collected in the present study, that deals with two experimental campaigns on effusion cooling schemes designed for aero-engine

combustor liner applications.

In the first part of the current research, an experimental survey has been performed for the evaluation of thermal performance, in terms of overall and adiabatic effectiveness, of seven multi-perforated planar plates representative of a portion of combustor liner, with uniform mainstream conditions. Effusion geometries were tested imposing 6 blowing ratios in the range 0.5-5, two values of density ratio and two level of mainstream turbulence. Concerning the geometrical features, different porosity levels have been considered: such values are obtained both increasing the hole diameter and pattern spacing. Then, the effect of hole inclination and aspect ratio pattern shape have been tested to assess the impact of typical cooling system features. The analysis of the data points out the impact of the main geometrical and fluid dynamics parameters on the thermal performance, proposing a possible thermal optimization strategy that seems to be promising also from the acoustic damping requirements. Results represent a wide experimental database relevant for the design of an high efficiency effusion cooling systems, even though the survey leaves the impact of the swirled gas flow on thermal performance an open issue.

To enhance the TRL (Technology Readiness Level) of experiments, a planar sector test rig equipped with three AVIO Aero PERM (Partially Evaporated and Rapid Mixing) injector systems and working at atmospheric conditions has been considered in the second part of the work. The test rig allowed to reproduce a representative flow field on the gas side and to test the complete liner cooling scheme composed by a slot system, that reproduced the exhaust dome cooling mass flow, and an effusion array. The final aim of the study is the experimental characterization of the flow field and the measurement of cooling performance in terms of heat transfer coefficient and adiabatic effectiveness due to the interaction of the swirling flow coming out from the injectors and the cooling scheme. Tests were carried out imposing several realistic operating conditions, especially in terms of reduced mass flow rate and pressure drop across swirlers and effusion cooling holes.

Detailed bidimensional maps of heat transfer coefficient have been obtained with a steady-state technique, using TLC (Thermochromic Liquid Crystals) in a wide band formulation; while adiabatic effectiveness distributions have been obtained using the PSP (Pressure Sensitive Paint) technique, based on heat and mass transfer analogy. This technique has been developed and tuned by the author within the Ph.D. course.
Local values of overall effectiveness have been measured through steady state conductive tests using thermocouples embedded in the test samples. Regarding the flow field generated by the PERM injectors, it has been investigated by a 2D PIV (Particle Image Velocimetry) analysis performed on several measurements planes.

The activities reported in the present work were carried out within the European Research Projects KIAI (Knowledge for Ignition, Acoustics and Instabilities) and LEMCOTEC (Low Emissions Core-Engine Technologies), both belonging to European Union 7^{th} Framework Programme in which the University of Florence is the scientific partner of AVIO Aero.

Chapter 1

Technical Background

1.1 Development of Modern Aero-engine

In the next twenty years the global air traffic is forecast to grow at an expected annual rate of about 5% [1] in order to support the future world economy envisioned to be increasingly global with diffused national boundaries. The high level of growth makes the environmental impact of the air traffic relevant, moreover from an economical point of view the aviation sector becomes strategic drawing investments. Consequently, aircraft manufacturers have to cope with hard technological challenges to satisfy the demand of economic, environmental friendly and safe aero-engines.

Even if the current aero-engines state of art (Fig. 1.1) allows to make a marginal improvement of performance, especially in terms of their pollutant emissions, they might not allow to strict the goals set by ACARE (Advisory council for Aeronautical Research in Europe [2]) by the 2020.
In the last years, several European Research Projects, such as NEWAC[1], have been carried out focussing on development and validation of novel core engine configurations [3], in order to provide a breakthrough in thermal efficiency and to achieve a significant and permanent reduction of pollutant emissions. Among them, the most promising configurations are the "*Inter-cooled core*" and the "*Inter-cooled Recuperated core*" solutions (Fig.1.2).

[1]NEW Aero-Engine Core concepts

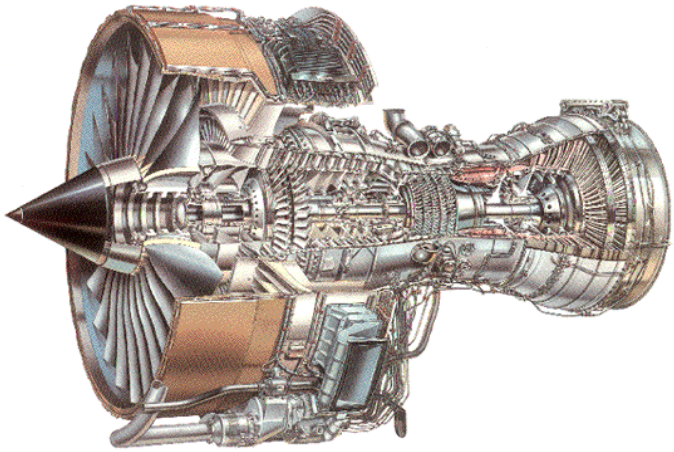

Figure 1.1: Example of the current state of the art of large turbofan[2]

Currently, the required technologies such as the heat exchanger systems, necessary to manufacture the core solutions reported above are not enough mature and further research and development are still necessary. In the short terms, as required by the ACARE targets, the only feasible way to increase the engine efficiency is to develop core engine technologies, including combustion systems, that work with overall pressure ratio (OPR) up to 50 for regional turbofan and 70 for large turbofan, adopting conventional gas turbine cycle. The current state of the art of aero-engine for regional and large turbofan is, respectively, a working OPR of 35 and 38.
In a second phase, around 2030 and later, when novel technologies such inter-cooling will become feasible, after further demonstrations, it could be

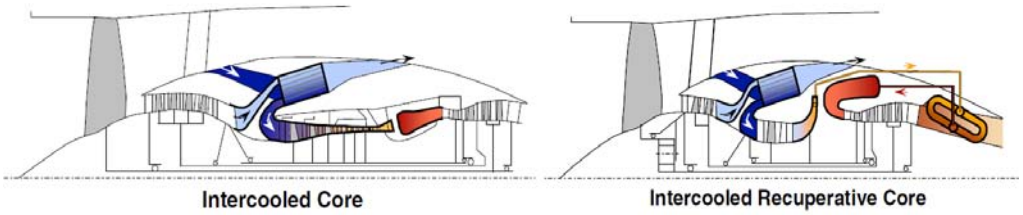

Figure 1.2: Example of novel Aero-Engine concepts [3]

[2]http://www.jet-engine.net/

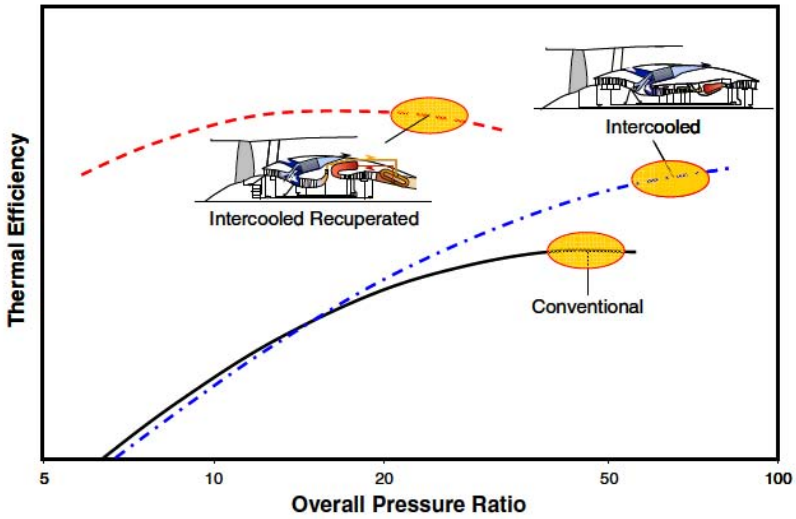

Figure 1.3: Effect of OPR on thermal efficiency for conventional and innovative core-engine [3]

integrated in high OPR thermodynamic cycle in order to achieve a significant improvement in fuel consumption and pollutant emissions as demonstrated in Fig. 1.3.

1.2 Pollutant Emissions and Novel Combustion Systems

In the last decades, the environmental effects issue of air traffic has gained the attention of public eye. Since 70's, the concerns regarding the toxicity of pollutant emissions and the impact of green house effect have make sensitive the industrial manufactures putting in action efforts to research environmental friendly solutions.

The exhaust gas of an aero-engine consists of different gaseous species and particulate material. In addition to the gasses that compose the portion of air not participating to the combustion process, the exhaust gas is constitute to different species causing different impact on environment. CO and NO_x are toxic species that cause acid rain and the depletion of ozone

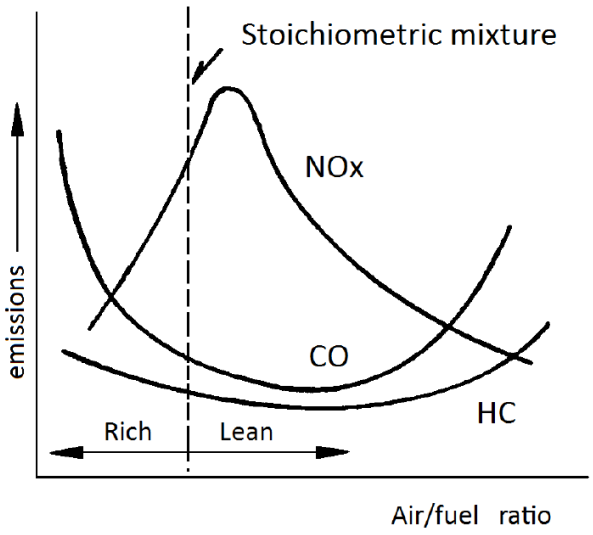

Figure 1.4: Dependence of NO_x, UHC and CO emission varying the air fuel ratio

in the stratosphere. Unburned hydrocarbons and smoke produce respiratory diseases, while carbon dioxide contributes to the green house effect.

For commercial aircraft, the effort of the industrial and scientific community is mainly aimed at reducing the CO and, most of all, NO_x as it is considered the major and more pressing target of the ICAO-CAEP standards. They imposed a reduction of nitrous oxides emissions with a target of 80% abatement by the next 2020.

The total amount of gas emission is, of course, directly linked to the global efficiency of the aero engine including the thermodynamic efficiency as well as the airframe drag. As discussed in the previous section, the forecast trend of engine thermal efficiency for the future aero engines is expected to significant growth helping the reduction of pollutant emission, this is true especially in terms of carbon dioxide emission. However a breakthrough in NO_x emission can be accomplished only acting on the combustion process.

The emission of NO_x varying the air-fuel ratio (AFR) is in contrast with the CO and UHC trend as reported in Fig. 1.4 lower the UHC and CO concentrations, higher the NO_x and vice-versa. This behaviour is due to the

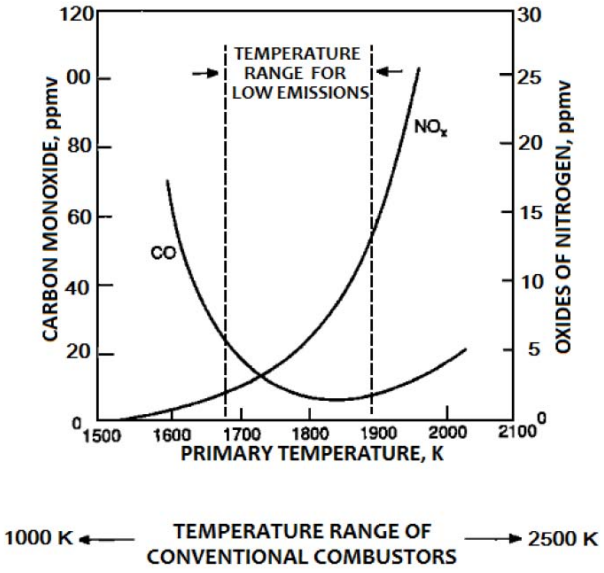

Figure 1.5: Temperature range to reduce both NO_x and CO emissions

fact that the production of nitrous oxides is maximum near the stoichiometric condition where the temperature reach a maximum: as demonstrated by the work of Zeldovich et al. [4] the predominant contribution to NO_x generation, comparing to the others [5], is due to the well know *Zeldovich Thermal* NO_x mechanism. It foresees that the NO_x production depends exponentially on the combustion temperature. On the other hand, UHC and CO which have roughly the same behaviour, are generated by lean or rich mixture with incomplete combustion.

To overcome this opposite behaviour, one of the way to reduce the NO_x production without increase the UHC and CO is to realize combustion system able to operate in the temperature range where a trade-off of the aforementioned species is achieved, as depicted in 1.5. One of the feasible solution to control the combustion temperature is to develop combustion systems operating with premixed flame. For this purpose, the industrial manufacturers are prompting several research programmes to develop LP (Lean Premixed) combustors equipped with innovative injectors that are currently considered the technology with the potentiality to match the targets in terms of NO_x

abatement [6], especially for aero-engines with high OPR and standard thermodynamic cycle which represents the future of aircraft in the short term. It is worth to notice that in core-engines without inter-cooling technology integrated in the compression system, the compressor delivery temperature increases with OPR. The increased pressure in core-engines poses a substantial challenge for the NO_x emission reduction: measures must be taken to mitigate the negative effects due to the rise in compressor delivery temperature and consequently turbine entry temperature that lead to a natural increase of NO_x. This issue must be addressed to avoid eroding the cycle benefit gained by the higher OPR, and it ask additional efforts to LP combustors to limit pollutant emissions.

1.3 Lean Premixed Technology

Gas turbine engines were initially developed with combustion systems that work with diffusion flame because of their reliable performance and compactness. Unfortunately, these type of combustor chambers produce high level of NO_x emissions through the Zeldovich thermal mechanism due to the high temperature reached in the combustion zone ([7]).

Currently, the main standard for aero-engines combustion systems with liquid fuel is the RQL technology (*Rich-Burn Quick-Quench Lean-Burn*), introduced as a results of a specific program for pollutant emission reduction [8]. RQL technology consists in burning a rich mixture in the primary zone with an operating equivalence ratio between about 1.2 and 1.6. The airstream flowing from the rich primary zone is thus high in concentration of UHC and CO and can not be exhausted without further processing. For this purpose, in the second region, referred to as quench zone, a substantial amount of air is injected through wall jets to create a lean mixture prior the exit plane of the combustor. Finally, complete combustion in the last lean burn region is achieved. The main drawback on adopting RQL technique is the soot formation and incomplete mixing between fuel-rich combustion products and air that hamper further development of this technology [9].

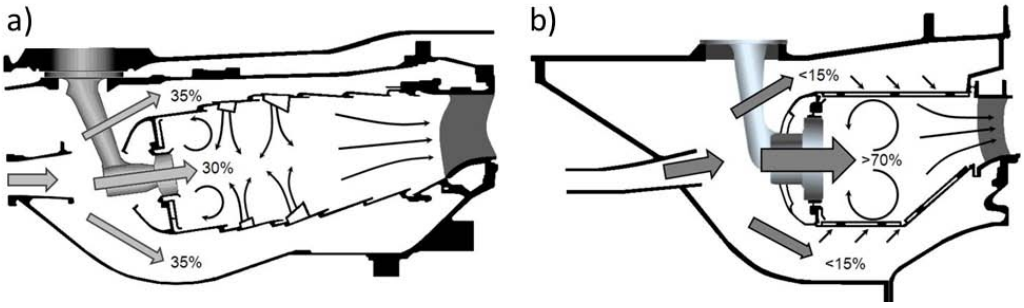

Figure 1.6: Air flow split and layout of conventional (**a**) and lean combustors (**b**) [10]

Demands for decreasing NO_x emissions, as prescribed by strict regulations, while increasing thermal performance, have prompt manufacturers to design of advanced and novel combustors able to overcome the limits of RQL approach. One of the most promising technology is the *Lean Premixed* in which the object of the design is to provide an homogeneous air/fuel mixture for the combustion zone at an AFR close to the lean blow out. A homogeneous mixture with high AFR guarantees a low combustion temperature limiting the hotspots due to rich fuel pockets.

On the other hand, if the NO_x are significantly reduced keeping low the combustion temperature, the concentration of CO increases with low burning temperature and low resident times in the flame tube: the results is an inefficient oxidation to carbon dioxide determining a limitation to mixture leanness as extensively reported by Correa [11]. In LP combustor the control of CO emission is implemented by an accurate design of combustor aerodynamics. The turbulence structure and the recirculation zones play a key role in the emission control; they alter the resident time and improve the mixing of burnt mixture favouring the gas oxidation.

In LP combustors most of the flow rate coming from the last stage of compressor is used to prepare the fuel-air mixture entering in the flame tubes through the injector systems (Fig. 1.6): indeed, the air flow split that affects directly the flame to is growth from about 30%, in the standard diffusive combustors, up to 70% in the new architectures [10]. One of the main drawback of the novel architecture is that the larger amount of air injected directly

with the fuel, deeply reduces the availability of air for dome and liner cooling requiring novel cooling systems to protect the combustor components.

The Lean Premixed technology was originally developed for gas turbines for land applications where the requirements in term of NO_x abatement were even more stringent respect to the legislation in force in the past for aircrafts. The application of this technique for land-based applications was supported by the use of gaseous fuels for which the major concern is to obtain an optimal level of mixing among the air, fuel, and combustion products in the combustion zone. On the other hand, when liquid fuels are employed, as strictly required for aero-engines, the application of the Lean Premixed technology is placing future challenges. To achieve an effective reduction of the pollutant emissions, liquid fuels must be accurately atomized into small droplets and then distributed in an air stream before entering the combustion zone.

Since the liquid fuel atomization, as required in aircrafts, and the mixture preparation play a key role to limit NO_x emissions, one of the most critical components in the design of novel combustor chambers is the fuel injector. There are several types of injectors, among them there are three technologies that have showed good performances: *Lean Pre-Mixed Pre-vaporized* (LPP), *Lean Direct Injection* (LDI) and finally the *Partially Evaporated and Rapid Mixing* (PERM) injector.

LPP injectors are technology developed in the past for engines that work at low OPR condition. Their working principles is based on the action of two distinct air flow: the first is used primarily to get a good liquid fuel atomizations, while the second is devoted to mix the fuel with air stream promoting the fuel evaporation and creating a mixture as much as possible uniform. Despite the interaction of the two air streams acts as a promoter for flame stabilisation, the main drawback of this type of injector is the combustor instabilities (Dhanuka et al. [12]) characterized by large amplitude pressure oscillations sustained by fluctuating heat release that causes a reduction of the life of combustor components. In addition they have poor performance in terms of altitude relight, a feature required for aircraft applications: the time required for vaporisation and mixing in the fuel preparation duct can

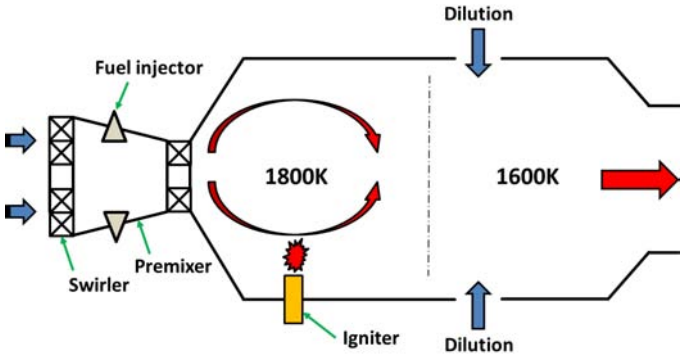

Figure 1.7: Schematic of an LPP combustor

exceed the autoignition delay time at high power. This might cause in some operating conditions the migration of the flame downstream conditioning the safe operability of the combustor (Brandt et al. [13]). A schematic layout of LPP combustor is reported in Fig. 1.7.

LPP combustors generally employ pilot combustion stages generally used at critical working conditions, such as at part load, when incomplete combustion phenomena can occur due to the low combustion temperatures. Finally, a dilution flow is usually placed near the combustor exit; it used to condition the temperature profile and to arrest the NO_x production. Nevertheless, in some operating range this flow can inhibit the fully conversion of CO in CO_2, lowering the combustor efficiency and increasing the level of pollutant emission. The NO_x and CO production balance is one of the major aspects that designer have to face off (Lazaro et al. [14]). Another major problem of the LPP combustors, documented in the current literature, is the flashback phenomena into the premix duct which usually takes place when locally the flame speed is faster than the velocity of the air-fuel mixture (Fritz et al. [15]).

From the analysis, it is clear that the LPP technology has serious operational risks for its application on aircraft especially for large turbofan that will operate at very high OPRs. Narrow stability range, thermoacoustic phenomena and flashback undercut the necessary safety requirements for its application in future aero-engines. However LPP combustors is nowadays

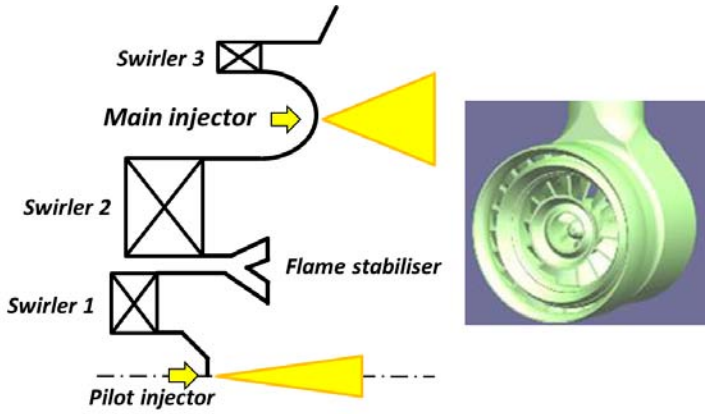

Figure 1.8: Schematic of an LDI injector [3]

widely used for land application due to its capability to easily reduce NO_x production with gaseous fuel.

With the aim to overcome the issues highlighted for the LPP combustors, recently the combustor designers have developed new type of injector based on the *lean direct ignition* (LDI) technology. These type of injectors would mitigate the limitation imposed by LPP combustors such as flashback and design complexities; here the fuel is directly introduced in the combustion test section where it is subjected to rapid mixing with the combustor air. In addition to its ability to limit flashback, studied have shown low level of NO_x emission and higher combustion efficiency compared to the LPP injector, making this technology attractive for aircraft applications (Cooper and Laurendeau [16]).

A schematic of on LDI injector is reported in Fig 1.8, the main feature is the internal controlled premixing of air and fuel stream achieved using two internally staged and concentric fuel injection at high pressure and at an equivalence ratio close to the lean blow-out limit. There is no premixing duct attached upstream the flame tube and the fuel air mixing is promoted using three different axial swirlers. The objective is to enhance the mixing process and to generate more turbulence to rip apart the liquid fuel streams in order to guarantee that the fuel-air mixing takes place in the shortest pos-

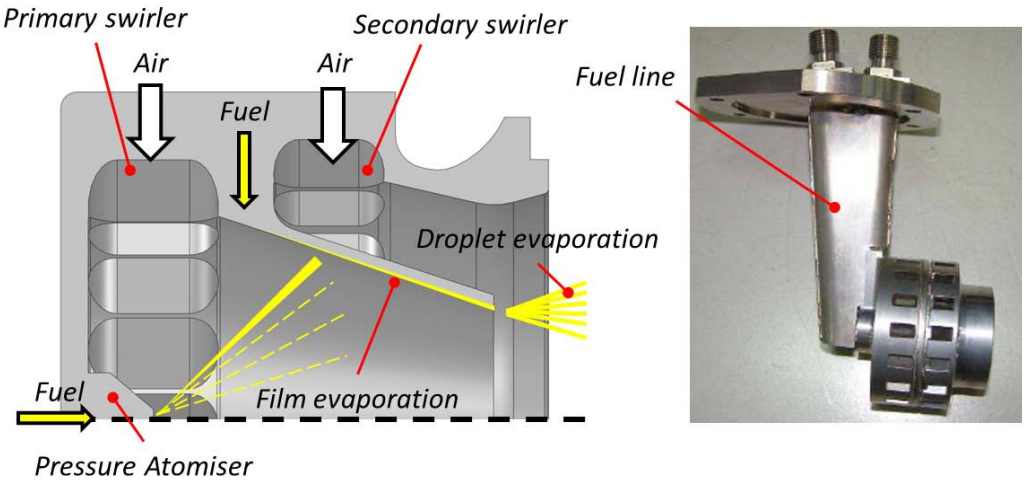

Figure 1.9: Schematic of a PERM injector[3]

sible distance. In addition, as the fuel is not premixed and pre-vaporized, to keep low the flame temperature and to avoid hot spots it is important to achieve a fine atomization of the fuel. A bluff body placed between the first two swirlers is used to anchor and stabilize the flame. Several authors have demonstrated its potential in terms of low-NOx production (Anderson [17]; Alkabie et al. [18]; Shaffer and Samuelsen [19]; Terasaki and Hayashi [20]).

In order to improve the mixing reducing the distance over which the fuel and the fresh air need to be mixed, a possible solution is to break up a few large of injectors into many smalls (Tacina et al. [21]; Cai et al. [22]). This expedient speed-up the mixing and makes the combustor front end more uniform. This technology, named *Multi-Point Lean Direct Injection* (MPLDI), makes possible the control of the injector staging mitigating hot streaks and instabilities. Nevertheless, MPLDI technology is at the first stages of development and only prototypes are present (Tacina et al. [23]; Heath et al. [24]).

The last type of injector among the three innovative configurations proposed is the PERM technology which will be extensively tested in the second part of the present work.

The PERM injector (Fig. 1.9) is developed for Ultra Low NOx (ULN) com-

[3]European Workshop on New Aero Engine Concepts http://www.newac.eu/

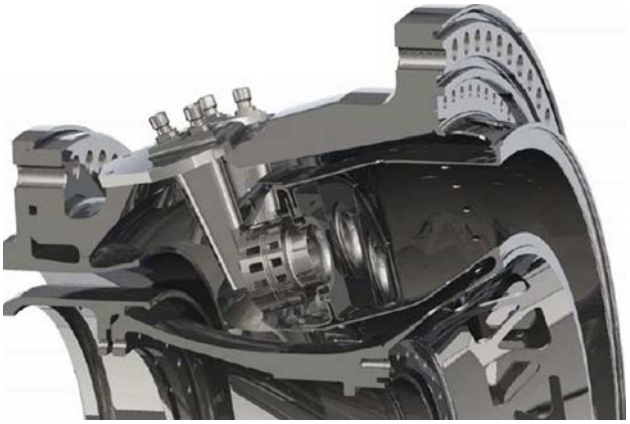

Figure 1.10: AVIO combustor with PERM technology[4]

bustor core technology for regional turbofan application and it is addressed to achieve partial evaporation inside the inner duct and a rapid mixing within the combustor, optimising the flame position and the stability of the combustion process. It is characterized by two radial co-rotating primary and secondary swirlers used to assign angular momentum on the two distinct inlet air flow; before entering in the combustion region, the swirled flows are accelerated in the inner and the outer nozzles thanks to a conical internal body (Kern et al. [25]).

Regarding the fuel supply system, the primary fuel is provided by a pressure atomizer located in the center of the injector which is used to create a fuel spray within the injector nozzle. A secondary fuel, issued by internal channels, creates a liquid film onto the nozzle lip. The film is dragged by the swirled air flow and then it is broken up near the lip, generating droplets that participate to the combustion process after evaporation.
This type of injector is distinguished by an extremely high amount of air directly supplied to the nozzle, a sketch of the AVIO combustor with PERM technology is reported in Fig. 1.10.

Nowadays, one of the main concern regarding the development of the PERM technology is their applicability in core-engine for regional turbofan with high OPRs (up to 50) according to the development trend of turbofan;

[4]European Workshop on New Aero Engine Concepts http://www.newac.eu/

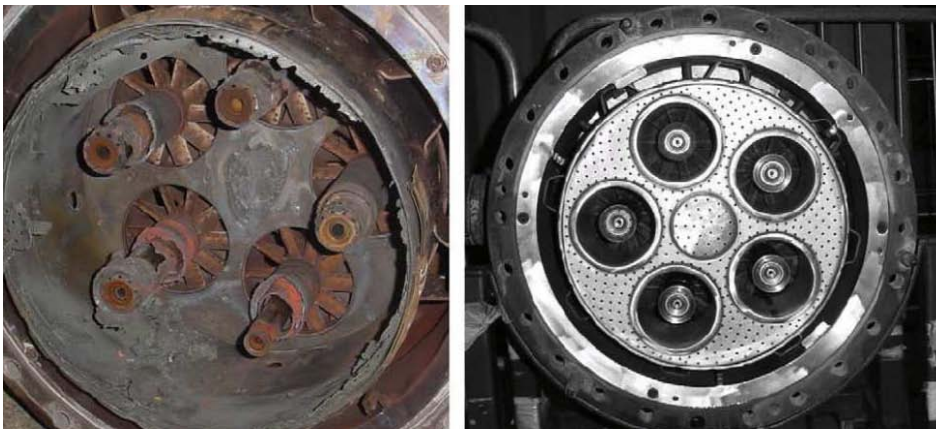

Figure 1.11: Effect of combustion instabilities on burner assembly [9]

moreover the research on this type of swirler is aimed at improve the stability at low regime (IDLE operation), where the flame is quite susceptible to extinction through lean blow-out, and at optimize the staging within the nozzle (Marinov et al. [26]).

1.3.1 Combustion Instabilities and Mitigation Techniques

One of the most common problem emerged in the development of lean combustor is the established of combustion instabilities. Combustion instabilities, generally know as thermoacoustic instabilities, are large amplitude oscillations of pressure and velocity inside the combustor chamber. They are caused by unsteady heat release with the flame that acts as an instability source.

As described in the previous section, the thermoacoustic instabilities are a relevant problem that compromise the safety and integrity of combustor chamber. Pressure oscillations are cause of wearing and fretting due to low and high cycle fatigue (Fig. 1.11).

The heat release instabilities, considered as the source of energy able to sustain the phenomena, are generated by several mechanism, among these the main are: vortex shedding, oscillation of AFR due to the presence of fuel

pocket not perfectly mixed with air, unsteadiness of air and fuel at injector inlet and oscillation of the flame surface (Lieuwen et al. [27]; Schuller et al. [28]). The instabilities are characterized by a mechanism in which the fluctuations of heat release are coupled with the acoustic field. The phenomena can be described as an internal feedback loop in which the unsteady heat release produces pressure fluctuations and vice-versa. An extensive review on combustion instabilities is recently presented by Huang and Yang [9]: starting from the recent development used to reduce the emissions in the industrial gas turbine they analyse the mechanisms driving the instabilities and the recent progresses in both analytical modelling and numerical simulation of swirl-stabilized combustion.

The control and mitigation of the thermoacoustic phenomena are generally carried out by two different methods based on active or passive control technique. Both methods aim at interrupt the coupling between unsteady heat release and acoustic waves.

The active control methods involve a control of the system using energy from an external source and acting on several input parameters. Generally, the purpose is to minimize the differences between the instantaneous desired and actual behaviour of a dynamic system. Active control is an attractive strategy because it relies on a broadband modulation of pressure oscillations in combustor chambers by means of sensors and actuators. Example of different active systems are extensively reported in the scientific literature, most of the proposed work are based on a phase-delay control in which heat release or pressure measurement are properly delayed (McManus et al. [29]; Richards et al. [30]; Padmanabhan et al. [31]). The main concern of active systems is that the dynamic behaviour of the system is generally unknown and the controller needs to be carefully tuned in all the operating conditions.

Passive strategies to control the instabilities involve changes or installations of dedicated hardware either to reduce the rate at which the energy is transferred to the pulsating flow or to increase the losses of acoustic energy by dissipative processes. These systems are cheaper and easier in design and

manufacturing with respect to the active methodology. On the other hand they are typically incisive only in a narrow band of frequency.

Among the passive devices, the two most used especially for land applications are the Helmholtz resonators and the quarter wave tubes (Dupère and Dowling [32]; Corà et al. [33]; Klaus et al. [34]; Sohn and Park [35]). Both devices act as acoustic energy dampers with closed resonators, the acoustic energy is dissipated at the entrance of the device by the pulsating flow that enter and exit the resonator mouth when pressure oscillations occur. In addition, if the resonator is correctly designed, it may change the acoustic impedance of the combustor liner and subsequently certain discrete oscillations are cushioned. Despite the passive resonators have been successfully installed on premixed combustors for land applications, their use on aero-engine is difficult because they are heavy and do not guarantee compactness. Combustor designer are searching for effective passive acoustic dampers that take the minimal amount of space without increase the engine weight. For this purpose, the holes of the liner cooling system in general act as a broadband acoustic attenuator able to mitigate thermoacoustic instabilities. Multi-perforated liners are hence very attractive in aero-engine field due to the opportunity to have an efficient cooling system and a device able to mitigate the detrimental pressure fluctuations. Further details on this acoustics damping strategy will be examined in depth in the next Chapter.

Chapter 2

Problem Overview

Contents

In one of his famous work, Sir Frank Whittle commented that one of the main concern regarding the early development of the engines based on the Joule thermodynamic cycle was the development of reliable combustor chamber able to work at an intensity at least 20 times greater than had been achieved before in any machine (Whittle [36]). Combustors in modern engines operate with even higher intensities, on the order of $1GW/m^3$, yet it is not unusual for aircraft applications to remain in service up to 20000 flights without undergo significant maintenance [37]. The high combustion intensities pose a relevant challenge to development of combustor technologies and in particular in to design effective cooling systems to manage the working temperatures of the walls, such as of combustor liners, that limit the combustion zone. For this reason, manufacturers are searching for novel and reliable cooling systems able to follow the limits imposed by the development

trend of core-engines, described in Chapter 1.

2.1 Flow Field of Lean Combustors

The comprehension of flow filed behaviour inside a combustor chamber plays a significant role in the definition of a well-performing cooling scheme for liners in order to improve durability of components. As stated in Chapter 1, modern combustors employ swirl injectors to provide the dominant flame stabilization mechanism; these system are characterized by highly swirling and expanding flows. These flow structures make hard the estimate of the heat load on the gas side of the liner and its impact on the liner cooling systems that generally consider injection of cooling flow to provide an insulated cold layer between gasses and metal wall. For example the estimation of heat transfer coefficient distribution cannot be estimated with sufficient accuracy using classical simplified correlations, which may lead to high overestimation of the cooling rates and, above all, makes difficult the optimization of the cooling arrangement.

Several works focused on the characterization of the flow structures generated by swirling flows coming out from combustor injectors: a first extensive review dealing with swirling flow in combustion was given by Lilley [38]. Among the outcomes of this work, the degree of swirl of an injector is identified through the swirl number (S_N): if $S_N > 0.6$ strong radial and axial pressure gradients are set up near the nozzle exit, resulting in a central toroidal recirculation zone (RCZ) and other typical flow structures, like the vortex breakdown [39] and the precessing vortex core (PVC). Both numerical and experimental works were aimed at the characterization of these flow structures: Syred et al. [40] used a two component laser anemometry system to measure the flow field due to the interaction of PVC and the reverse flow zone in the exhaust of a swirl burner. Vu and Gouldin [41] reported hot wire measurements in an axisymmetric combustor: in the RCZ, tangential velocities were found to be very small while levels of turbulence and dissipation rate were very high. Rhode et al. [42] performed mean flow-field studies in axisymmetric combustor geometries with swirl. Various flow-field

configurations with different side wall angles and swirl vane angles were investigated to characterize the time-mean streamlines, recirculation zone, and regions of high turbulence. The length and the width of the recirculation zone was found to increase with swirl vane angle until a critical angle was reached, after which any further increase in swirl shortened the length but further increased the width. The major effect of side wall expansion angle was to shorten the corner recirculation region, with no major effects on the central recirculation. Ferrell et al. [43] reported experiments with five-hole pitot probe velocity measurements and flow visualization.
More recently, Spencer et al. [44, 45] performed PIV, LDA and hot wire measurements supported with LES calculations in an annular full scale three-sector isothermal model of a gas turbine combustor: they gave details to a better understanding of the processes occurring in the combustor such as the annular jet impingement and the interaction of the swirled flow with the primary jets. Gnirb and Tropea [46] performed PIV and concentration measurements using POD analysis on a gas-turbine model composed by 5 swirlers in planar arrangement. In addition to the mean flow field inside the model, measurements highlight the concentration of mass flow injected through a dilution hole.

More of the works reported above deal with flow field analysis of injector developed for traditional diffusive combustor, however in the last years with the growing interest on development and optimization of lean injector several authors have carried out flow field measurements on the novel LDI and PERM injectors. Due to the fact that most of the air (up to 70%) passes through the injection system, the flow field is characterized by high intensive recirculation zones and strong interactions with the liner surface.

Kern et al. [25] and Marinov et al. [26] studied the flow field and the flame characteristic produced by a PERM injector in a cylindrical combustion chamber by means of numerical simulations and LDA measurements: they characterised the shape and the intensity of the RCZ generated by the injector and found that only LES approach is able to predict high frequency dominant coherent structure such as PVC. In addition they highlight the

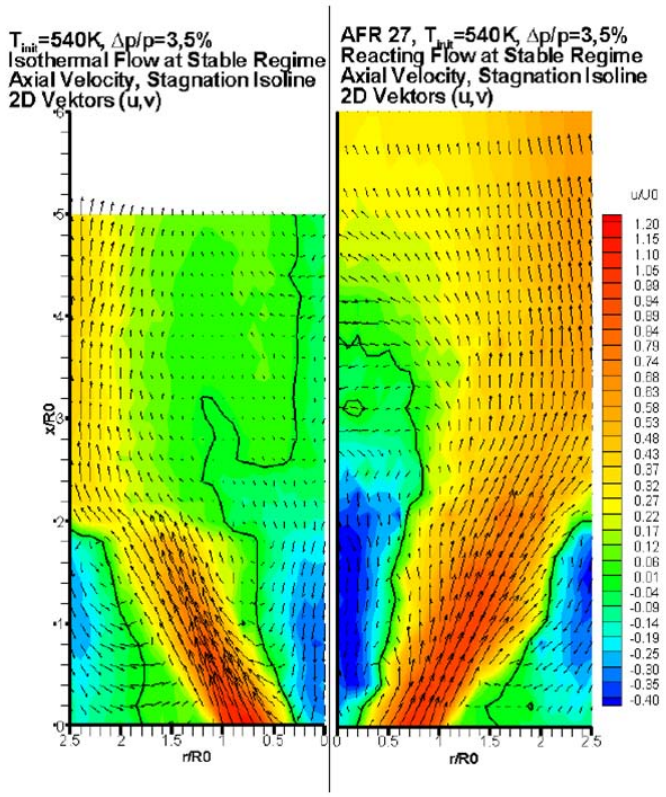

Figure 2.1: Flow field measurement of a PERM injector in isothermal (left) and reacting/stable condition (right) [26]

difference between reactive and non reactive flow field: the reactive case reduces the axial length of the Inner Recirculation Zone (IRZ), and the near wall flow field seems to be subjected to more intensive acceleration and velocity magnitude (Fig. 2.1).

Wurm et al. [47] carried out the investigation of swirled combustion chamber flows in a three sector scaled test facility equipped with LDI injector at isothermal condition (Fig. 2.2). PIV measurements downstream of the central burner highlighted the identification of characteristic near wall effects and provided proper information for the design of effective cooling system.

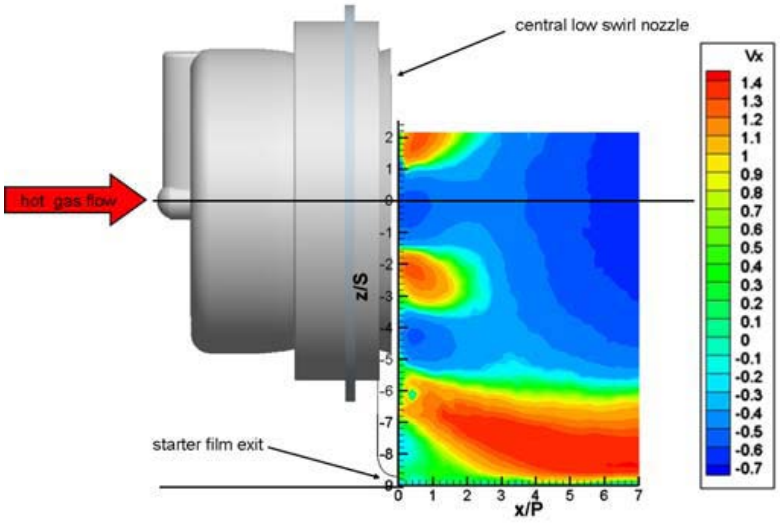

Figure 2.2: Flow field measurement of a LDI injector in isothermal condition [47]

2.1.1 Convective Heat Transfer

The swirled flow in a combustion chamber deeply influence the heat transfer coefficient (HTC) distribution on the liner surface, its knowledge is essential to correctly predict the linear heat load.
Most of the studies available in technical literature deal with apparatus equipped with backward facing step to reproduce a recirculation zone and measuring its influence on wall heat transfer. Shisnova et al. [48] and Vogel and Eaton [49] studied the convective transfer in the recirculation zone. They showed, in the case of a turbulent flow, that the thickness of the boundary layer upstream of the separation plays a very significant role in the maximum of the heat transfer value: the maximum Nusselt number increases with the thickness of the boundary layer. Pozarlik et al. [50] studied the heat transfer in a recirculating zone at steady state and oscillating conditions. Heat transfer coefficient was founded minimum in the recirculating area and maximum after around five times of step height for steady state measurements.

Despite the interest in that topic, to the author's knowledge there are only a very few data, in literature, dealing with the evaluation of convective

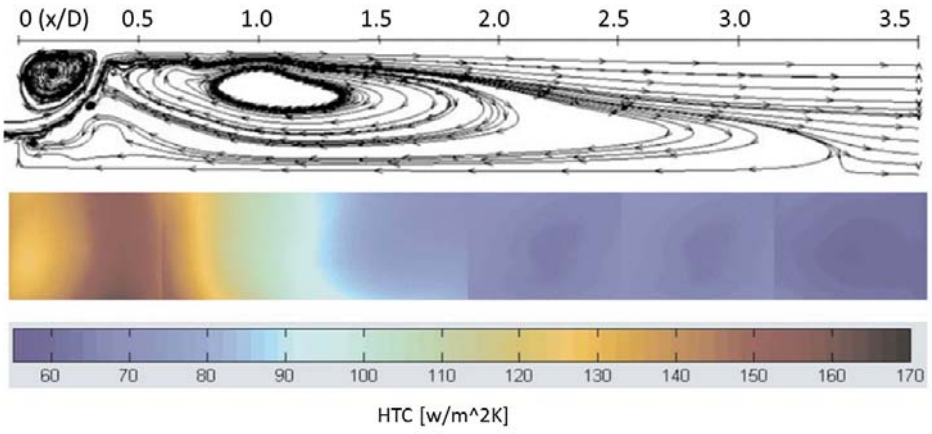

Figure 2.3: Streamline and detailed heat transfer distribution in combustor chamber [51]

heat transfer coefficient due to a swirled flow generated by a representative geometry of a combustor injector. Memar et al. [52] studied the heat transfer distributions generated by the mixing of two confined coaxial swirled jets. They found that local heat transfer rates and flow physics are strong influenced by the swirl number of inner and outer jets and the annular-to-inner jet Reynolds number ratio. The shearing of two coaxial jets generated high mixing rates and high turbulence level resulting in heat transfer coefficients that were substantially higher than those that would be obtained at the same Reynolds number in fully developed pipe flow. Peak of local Nusselt number were obtained in the region where the inner jet impinged on the test section wall. Patil et al. [51] performed experimental and numerical investigations on liner wall convective heat transfer coefficient in an annular and can combustor test rigs (Fig 2.3) they employed a swirler which generates a flow field representative of a real engine injector. The experimental analysis is carried out using air at ambient conditions and measuring the temperature of the heated liner wall by means of an IR camera. The interaction of the swirled flow with the different surface curvature (can liner, annular convex and concave liners) results in a slightly larger region of peak heat transfer on the concave liner wall. It is observed that, as the Reynolds number increases, the Nusselt number augmentation reduces on the walls. Additionally, it is

also observed that the flow structures in the combustor are mostly independent of the Reynolds number.

2.2 Combustor Liner Cooling Systems and Effusion technology

Driven by the trend of increasing the overall pressure ratio in the novel core engines, the compressor exit temperature is forecast to drastically growth. Besides the introduction of lean combustor to respect the future emission targets, a larger amount of air is then injected together with fuel, reducing the availability of coolant for the combustor dome and above all liner cooling [53]. In addition, the reduction of dome coolant lead also to a strong reduction of the cooling flow generally injected upstream the linear wall to provide a slot cooling (Lefebvre [6]). This scenario makes fundamental the design of an high efficiency liner cooling system, with low air consumption.

Classical cooling systems for combustor liner are based on generation of wall film cooling in order to create an insulate cold layer between hot combustion gasses and liner wall using the air flow rate that does not participate directly to combustion process. There are several possibilities to generate film cooling. The best performing solution to generate high effectiveness film cooling is to realize a number of 2D slots in the liner wall. In the earlier designs, slots were realized by overlapping metal sheets separated by a corrugated strip; several slots are generally created along the axial depth of the liner.

More recently development of slot cooling for combustor chamber are based of combined effect of slot protection and several strategies, such as impingement, to intensify the convective heat transfer on the cold side. Indeed the slots are effective system to generate film cooling, they are not be able to exploit the heat sink potential of the coolant. The combined cooling methods usually have a double wall to keep more lower the metal temperature such as the concept with float wall to compensate the thermal expansion (Fig. 2.4).

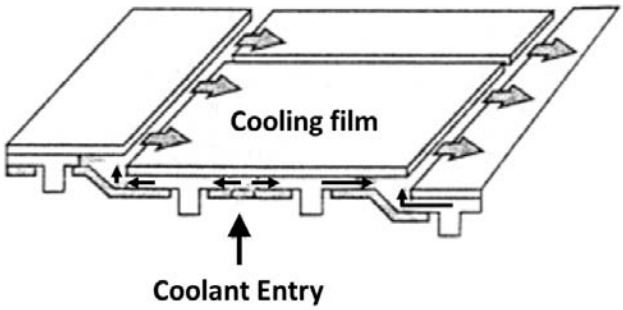

Figure 2.4: Double wall design of a slot systems [53]

Despite the performance of methods proposed above have the ability to create an effective thin cold layer at liner wall, it requires a large amount of coolant not compatible with the lean combustor architecture. For this purpose, combustor designers in aircraft field have searching for alternative solutions for liner cooling system respecting the following requirements:

- High effective cooling systems with low air consumption for application at high OPR in lean combustors.

- Avoid pronounced temperature gradients that could result in high thermal stresses.

- Lightweight, reliable and cost-effective solutions.

- Avoid reaction quenching due to the injection of cool air, and moreover prevent the injection of uncontrolled air that could participate to combustion process deteriorating the action of the low-NOx technologies.

- Act as passive device to mitigate thermoacoustic instabilities.

One of the most promises cooling technology able to ensure the requirements listed above is the *effusion cooling*. This reliable cooling technique is suitable for novel lean combustor for aero engine because it allows to increase thermal effectiveness with low coolant consumption compared to other technologies.

Effusion cooling consists of an array of closely spaced discrete film cool-

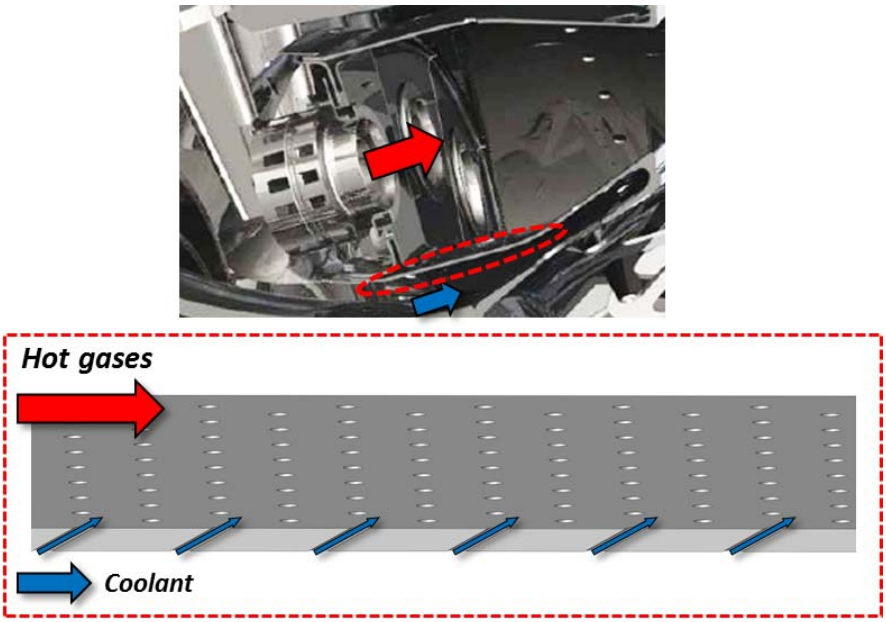

Figure 2.5: Effusion cooling scheme

ing holes distributed on the whole liner surface (Fig. 2.5). The resulting large number of holes with a reduced diameter with respect to traditional film cooling situations, are generally manufactured by means of laser drilling technique (Moskal [54]). When the perforation has a length to hole diameter ratio below one, the technology is generally referred to as *full coverage film cooling*.

The cooling air from the annulus side of the combustor chamber is injected to the gas side boundary layer to constitute a protective cold layer of cooling between the liner surface and combustion gasses flowing over it. An exhaustive review of effusion cooling, not only for combustor application, is recently reported by Krewinkel [55]. A picture of a prototype of the combustion chamber equipped with effusion scheme developed within the European Integrated Project NEWAC is shown in Fig. 2.6.

Even if effusion cooling does not generate an excellent insulating layer like slots manufactured on liner wall, the good cooling performances are guaranteed by the heat removed by forced convection trough the holes by the passage of coolant (Gustafsson and Johansson [56]). In fact, the effusion

Figure 2.6: Combustor prototype of European Project NEWAC [57]

cooling acts as an approximation of transpiration cooling: the large number of micro-holes distributed on the surface allow an excellent improvement in lowering the liner temperature, trough internal heat removal, despite a slight reduction of the wall protection, with respect to traditional film cooling arrangement, is expected at least in the first part of the liner.

In addition to its thermal effectiveness, nowadays effusion technique is taking the attention of manufacturers as potential acoustic damping device since the use of perforated plate find applications to control noise emission since late '70 (Dean [58]). The damping capabilities of perforated plate is generated by the unsteady flow across the plate, sustained by the acoustic filed, that leads to the generation and diffusion of vorticity near the hole lip. With this mechanism the acoustic energy is transferred to the flow field field as kinetic energy and then dissipated trough the action of shear stresses (Bellucci et al. [59]; Rupp et al. [60]).

In the last years several works deal with the measurements or prediction of the acoustic behaviour of perforated liner. Eldredge and Dowling [61] proposed a 1D model to predict the acoustic behaviour of a perforated plate. More recently Heuwinkel et al. [62] performed an experimental campaign in cold condition aimed at evaluate the acoustic energy dissipation of cylindrical liners with several perforation pattern with normal holes. The tested

geometries showed good damping capabilities on wide frequency range.
Seven different cylindrical liners with effusion perforation were characterized from an acoustic point of view by Andreini et al. [63], the same test matrix in terms of perforation pattern will be considered in the first part of present work (Cfr. 4.3). Effusion systems have shown broadband capabilities in term of acoustic energy absorption. They found in perforation porosity the main geometrical parameter driving the damping capabilities; in addition an increase of acoustic performance was recorded reducing the velocity of the coolant inside the holes (i.e. coolant Mach number).

The latter scientific works confirm the capabilities of multi-perforated plate to damp acoustic flow field motivating the development and the optimization of cooling system based on effusion technique from a thermal standpoint taking into account its acoustic behaviour.

2.2.1 Main Parameters Definition for Effusion Systems

The effusion cooling behaviour is affected by several fluid dynamics and geometrical parameters. The heat transfer to a cooled surface can be computed using Eq. 2.1 [64]:

$$\dot{q} = HTC_{main} \left(T_{ad} - T_w\right) \tag{2.1}$$

where the subscript *main* is used to identify the hot gas side. The driving parameter that controls the heat transfer is the temperature difference between the wall temperature T_w and the adiabatic wall temperature T_{ad}. This last parameter, according to Lakshminarayana [65], is defined as the temperature obtained locally on the surface in the case of perfectly insulated surface (i.e. adiabatic wall). The definition of heat load based on the adiabatic wall temperature leads to a definition of an heat transfer coefficient HTC independent to the temperature difference but dependently only to the flow field.
The adiabatic wall temperature without coolant injection corresponds to the recovery temperature of the mainstream, that it is close to total mainstream

temperature especially in turbulent flow at moderate Mach number; while in presence of coolant it is presented in a dimensionless form as adiabatic effectiveness η_{ad}, Eq. 2.2:

$$\eta_{ad} = \frac{T_{main} - T_{ad}}{T_{main} - T_c} \tag{2.2}$$

Adiabatic effectiveness assumes value equal to one when, in the limit case of adiabatic test case, the wall assumes a temperature equal to T_c: in this case we obtain the maximum protection and the driving temperature difference is reduced as far as possible (i.e. lower heat load and hence lower wall temperature in case of the same heat transfer coefficient). In fact, in absence of radiative phenomena, the temperature of a cooled surface is always below the adiabatic wall temperature.

The second parameter that constitutes the definition of heat load is the heat transfer coefficient, to limit the heat load to a cooled surface is generally required to reduce the HTC_{main}. Anyway, it is worth to notice that in presence of a relevant radiative heat load it can happen that metal temperature goes up the local adiabatic film temperature. In this latter case, that could happen especially in diffusive combustor chamber, a greater gas side heat transfer should have a beneficial effect on wall cooling, limiting the impact of radiation.

Since the effusion systems act on both the right terms of Eq. 2.1, a very useful parameter to analyse the performance of cooling systems is the Net Heat Flux Reduction ($NFHR$) [66]. It quantifies the the reduction of heat load on the gas surface, with respect to the baseline situation (i.e. non-blowing case, subscript "0"), Eq. 2.3:

$$NHFR = 1 - \frac{\dot{q}}{\dot{q}_0} = 1 - \frac{HTC_{main}}{HTC_{main;\,0}} \left(1 - \eta_{ad} \cdot \theta\right) \tag{2.3}$$

where θ is the dimensionless temperature defined as, Eq. 2.4:

$$\theta = \frac{T_{main} - T_c}{T_{main} - T_w} \tag{2.4}$$

it represents a parameter that depends only on cooling situation and to the desired and allowable wall temperature. One of the goal of the effusion systems is to increase the $NHFR$ as much as possible. It worth to notice that, in presence of high radiation the $NFHR$ parameter is not representative of the reduction of heat load to the external liner surface. In addition, it can not be used as performing parameter comparing different effusion arrangement because it does not take into account the heat sink effect. Nevertheless, with this limitations, it represents a powerful parameter to summarize the impact of effusion cooling systems on HTC and η_{ad}.

As already been inferred both geometrical and fluid dynamic parameters affect effusion cooling systems behaviour. Hole injection angle, spacing, length to diameter ratio, perforation porosity are among the geometrical features playing a major role in cooling performance. Regarding the flow parameters, a set of dimensionless parameters that govern the interaction of gas and coolant can be identified, such as blowing ratio BR, velocity ratio VR, density ratio DR and momentum ratio MR, Eq. 2.5:

$$\begin{aligned} BR &= \frac{(\rho U)_c}{(\rho U)_{main}} & VR &= \frac{U_c}{U_{main}} \\ DR &= \frac{\rho_c}{\rho_{main}} & MR &= \frac{(\rho U^2)_c}{(\rho U^2)_{main}} \end{aligned} \tag{2.5}$$

Usually, VR is employed to distinguish the occurrence of penetration regime. According to the classification proposed by Lefebvre [6], coolant jets from a cylindrical hole start to lift off from the surface for $VR > 0.8$. As highlighted before, both film protection and heat sink effect have a significant impact on lowering the liner temperature. A parameter able to evaluate this combined effect is the overall effectiveness, defined in Eq. 2.6:

$$\eta_{ov} = \frac{T_{main} - T_w}{T_{main} - T_c} \tag{2.6}$$

where T_c is the coolant temperature approaching the cooling system. Overall effectiveness, taking into account implicitly in its definition the heat sink

effect and hence the conduction across the liner wall, is affected by the value of Biot number, Eq. 2.7:

$$Bi = \frac{HTC \cdot d}{k} \tag{2.7}$$

2.2.2 Heat Transfer Augmentation

The injection of coolant air and consequently the mixing with the hot gases in the near wall flow field is governed by very complex and unsteady structures. For this reason the heat transfer coefficient is expected to change compared to the case without coolant injection. The knowledge of the heat transfer distribution under coolant injection conditions is hence essential to correctly predict the heat load to the combustion liner in presence of active effusion system. It is worth to notice that, in film cooling situations with very few rows of holes, the heat transfer augmentation is generally limited to a portion of the liner near the holes. On the contrary, in effusion systems with a distributed injection on the whole liner surface, the heat transfer augmentation involves all the protected surfaces.

Several studies were carried out in the past with planar liner geometries under uniform mainstream conditions. Metzger et al. [67] were among the first researchers to comprehensively deal with heat transfer coefficient variations for both inline and staggered arrays, finding a significant increase compared to values obtained with no injection; Kelly and Bogard [68] evaluated the heat transfer coefficient augmentation associated with a full-coverage array. A wide experimental survey with effusion cooled plates with normal injection were carried out by Kelly and Bogard [68]. They compared the results obtained with coolant injection with the results obtained with the non-film cooling ones. Increasing the blowing ratio, they found an increase in the heat transfer coefficient up to about 65% at $BR = 0.77$.
Heat transfer augmentation measurements at two different density ratio were recently performed by Andreini et al. [57] on an effusion array with an upstream slot injection. They found a linear dependency between heat transfer augmentation and the imposed velocity ratio; augmentation factor up to 4 are evaluated for effusion velocity ratio of 7 (Fig. 2.7).

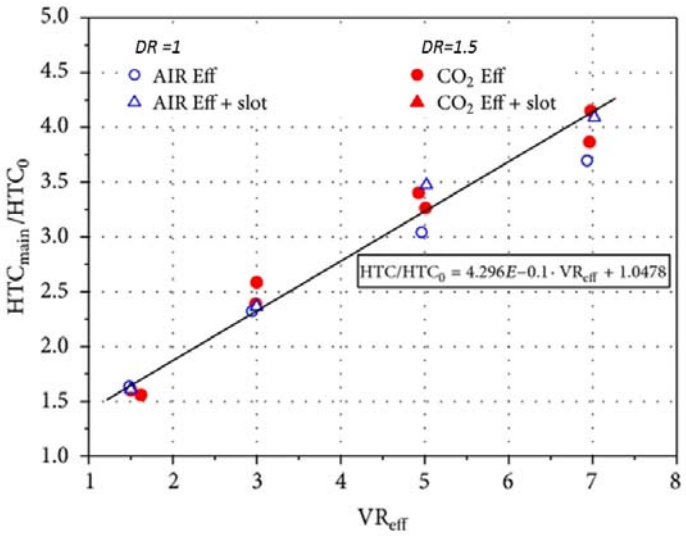

Figure 2.7: Heat transfer augmentation for film cooling arrangements with and without slot injection [57]

The results obtained in the works reported above indicate a generally increase of heat transfer due to coolant injection. However the studies were carried out with a uniform flow field on the gas side, this means that the experimental results could be used with sufficient accuracy for the design of liner close to the combustor exit where the expected flow field is not affected by recirculation and strong accelerations near the wall. To the authors knowledge, measurements of bidimensional distributions of heat transfer augmentation factor for effusion systems under realistic swirl flow conditions are not yet reported in the available literature.

2.3 Combustor Effusion Cooling

Attention will be now addressed to relevant past studies concerning combustor liner effusion cooling. The main part of full coverage film cooling studies have been focused on the effectiveness of the protection due to the injection of coolant. Studies on effusion cooling, or on multi-row holes injec-

tion, have been performed since the late 70's.

Sasaki et al. [69] presented film cooling adiabatic effectiveness results while Mayle and Camarata [70] proposed a correlation for that parameter. Andrews et al. [71, 72] investigated the effects of various factors on full-coverage film-cooling: they showed the strong influence of the number of holes, of their length and injection angle. Harrington et al. [73] focused on a configuration with very short effusion holes with normal injection angle, finding that an asymptotic fully developed adiabatic effectiveness level was established within four or eight rows.

Scrittore et al. [74] studied the effects of dilution hole injection on effusion behaviour; they found relevant turbulence levels downstream dilution holes, thus leading to an increased spreading of coolant jets. Scrittore et al. [75] measured velocity profiles and adiabatic effectiveness of a full coverage scheme with blowing ratios from 3.2 to 5.0, finding the attainment of a fully developed effectiveness region at the 15^{th} row and a very low effect of blowing ratio on cooling performance.

A correlative analysis of effusion cooling systems, by means of a DOE (Design Of Experiment) approach, was performed by Arcangeli et al. [76]; one of their main objectives was the investigation of the effects of the main design parameters. A big influence on global performance has been shown by the hole length to diameter ratio, as it was found that the overall effectiveness always increases with l/d.

More recently Ligrani et al. [77] presented film effectiveness and heat transfer results for full coverage film cooling arrangements with streamwise pressure gradient; they studied the effect of the blowing ratio and the influence of dense and sparse hole arrays on the thermal effectiveness.

Experiments under conditions of very high freestream turbulence up to 25% were conducted by Martin and Thorpe [78] on an effusion test plate with angled hole array and staggered pattern, varying blowing ratios from 0.3 to 1.5. They found that when freestream turbulence is increased the spatially averaged effectiveness can increase by as much as 85% at $BR = 1.4$ due to the spanwise spreading of coolant and turbulent transport of coolant back towards the plate surface (Fig. 2.8).

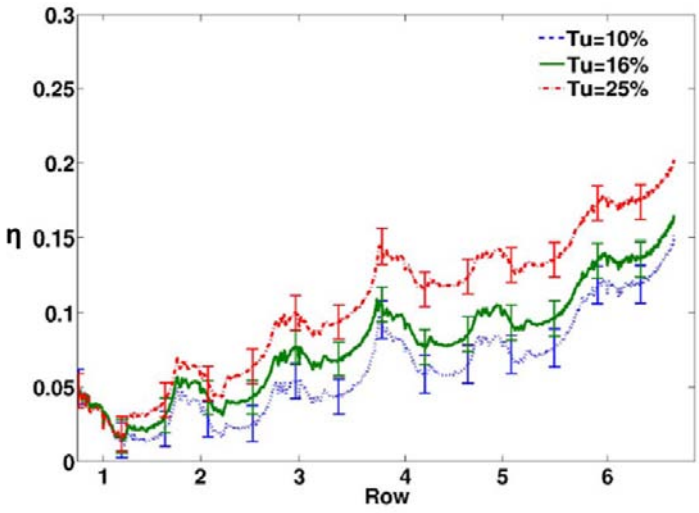

Figure 2.8: Spanwise averaged adiabatic effectiveness for DR=1.4 at different turbulence level of mainstream (Martin and Thorpe [78])

A real combustion cooling scheme was experimentally studied by Ceccherini et al. [79] measuring the overall effectiveness and heat transfer coefficient in order to evaluate the combined effect of slot, effusion and a large dilution hole at variable blowing ratios; they found that an increase in BR leads to lower values of effectiveness.

Despite many experimental studies deal with investigating the effusion cooling performance, most of them were conducted precluding the possibility to point out the effects of density ratio between the two flows. Density ratio is, however, a key parameter for the design of a combustor liner cooling system, mainly because of the actual large temperature difference between coolant and burned gases inside the core. Lin et al. [80] investigated both experimentally and numerically adiabatic film cooling effectiveness of four different inclined multihole film cooling configurations; the survey, which was specific for combustor liner applications, was performed using a mixture of air and CO_2 as coolant, but it was mainly focused on studying the influence of hole geometrical parameters and BR on film cooling rather than on the effects of DR. Andreini et al. [57] studied through an extensive experimental campaign the effect of density ratio on the cooling performance of

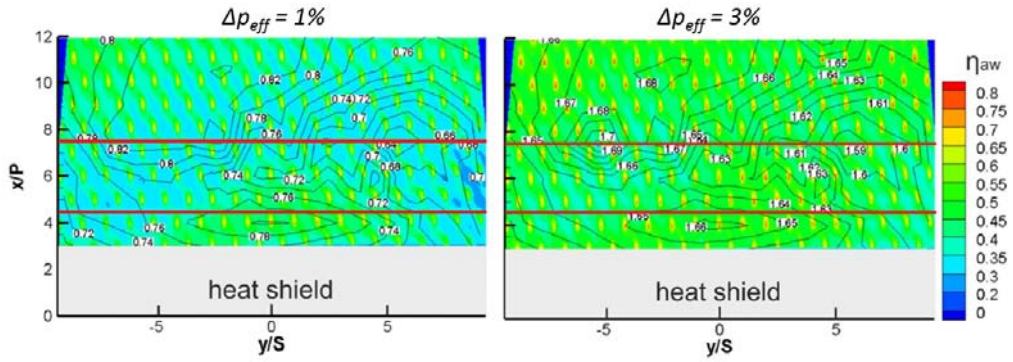

Figure 2.9: Adiabatic effectiveness distribution using IR thermography at representative gas flow field (Wurm et al. [82])

a real engine cooling scheme composed by a slot cooling, an effusion array and a large dilution hole. They found that in penetration regime the effect of density ratio on the adiabatic effectiveness can be neglected.

Most of the scientific works on effusion cooling systems deal the measurements of thermal behaviour with simplified flow condition on the gas side. Typical experimental configurations are based on flat plate with uniform flow field on the gas side. Despite the interest of the author on this topic very few work are related to the effusion cooling behaviour under realistic swirl conditions. A backward facing step was employed by Maiuolo et al. [81] to simulate the effect of typical corner recirculation zone on an effusion cooling system measuring heat transfer and adiabatic effectiveness. Despite the step is able to reproduce a RCZ in the first part of the liner, the flow field can not be considered fully representative of a lean aero-engine combustor (Cfr. 2.1). Recently, a pioneering work was carried out by Wurm et al. [82, 83]: developing a cold and planar sector test rig equipped with three LDI injectors, they have measured the cooling effectiveness of an effusion array with starter film cooling by means of IR thermography. The survey gave a deep insight the interaction between swirling flow and cooling flow, the results indicated that better adiabatic effectiveness can be achieved increasing the pressure drop across the multi-perforated plate from 1% to 3% (Fig. 2.9).

2.4 Thesis Outline and Motivations

The requirement for improvement the aero-engine combustors following the development trend of novel core engines has addressed research effort to deepen the knowledge on effusion cooling systems. In this context, design of multi-perforated plates for an optimum thermal and acoustic behaviour, to damp thermoacoustic phenomena (Cfr. 1.3.1), represents an attractive goal. Beyond that, the design and optimization of effusion cooling system have to cope with flow field characterized by highly swirling and expanding flows generated by the lean injectors. This complex flow field and its interaction with cooling systems are difficult to be predicted; as a consequence, the convective heat transfer and adiabatic effectiveness distributions on the liner surface cannot be estimated with sufficient accuracy using classical simplified correlations, which may lead to high overestimation of the cooling rates and, above all, makes difficult the optimization of the cooling arrangement. To the knowledge of author, there are only few data, in literature, dealing with these topics.

For the reasons reported above, the present work aims at deepening the knowledge of effusion systems from a thermal point of view by means of two different experimental campaigns, even in case of representative/swirled mainstream flow field.

Previous literature surveys report that several parameters affects the effusion thermal efficiency, among them the most important are: hole pattern, hole inclination angle, hole diameter and blowing and velocity ratio. These parameters represent the starting point for the definition of a test matrix composed by 7 multi-perforated planar test plates, which represent portions of liner geometries, tested in the first part of the work. Imposing several working conditions among the actual engine values, the geometries are tested in terms of adiabatic effectiveness distributions and local values of overall effectiveness. The goal of the first survey is to illustrate the effect of the main geometrical and fluid dynamic parameters on cooling performance and, above all, to search a design optimization strategy taking into account the acoustic

standpoint in accordance with the conclusion of the experimental work of Andreini et al. [63], directly linked to the present research.

Results obtained in the first part of the work represents a wide experimental database of outstanding importance for the design of an high efficiency cooling system, even though the survey is carried out with an uniform flow field on the gas side leaving the impact of the swirled gas flow field an open issue. To examine in depth this topic, in the second part of the present work a dedicated experimental investigation is presented. The experimental setup consists of a scaled three sectors planar rig equipped with PERM injectors. The rig reproduces a liner cooling arrangement composed by an effusion and a slot cooling system. The flow field on the gas side is investigated by means of PIV (*Particle Image Velocimetry*) technique, imposing several realistic combustor operating conditions, especially in terms of pressure drop across cooling system and swirlers. The survey will highlight the flow filed characteristics of PERM injectors and the interactions near the wall with the cooling flow. Moreover, the cooling system will be fully characterized from a thermal point of view with direct measurements of heat transfer and adiabatic effectiveness distributions, providing useful data for the design and optimization of cooling system.

Chapter 3

Experimental Techniques and Data Reduction

Contents

3.1 Flow Field Measurements Using PIV

In the second part of the work (Cfr. 6) an extensive analysis of the PERM flow filed and its impact near the wall with the cooling system is performed by means of 2D Particle Image Velocimetry Technique (PIV).

PIV technique is based on the insertion of seeding particles inside the flow able to follow the mean flow field. The particles are illuminated trough a laser sheet and their positions are caught by a CCD (Charge-Coupled Device) camera in two different instants setting the desired time delay between two laser pulses. In order to evaluate the particle movements, the images acquired by the camera are divided in different interrogation areas. Assuming an homogeneous movement of particles inside each area, a statistic approach based on 2D cross correlation method is exploited to compute a vector associated to the particle movement. Moreover, the velocity vector on the laser plane is directly computed by the movement vector knowing the time delay between the pair of images and the "*scale factor*" to convert CCD coordinates into space coordinates.

A generic setup for PIV measurements is reported in Fig. 3.1 where it

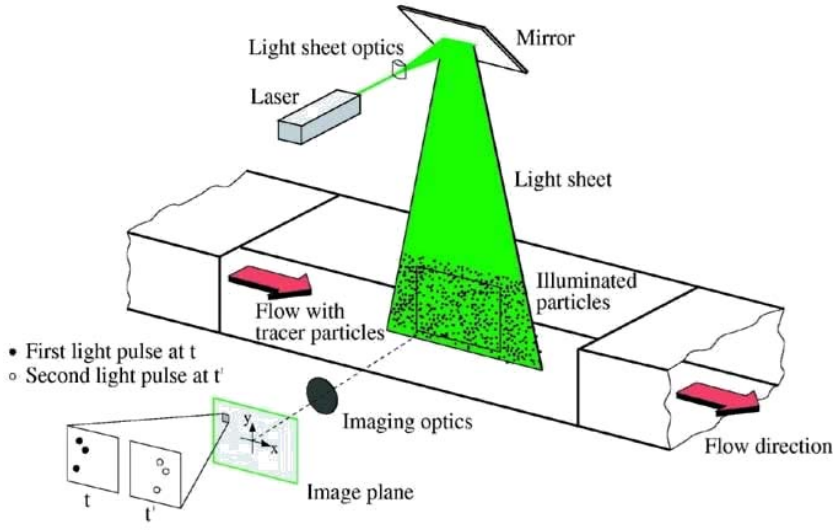

Figure 3.1: Experimental setup for PIV measurements

is possible to observe the main components necessary to perform the tests. The laser system is used to illuminate the seeding particle without chromatic aberrations, it is able to generate monochromatic light with high density of energy; a set of optic lens are used to generate the light sheet while a mirror can be used to deviate the laser beam.
The seeding necessary for the PIV measurements was introduced upstream the test section by means of a Laskin nozzle [84]. The seeding particles must be constituted by inert substance and must have a small diameter in order to follow the streamlines of the flow field. A dimensionless number able to describe the capability of particles to follow the mean flow field is the Stokes number, Eq. 3.1:

$$St = \frac{\tau \cdot U}{d} \tag{3.1}$$

where τ is a characteristic time of particle drag phenomena, generally it is inversely proportional to the particle Reynolds number; U is the local drag velocity and d is the particle diameter. To follow the streamlines, the particles must have a lower value of St number as much as possible. In addition to the previous desired characteristic, the particles must have good properties in terms of light reflection in order to correctly detect them during the data analysis. For test at low temperature, one of most reliable substance that can be used as seeding for PIV measurements is the mineral oil. Olive oil particles with a mean diameter of about $1\mu m$ were injected in the flow field through a pipe as long as the height of the inlet of the test model (Cfr. 6.1); the pipe was drilled with about 15 holes of $1mm$ in diameter, which allow a sufficient mixing between air and seeding before crossing the laser sheet.

PIV measurements are performed using a Dantec Dynamics PIV system. The system consists of a $120mJ$ New Wave Solo Nd:YAG pulsed laser operating with a wavelength of $532nm$ and a FlowSense 2Mpixel camera operating at a data rate of $15Hz$. A narrow band optical filter placed in front of the camera to ensure that only the reflected light from the particle are caught by the camera. All devices are controlled via the commercial soft-

ware Dantec FlowManager®, which allows the synchronization of the system and moreover the collecting and the processing of the data. A programmable timing unit (PTU) controlled by the software is used to provide the trigger signals to camera and laser system.

For all the measurement planes investigated in the present work, the investigation areas are too large to be covered with a single framing and at the same time to guarantee enough image resolution [84]: as a consequence, up to 16 different camera/laser positions are employed to cover the selected test planes, with a scale factor of ≈ 9 (number of millimetre on the measurements plane for one millimetre on the CCD). To avoid loss of information, each camera framing is overlapped with the neighbouring ones of about $5mm$ for each side; the positioning of the camera/laser system is done using a traverse system with the help of a dedicated calibration device located inside the test section which is primary used to calculated the image scale factor.

For each camera position, 480 image pairs are taken; the time delay between two laser pulses is adjusted depending on the local averaged velocity, from about $10\mu s$ up to $40\mu s$. The time delay represents a key parameter and must be selected accurately during the commissioning of the experimental technique: if it is too long the recognized velocity can only be assimilated to a mean and not instantaneous value; on the other hand if it is too short there is not significant gain in the measurements (i.e. small variation of particle position) and the flow field cannot be reconstructed.
The laser sheet thickness is set to about $1mm$, acting on the focus of the optical system, to keep the number of loss of pair due to out of plane motion as low as possible. In addition, to avoid reflection of the laser light and hence to reduce the noise into the acquired images, the components inside the test rig are painted with opaque black coating.

3.1.1 Data Reduction

The data reduction for each set of of 480 image pairs is carried out by means of the software Dantec FlowManager®using an adaptive grid iterative

method approach.

In the PIV standard cross-correlation technique, each pair of images are divided in several interrogation areas and the 2D cross correlation is applied to find the particle movement. However particles in the time delay between the laser pulses can left the interrogation area, loss of these particle images is known as the "in-plane drop-out", which reduces signal strength and, as a result, the number of successful vectors that can be obtained because the signal peak in correlation is lowered [46].
To overcome this issue an adaptive grid iterative method can be used. The fundamental principle of adaptive correlation is an iterative procedure based on the shift of the interrogation windows (i.e. the interrogation area is not locked in the space): from an initial guessed shift value, a shift is introduced from the first window (the interrogation area in the image frame from laser pulse one) to the second window (the interrogation area in the image from laser pulse two). The obtained movement vector calculated trough standard cross correlation algorithm [84] is used as a new estimate for the window shift in the second iteration. From the results of the previous iterative process a new run is made, but this time with a refinement of the size of the interrogation area.
Using Adaptive correlation helps in two ways. First, the signal strength is raised due to the capture of the in-plane drop-out. Secondly, a refinement of the interrogation area is possible because an adaptive window offset is applied, again producing a successful signal and increasing the resolution of results.

The approach adopted in this work starts from a 256x256 pixel initial windows size, which is reduced in three steps to 64x64 final size; two iterations were chosen for the initial step, while three iterations for the following steps to achieve maximum displacement accuracy.
The resulting velocity field from the adaptive correlation contains 49x36 vectors for each image pair. These raw vector maps are validated and filtered using in succession two approaches:

- *Peak-height validation*: this method validates or rejects individual vectors based on the values of the peak heights in the cross correlation

plane. The criterion is to compare the highest peak with the second highest peak, if it is ratio is greater than 1.2 the vector is not rejected (Keane and Adrian [85]).

- *Moving-average validation*: this criterion validates or rejects vectors based on a comparison between neighbouring vectors. The rejected vectors may be replaced by vectors estimated from surrounding values. Continuity of the flow field's behaviour is an implicit assumption in the moving-average validation method.

An average vector map for each camera framing is computed using only the validated vectors, and finally all the velocity maps, one for each camera position, are composed in a single vector map using an automatic procedure developed in MatLab®environment.

3.2 Adiabatic Effectiveness Measurements Using PSP

3.2.1 Pressure Sensitive Paint

Pressure sensitive paint (PSP) is an organic substance, composed by oxygen sensitive molecules embedded in the paint solution using a polymer binder permeable to oxygen. Through the exploitation of the luminescence behaviour of these molecules, PSP can be used to measure the oxygen concentration of the atmosphere surrounding the paints, which in turn can be linked to the partial pressure of air.

The oxygen sensitive molecules are excited by the absorption of a photon to higher energy levels by an incidence light of a certain frequency (UV light). From the excited state the molecule has several competing relaxation paths. The path of interest for PSP involves a forbidden transition

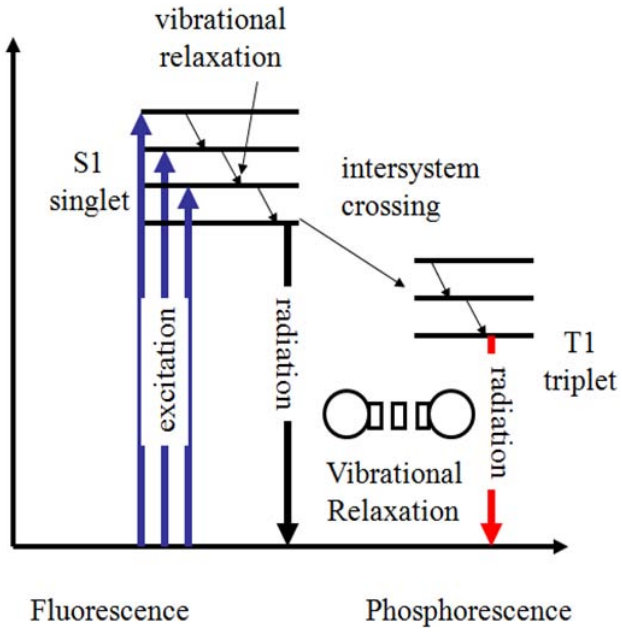

Figure 3.2: Oxygen Quenching[1]

[1]http://www.psp-tsp.com/

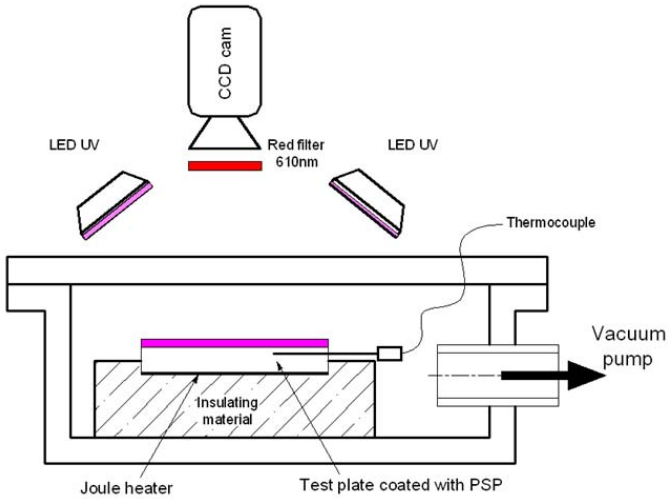

Figure 3.3: Setup for PSP calibration

to an excited triplet state from which the molecule may simply emit a photon. However, if there is oxygen present the molecule may interact with the oxygen transmitting its energy into a vibrational mode of the oxygen.

This radiationless deactivation at lower frequency results in a system where the luminescent intensity from the molecule is a function of the partial pressure of oxygen to which the molecule is exposed; the intensity of the light increases as the oxygen concentration in the binder around the sensitive molecules is decreased. This well knows phenomenon is called "oxygen quenching" (Fig. 3.2); Navarra [86] provides a detailed analysis of this process with a mathematical formulation based on the Sterm-Volmer equation.

Before their use on a test model, PSP must be accurately calibrated in a dedicated hardware reproducing the same optical conditions of the experiments. The calibration apparatus, depicted in Fig. 3.3, is constituted by a vacuum chamber, housing an aluminium test plate with Pressure Sensitive Paint, in which the pressure and the temperature of the test plate can be controlled.
PSP are sprayed with an air brush directly on the test surface with 6-8 very light cross coats resulting in a total thickness between $10 - 30\mu m$. PSP used

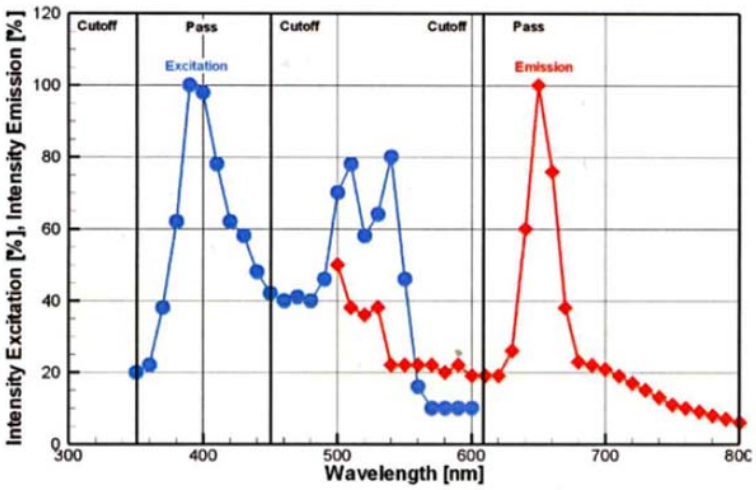

Figure 3.4: PSP with PtTFPP luminophore: typical emission spectra [87]

in the present work is supplied by Innovative Scientific Solutions, Inc. and is composed by a blend of Fluoro Isopropyl Butyl polymer (FIB) and Platinum tetra porphine (PtTFPP); as shown in Fig. 3.3, an UV 400nm Led system provides the adequate light source for paint excitation, while a 1600x1200 resolution 14-bit CCD camera (PCO.1600) with a 610nm red filter records the intensity emitted by PSP. This last filter is necessary to ensure that the exciting UV light is not captured by the scientific grade camera. A typical emission spectra of PSP paint based on PtTFPP luminophore is reported in Fig. 3.4.

Since the emitted light depends on both the partial pressure of oxygen and the surface temperature, intensity of the emitted light during calibration is recorded by the CCD camera for various pressures and for three different temperatures: pressure is controlled in the calibration chamber by vacuum pumps and the temperature of the aluminium test plate is set by means of an adhesive electric heater (Fig. 3.3).

The relation between the light emitted by the paint and the pressure is plotted in Fig. 3.5. The pressure is normalized with the room pressure (P_{ref}), while the intensity data are normalized with three different reference conditions recorded at room pressure and at the same temperature of the corre-

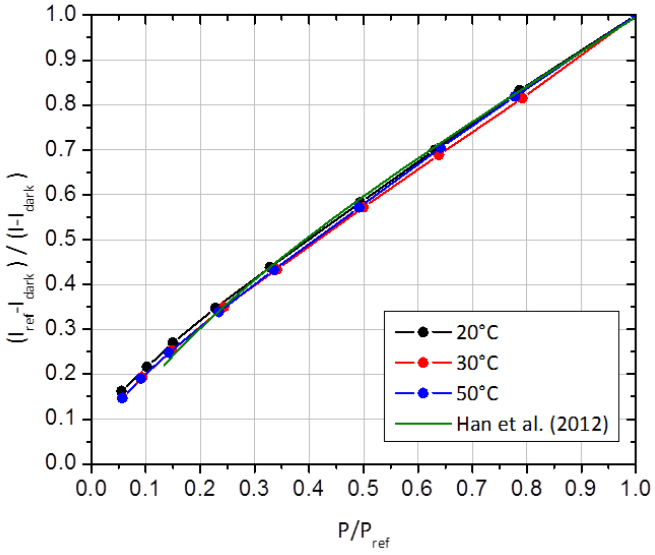

Figure 3.5: PSP Calibration Curve

spondent curve (I_{ref}). The ratio between images leads the measurement independent to the non uniform paint thickness and non uniform illumination. In order to correct background noise a non-excited image is also acquired and subtracted from all other images (*dark*). The figure shows also a good agreement with the calibration curve found by Han et al. [88] for the same PSP formulation.

The curves for three different temperatures collapse together allowing to neglect the temperature effect on oxygen quenching; a similar behaviour is found by Han and Rallabandi [89]. A polynomial curve can be computed by fitting the calibration dataset, relating the air pressure to the intensity emitted by PSP (Eq. 3.2).

$$\frac{P_{O_2}}{P_{O_2;ref}} = -0.066 + 0.716 \cdot \frac{I_{ref} - I_{dark}}{I - I_{dark}} + 0.429 \cdot \left(\frac{I_{ref} - I_{dark}}{I - I_{dark}}\right)^2 - 0.065 \cdot \left(\frac{I_{ref} - I_{dark}}{I - I_{dark}}\right)^3 = \frac{P}{P_{ref}} \tag{3.2}$$

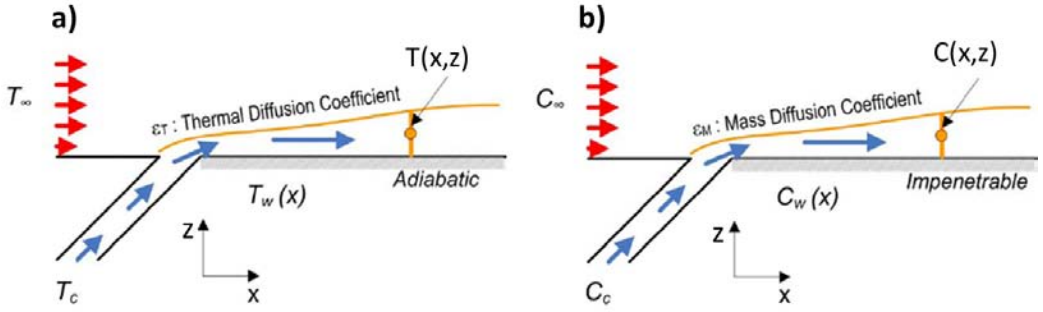

Figure 3.6: Heat and mass transfer analogy for film cooling situations: thermal (**a**) and mass transfer (**b**) boundary conditions [88]

3.2.2 Measurement Theory

Starting from a simple 2D film configuration reported in Fig. 3.6a, the governing equation for the heat transfer into a turbulent boundary layer is, Eq. 3.3:

$$G_x \frac{\partial T}{\partial x} + G_z \frac{\partial T}{\partial z} = \rho \left(\epsilon_T + \alpha\right) \frac{\partial^2 T}{\partial^2 x} \tag{3.3}$$

where G is the mass flux per unit of area, ϵ_T and α are respectively the turbulent and laminar diffusivity. The boundary conditions in case of adiabatic wall are, Eq. 3.4:

$$\begin{aligned} z = 0 \quad &\Rightarrow \quad T = T_{ad}; \quad \frac{\partial T}{\partial z} = 0 \\ z > \delta_f \quad &\Rightarrow \quad T = T_\infty \\ x = 0 \quad &\Rightarrow \quad T = T_c \end{aligned} \tag{3.4}$$

Now consider the analogous case for mass transfer situation, where the hot mainstream has a tracer element concentration of C_∞ and the coolant has a tracer concentration of C_c (Fig. 3.6b). For this situation, the governing equation of tracer gas diffusivity inside the concentration boundary layer are, Eq. 3.5:

$$G_x \frac{\partial C}{\partial x} + G_z \frac{\partial C}{\partial z} = \rho \left(\epsilon_C + D\right) \frac{\partial^2 C}{\partial^2 x} \tag{3.5}$$

here the ϵ_C represents the turbulent mass diffusivity. An impenetrable wall situation leads to the following boundary conditions, Eq. 3.6:

$$\begin{aligned} z = 0 \quad &\Rightarrow \quad C = C_w; \quad \frac{\partial C}{\partial z} = 0 \\ z > \delta_f \quad &\Rightarrow \quad C = C_\infty \\ x = 0 \quad &\Rightarrow \quad C = C_c \end{aligned} \tag{3.6}$$

It is easy to observe that the set of equations for heat and mass transfer situations have same modelling expression [90]. Moreover, if the boundary conditions of the two analogous problems are the same and if the molecular and turbulent Schmidt number Sc_T are identical to molecular and turbulent Prandtl number Pr_T respectively (i.e. turbulent Lewis number Le_T equal to one), the solutions of the heat and mass transfer phenomena are identical, Eq. 3.7:

$$Le_T = \frac{Pr_T}{Sc_T} = \frac{\epsilon_T + \alpha}{\epsilon_C + D} \approx 1 \tag{3.7}$$

In turbulent flows, experimental results suggest that the coefficients of turbulent transport diffusivity, represented by the Sc_t and Pr_t numbers, have similar magnitudes [91].

Concerning the applicability of the heat and mass transfer analogy to film cooling situations with moderate Mach number, turbulent main flow and high blowing rate multiple injections, the mixing process of interested is generally situated far from the wall, where turbulence effect are dominant, and therefore the analogy is generally satisfied.

Even if the hypothesis of turbulent Lewis number is met ($Le_t = 1$), the similarity of molecular diffusion may not be satisfied and thus Lewis number may deviate from one: in this case, the difference between Pr and Sc influences the heat/mass transfer rate only near the wall boundary layer in the thin viscous sub-layer [90]. However, only a small influence of molecular parameters is expected as a consequence of the zero temperature/concentration gradient at the adiabatic/impenetrable wall of the test plate.

Despite the fact that the applicability of heat and mass transfer analogy has limitations, especially for fluid field where viscous effects dominate (e.g.. film cooling at blade leading edge), it represents a good approximation for test cases as encountered in the present work.

3.2.3 The PSP Mass Transfer Analogy to Determine Film Effectiveness

In the recent years the pressure sensitive paint has been employed for adiabatic effectiveness measurements in studies which involve very different flow conditions such as endwall [92], rotating leading edge [93] and blade cooling system in annular cascade using real engine hardware as shown by the author [94]. In all these studies PSP has proven to be a very powerful experimental technique, able to achieve highly detailed results.

Since the PSP is a sensor of the oxygen concentration, this paint is suitable for gas concentration technique based on the heat and mass transfer analogy [95] (Cfr. 3.2.2).

Assuming valid the analogy [96], if a tracer gas without free oxygen is used as coolant in a film cooling system it is straightforward to replace the temperature definition of film cooling effectiveness by mass fractions of oxygen [95]:

$$\eta_{ad} = \frac{T_{main} - T_{ad}}{T_{main} - T_{cool}} \equiv \frac{C_{main} - C_w}{C_{main}} \tag{3.8}$$

Here C_{main} is oxygen concentration of main free stream and C_w is the oxygen concentration in proximity of the wall. In order to express Eq. 3.8 in terms of partial pressure of oxygen as measured with PSP, the expression of adiabatic effectiveness is elaborated using the molecular weights [92]:

$$\eta_{ad} = \frac{C_{main} - C_w}{C_{main}} = 1 - \frac{1}{\left(1 + \left(\frac{P_{O_2;air}/P_{O_2;ref}}{P_{O_2;fg}/P_{O_2;ref}} - 1\right)\frac{W_{fg}}{W_{air}}\right)} \tag{3.9}$$

In the previous equation, the subscript fg and air stand, respectively, for the case with foreign (tracer) gas and air injection trough cooling system; moreover ref is used to identify a reference case. In the case $W_{fg}/W_{air} \approx 1$, as for nitrogen injection, the Eq. 3.9 reduces to:

$$\eta_{ad} = \frac{C_{main} - C_w}{C_{main}} = 1 - \frac{P_{O_2;fg}/P_{O_2;ref}}{P_{O_2;air}/P_{O_2;ref}} \tag{3.10}$$

In order to evaluate the adiabatic effectiveness distribution using PSP technique four types of images are needed for each tested flow condition; the experimental apparatus must be equipped with the same illumination system and camera used for calibration test. Each type of image is evaluated as an average of at least 10 images to reduce measurement noise.

1. The first image (*Dark Image*) is acquired with the UV illumination system switched off and it is necessary to correct the background noise of the camera CCD (I_{dark}).

2. Using a tracer gas for the cooling line and air for the mainstream, a second image (*Air Image*) is acquired setting the desired flow conditions.

3. The third image (*Tracer image*) is acquired imposing the same conditions of the previous one, but using air as coolant instead of tracer gas.

4. The last type of image (*Ref Image*) is captured with no flow condition and it represents the reference intensity field of the measurements (I_{ref}).

Coolant and mainstream are set at the same room temperature for all the tests. From the ratio of the reference (I_{ref}) and tests 2 intensity images, both corrected with the dark field (test 1), the calibration curve can be used to estimate pixel by pixel the normalized partial pressure of oxygen in case of tracer gas injection through holes array ($P_{O_2;fg}/P_{O_2;ref}$). In the same way the intensity image acquired with the third test (air injection) is elaborated

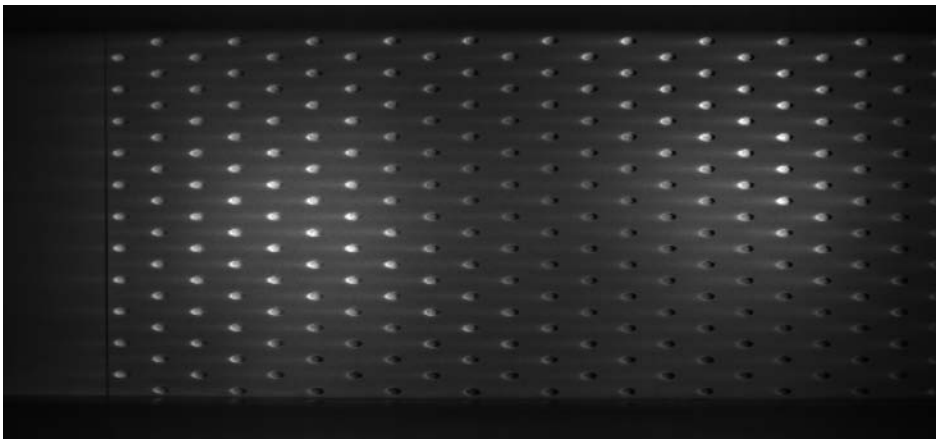

Figure 3.7: Response of PSP injecting tracer gas in an effusion cooling system

in order to achieve the ratio $P_{O_2;air}/P_{O_2;ref}$. Finally both the distributions of partial pressure of oxygen are combined, as suggested by Eq. 3.10, to estimate the bidimensional map of adiabatic effectiveness. Generally the final map is also filtered using an algorithm based on 2D Fourier Transform to smooth the results. An example of a raw intensity image acquired with injection of tracer gas is depicted in Fig. 3.7.
A schematic description of the experimental procedure is summarized in Fig. 3.8, the post process procedure is performed through an integrated procedure developed in LabView®and MatLab®environments.

An important aspect of the PSP technique is that it allows to perform tests which can be considered really adiabatic. In the case of a thermal technique such as IR, TLC or TSP thermography [97], the adiabaticity is guaranteed when there are not thermal gradients across the test plate; this requirement can be only partially satisfied using a low conductive material. On the other hand, when the heat and mass transfer analogy is employed, the adiabaticity is guaranteed when there are not oxygen concentration gradients inside the test plate: as a consequence, since in the PSP technique the test plate has an impenetrable wall, except for the thin layer of PSP coating, tests can be considered really adiabatic. Other pros of the PSP technique are the high resolution of the results and the reduced experiments time due

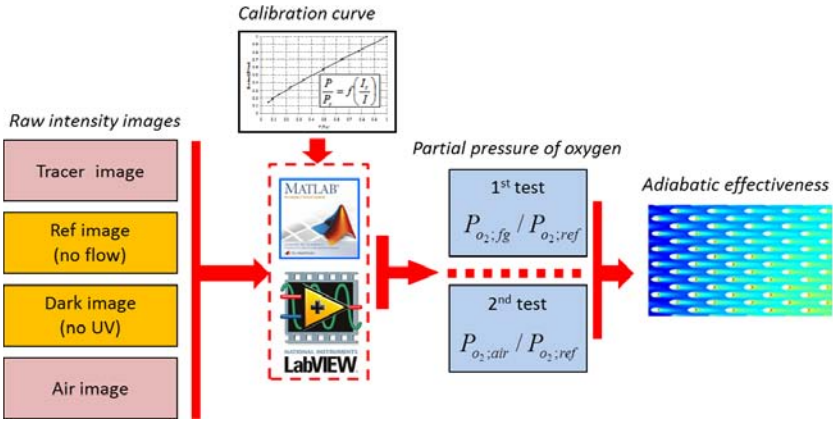

Figure 3.8: Adiabatic effectiveness measurements using PSP technique

to high response time. In fact, the space resolution of the measurements is practically coincident with the camera resolution and the response time is in the order of microseconds. Both these characteristic are governed by the diffusion of oxygen inside the thin layer of paint binder. A comparison between PSP and TLC techniques for adiabatic effectiveness measurements has been performed by the author [98] highlighting the pros and cons of the techniques.

3.3 Overall Effectiveness Measurements

For the first experimental investigation reported in this work, overall effectiveness tests are carried out. As will be explained in the following Chapters, measurements are performed on multi-perforated tests plate made of conductive material, selected to achieve Biot similarity.

The steady state technique used to evaluate the overall distributions is based on temperature measurements of the conductive plate, heating up the mainstream by means of an electric heater up to approximately $330K$, and using coolant at room temperature.
Starting from the definition of Overall Effectiveness, the measurements require to know different values of temperature, Eq. 3.11:

$$\eta_{ov} = \frac{T_{main} - T_w}{T_{main} - T_{cool}} \tag{3.11}$$

For this reason the experimental apparatus used in the first part of the current research (Cfr. 4.1) is equipped with several thermocouples. The temperature of mainstream (T_{main}) is evaluated averaging the reading of two thermocouples located normal to the flow $\approx 80mm$ upstream the coolant injection. The temperature of the coolant (T_{cool}) is estimated by means of a thermocouples inside the plenum chamber used to feed the effusion cooling system. Finally

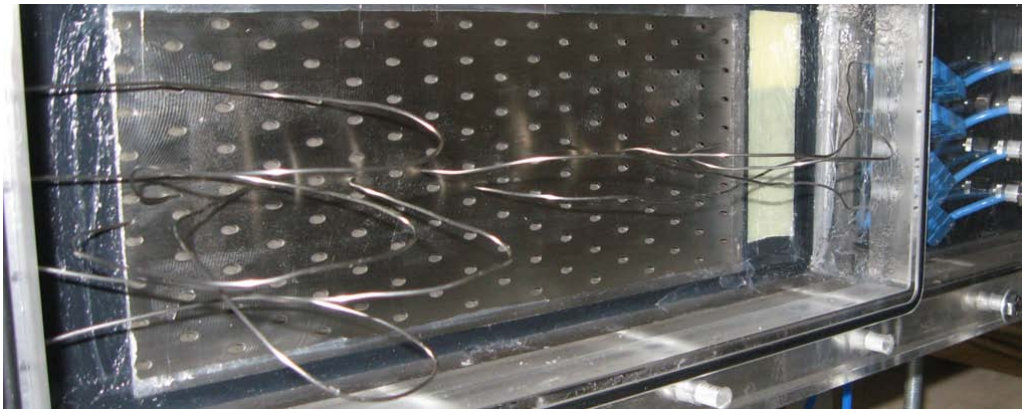

Figure 3.9: Effusion plate equipped with thermocouples for wall temperature measurements for η_{ov} tests

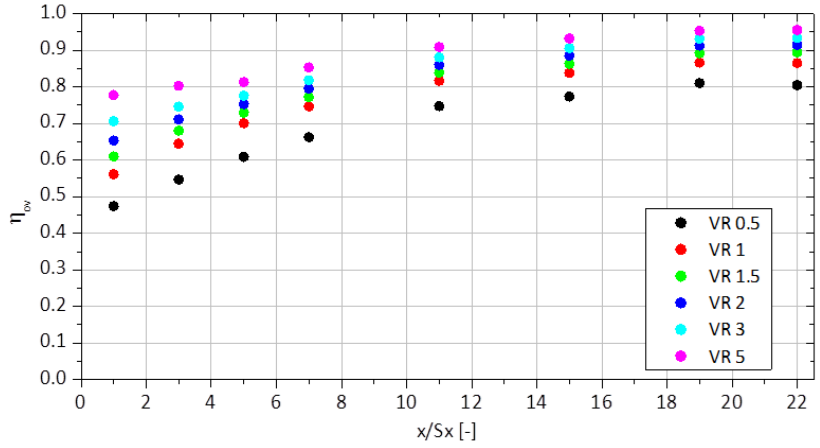

Figure 3.10: Example of overall effusion measurements at different VR

the temperatures of the wall (T_w) is evaluated using eight thermocouples embedded inside the test plate. These are housed in as many dead holes on the plenum side of the plate, about 2 mm below the investigated surface along the centreline. In fig. 3.9 it is possible to observe the coolant side of an effusion test plate equipped with thermocouples. Thermally conductive grease is used to ensure the contact between the thermocouples and the effusion plate. In addition, the high conductivity material of the effusion plate allows to use the temperature detected by the thermocouple as the local temperature of the wall surface on gas side.

Setting the desired flow conditions the tests are run after steady condition is reached by all the measured quantities: flow rates, pressures and temperatures. The same experimental procedure was used in the work of Ceccherini et al. [99] and Oguntade et al. [100].
An example of result obtained on a effusion test plate is reported in Fig. 3.10, the measurements technique provides discrete results in correspondence of the thermocouples. For each flow conditions an averaged η_{ov} value is resolved starting from the overall measurements along the centreline ($\eta_{ov;i}$); it is estimated as weighted mean using the locations of the TCs (x_i) and their reciprocal distance along the center of the plate to estimate the weights,

Eq. 3.12:

$$\eta_{ov} = \frac{\sum_i w_i \cdot \eta_{ov;i}}{\sum_i w_i}; \begin{cases} w_i = (x_{i+1} - x_{i-1})/2 & i = 2 \dots 7 \\ w_1 = (x_2 + x_1)/2 \\ w_8 = L - (x_8 + x_7)/2 \end{cases} \tag{3.12}$$

where $i = 1 \dots 8$ is the index associated to one of the eight thermocouples ($i = 0$ for TC located at $x/S_x = 0$ and $i = 8$ for TC at last row of holes); L is the perforation length. This approach is based on a linear variation of effectiveness between each thermocouples location and gives an averaged value that can be used to compare the performance of different effusion geometries with same perforation length.

3.4 Heat Transfer Coefficient measurements

In the second part of the present work, HTC measurements are performed on a multi-perforated plate by means of a steady state technique using thermochromic liquid crystal.

3.4.1 TLC measurement technique

A brief mention on thermochromic liquid crystals (TLC) it's now to be made. In different research fields TLC have been diffusively employed as an effective tool to visualize temperature distributions on solid surfaces and in the last two decades many heat transfer measurements have been performed through such a fascinating means. The capability of Thermochromic Liquid Crystal of displaying different colors at different temperatures depends on selective reflection of certain wavelengths by the crystalline structure of the material.
With respect to other heat transfer measurements technique, there are few advantages provided by the use of TLC. Unlike traditional methods, TLC offers a non intrusive method, with negligible interaction with the flow field, able to provide continuous information on the whole test surface. On the contrary the use of thermocouples to monitor the temperature give information at discrete points, as reported describing the overall effectiveness technique (Cfr 3.3). These peculiarities make the TLC technique an attractive method for heat transfer measurements especially in studies which involve complicated geometries with high heat transfer gradient such as gas turbine cooling system.

The liquid crystals used in the current study are wide band TLC 30C20W supplied by Hallcrest and active from about $30°C$ to $50°C$. The active substance of the liquid crystal is encapsulated into a polymer layer that provides protection against the environmental light that could damage it reducing the lifetime. The paint is thinned with water and sprayed over the desired test surface using an air gun, generally a black coating is used to provide the proper background for TLC.

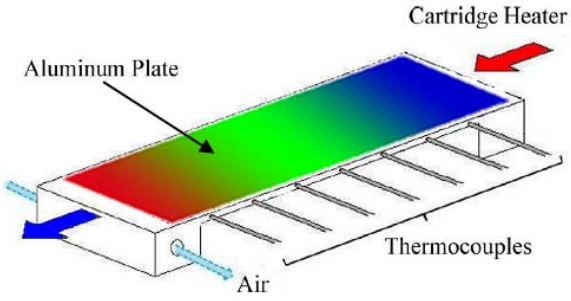

Figure 3.11: Setup for TLC calibration

When the surface is heated up and the temperature goes over the activation temperature, the active substance star to reflect light from the long wavelength to the short wavelength: the first color is the red and as heating continues (i.e. the surface temperature increases), the color passes through the visible color spectrum to yellow, green and ultimately reaches blue. A further heating with temperature over $\approx 50°C$ the TLC color will disappear. Among many TLC techniques used for temperature measurements, the steady-state, Hue-capturing method is adopted in this study. The Hue angle is maybe the most employed color characteristic for analyse the TLC color play as far as wide band crystals are considered. Starting from the polar chromaticity space defined by the intensity of the red, green and blue channels (R, G and B values) the Hue can be computed as, Eq. 3.13 [101]:

$$Hue = \arctan\left(\frac{\sqrt{3}(G-B)}{2R-G-B}\right) \tag{3.13}$$

TLC Calibration Procedure

A robust TLC color-temperature response calibration is necessary for high-accuracy measurements. When temperature is measured with the TLC, extra care has to be taken to fix all the conditions identical to the calibration to avoid the color variation problem due to the lighting/viewing arrangement. The TLC calibration has been conducted following the steady state gradient method (Chan et al. [102]). The calibration setup is made by a $4.5mm$ thin

aluminium rectangular plate, sprayed with black background paint and then TLC, which houses seven thermocouples. One of its edges is heated by an electric heater, while the other is cooled by air. The whole apparatus is placed into an insulating basis (Fig. 3.11).

A linear temperature gradient will appear on TLC surface: once steady conditions are reached, a single picture is sufficient for a precise measurement of color-temperature response, with the latter parameter measured through thermocouples. A digital camera (Sony XCD-SX90CR) is used to capture color images (1185x889 pixel) from the TLC painted surface; the illuminating system, composed by two LED tubes 18 Watt ($5500K$ temperature color), ensures an uniform illumination on the test surface and allows to keep both color temperature and light power constant.

This arrangement allows an entire TLC hue-temperature calibration curve to be computed from a single image. However, several tests have been carried out, so as to increase global precision. The choice of "hue" as the color detector is due to the fact that this parameter is less sensitive to measurement conditions (e.g. light intensity) with respect to others; moreover, as it is shown in calibration curve of Fig. 3.12, its dependency from temperature is monotonic inside the activation range of TLC [103].

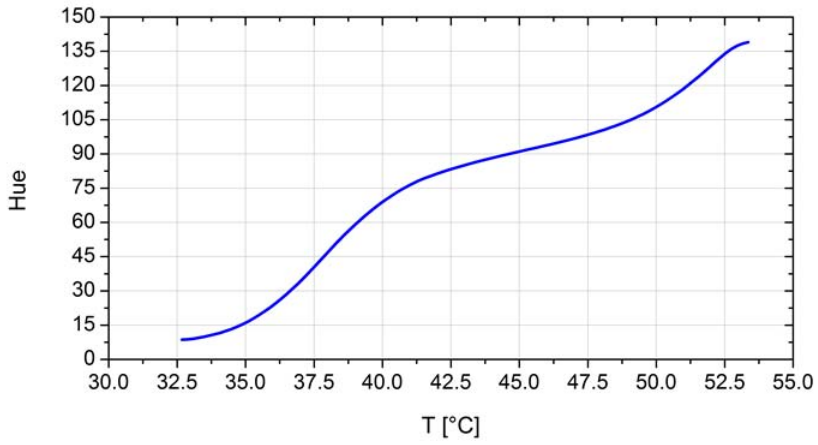

Figure 3.12: TLC calibration curve

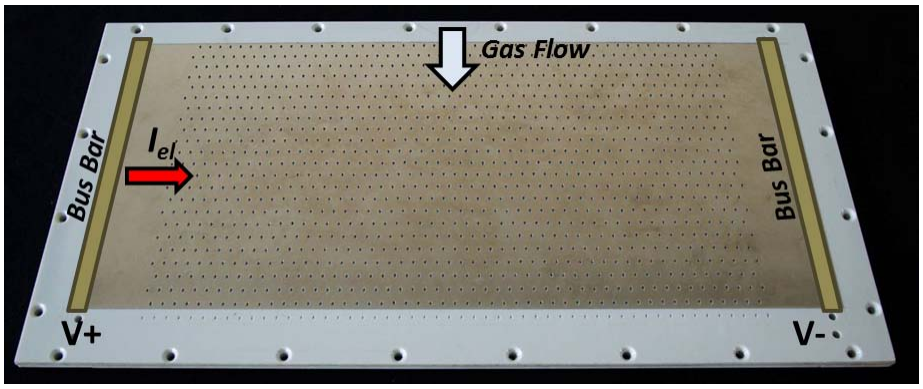

Figure 3.13: Effusion test plate with multi-perforated heating foil

3.4.2 Experimental Procedure

Heat transfer coefficient distributions are determined by a steady-state technique, using TLC paint to measure the wall temperature. The liner plate was made in low conductivity material and covered with a thin heating foil made of Inconel 600 (thickness $0.0254mm$). The Inconel sheet is electrically supplied by two lateral copper bus bars (current flows along the lateral direction) connected to a low voltage generator AGILENT®N5763A Programmable DC Power Supply. It should be remarked that, in presence of multi-perforated plate, the sheet has exactly the same hole pattern of the plate as can be observed in Fig. 3.13.

By setting the input current or voltage, the heating foil is used to provide the desired level of surface heat flux. Using mainstream and coolant at room temperature, the TLC color play on the liner surface is directly linked to the local value of HTC: region with high surface temperature (blue color) means low heat transfer coefficient and vice-versa.
For each desired flow condition, the digital camera records a raw bitmap image from the painted surface on a PC (IEEE-1394 standard), while the illuminating system ensures an uniform illumination as done in the same way during the calibration. The acquisition is done after steady conditions are reached by all the measured parameters (about 1 hour).

The post processing procedure of the acquired images is performed by a MatLab®in-house code. Starting from the bitmap the images are converted

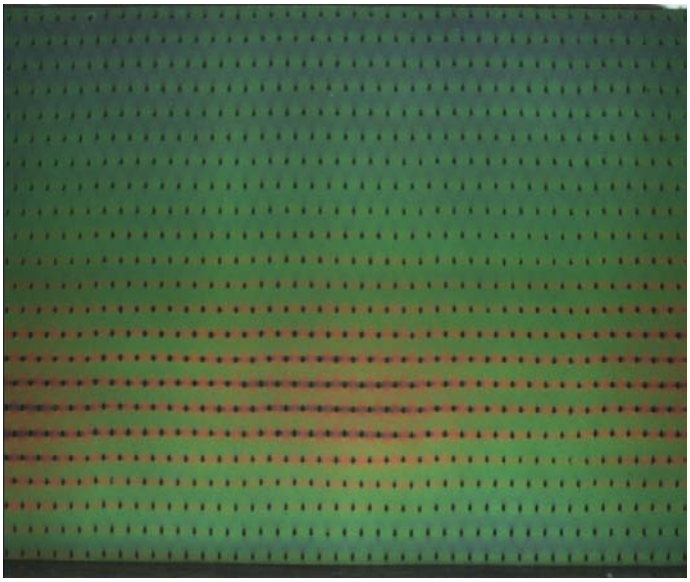

Figure 3.14: TLC color play on an effusion test plate

into color map exploiting a demosaicing algorithm. The aim of this procedure is to reconstruct full color images from the spatially under-sampled color channels: the output of the procedure is an RGB map for each flow condition. After that, a built-in function of MatLab®environment image package **RGB2HSV** transforms the R, G and B matrices into a hue matrix using the hue definition based on Eq. 3.13. Finally, it is straightforward to use the calibration curve to compute the temperature map that represents the basis for the calculation of HTC distributions.

An example of TLC color play is reported in Fig. 3.14.

3.4.3 Data Reduction

The experimental procedure and the first part of the post-processing procedure described above allow to estimate the surface temperature distribution over the liner test plate. The next step is the calculation of HTC, a description of the post-processing procedure developed an adopted for data reduction is given.

The heat transfer coefficient is defined as follow:

$$HTC = \frac{\dot{q}_{conv}}{T_w - T_{aw}} \tag{3.14}$$

where the T_{aw} represents the surface temperature of a perfectly insulated wall. As the mainstream Mach number is low, recovery effects can be neglected and therefore the mainstream temperature, measured with thermocouples upstream the test section, is used as adiabatic wall temperature. T_w is recorded during the experiments by means of TLC as described in previous section; q_{conv} represents the heat rate exchanged by convection between the test plate and the mainflow. It can be locally computed knowing the heat generated by Joule effect, $\dot{q}_{Joule}$, and the heat loss through conduction across the test plate $\dot{q}_{loss}$, Eq. 3.15:

$$\dot{q}_{conv} = \dot{q}_{Joule} - \dot{q}_{loss} \tag{3.15}$$

In fact, a fraction of the heat generated by Joule effect is not exchanged by convection and represents the heat loss due to conduction through the plate and the following convection on its back side and inside the effusion holes (heat sink effect). Despite the low conductivity material of the plate, the heat loss represents a not negligible quantity. Typical heat flux input values, calculated using the resistance ratings of the heater and the voltage settings on the power supply, are $2000 - 3000 W/m^2K$.

Knowing the wall and mainstream temperatures directly measured by TLC and thermocouples, Eq. 3.14-3.15 suggest that that two other quantities must be estimated to compute the heat transfer coefficient:

1) $\dot{q}_{Joule}$: in case of multi-perforated plates the imprints of holes deeply affect the distribution of heat generated by the heating foil. Current concentrations are expected between the rows of holes.

2) $\dot{q}_{loss}$: the heat loss due to the conduction is affected by the presence of the heat sink effect that generates three dimensional conduction phenomena within the plate thickness.

These two quantities could be estimated by means of a thermoelectric 3D FEM analysis combined with a 1D conduction model as reported in the procedure developed by Maiuolo et al. [81]. However for test plate with a large number of holes like the case encountered in the present research (1236 holes), a complete 3D Thermoelectric FEM simulation is not a feasible solution in terms of computational cost. In addition, it requires to know the cooling mass flow distribution among the effusion holes to estimate the heat transfer inside the perforations. For the reasons reported above a simplified approach is developed and validated having in mind the aim of achieve a reliable data reduction procedure.

3.4.4 Post-Processing Procedure

The final aim of the post processing procedure is the evaluation of the thermal flux across the plate ($\dot{q}_{loss}$) and the distribution of heat generated by the heating foil ($\dot{q}_{Joule}$). These quantities distributions are necessary to calculate the HTC by exploiting point by point the formulation reported in Eq. 3.14 and the approach discussed in section 3.4.3.
To understand the thermoelectric behaviour of the plate with the Inconel heating foil, two different simulations are performed using the commercial code ANSYS® 14: the first simulation is an electric 2D FEM of the multi-perforated heating foil and the second is a 3D simulation of a portion of the liner plate with the Inconel sheet.

Electric FEM Analysis of Inconel Heating Foil

The first simulation is aimed at deepening the influence of the hole pattern on current distribution. In order to reduce the computational cost, a portion of the complete sheet, depicted in Fig. 3.13, is tested exploiting the symmetry of the problem. The FEM analysis is performed using *Shell 157* 2D element type that has the voltage as degree of freedom in its formulation. The boundary condition is the voltage drop applied at sheet extremities. The result in terms of $\dot{q}_{Joule}$ distribution is reported in Fig. 3.15, it is clear that the effusion perforation produce region with both high and low current

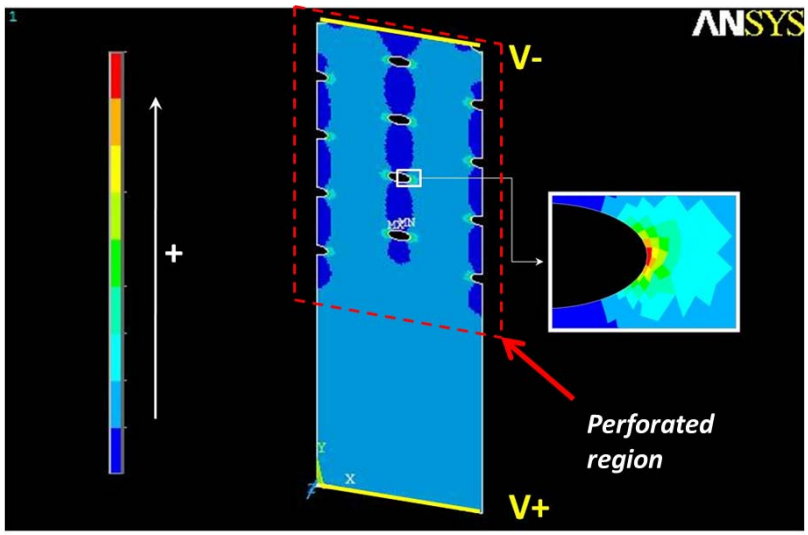

Figure 3.15: Distribution of heat generated by Joule effect in a portion of the Inconel heater

value, nevertheless between the rows of hole the distribution is more uniform. Moreover elaborating the results, it has been estimated that in the regions between the rows of holes the surface heat flux is 5% greater than the average heat flux that affects the perforated region indicated in Fig. 3.15 with red dotted line.

This behaviour suggests that in the zones between each row of holes is possible to estimate the value of $\dot{q}_{Joule}$ knowing the voltage and the current imposed during the test and by means of simple energy balance approach. Thanks to the bus bars that provide an uniform input voltage on the lateral sides of the heater (Fig. 3.13), the Inconel sheet is reduced as a series of electric resistances (Fig. 3.16) where the central resistance represents the portion of the sheet with the holes while the two lateral can be easily computed using the well known relation, Eq. 3.16:

$$R_{smooth} = \frac{\rho_{el} l}{s} \tag{3.16}$$

where ρ_{el} represents the electric resistivity of the Inconel 600, known thanks to the material data-sheet and verified with dedicated experiments, while s and l are the respectively the thickness and the cross-sectional area of the

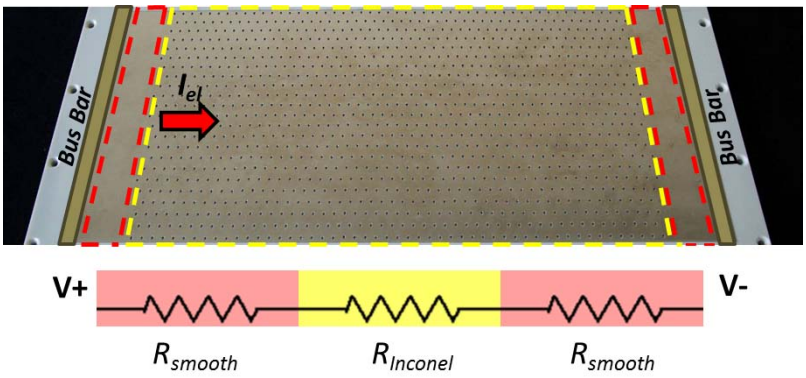

Figure 3.16: Electric model of Inconel heating foil

portion of the heather. During the experiments, for each testing condition the voltage applied to the bus bars and the current flow are acquired; using basic electrical equation based on the Ohm's law and to the "voltage divider" relations, the value of the surface heat flux in the bands between the rows of holes can be computed, Eq. 3.17:

$$\dot{q}_{Joule} = I_{el}^2 \cdot \frac{\left(\frac{V^+ - V^-}{I_{el}} - 2 \cdot R_{smooth}\right)}{A_{heater}} \cdot 1.05 \tag{3.17}$$

where the factor 1.05 is used to take into account the current concentration estimated during the FEM analysis and A_{heater} is the active surface of the multi-perforated region associated with the resistance $R_{inconel}$.

Thermoelectric FEM Simulation

A thermo-electric FEM simulation of a portion of the liner plate is carried out, the objective is to calculate a temperature distribution on the liner surface that can be used to stress the post processing procedure.
Steady state FEM calculation is performed on a periodical section of the tested geometry. The model includes the test plate and the thin heating foil, it has been meshed with about 150000 elements imposing adiabatic conditions on the plate lateral sides. *SOLID 69* eight nodes elements are used, they have as degree of freedom the voltage and the temperature value

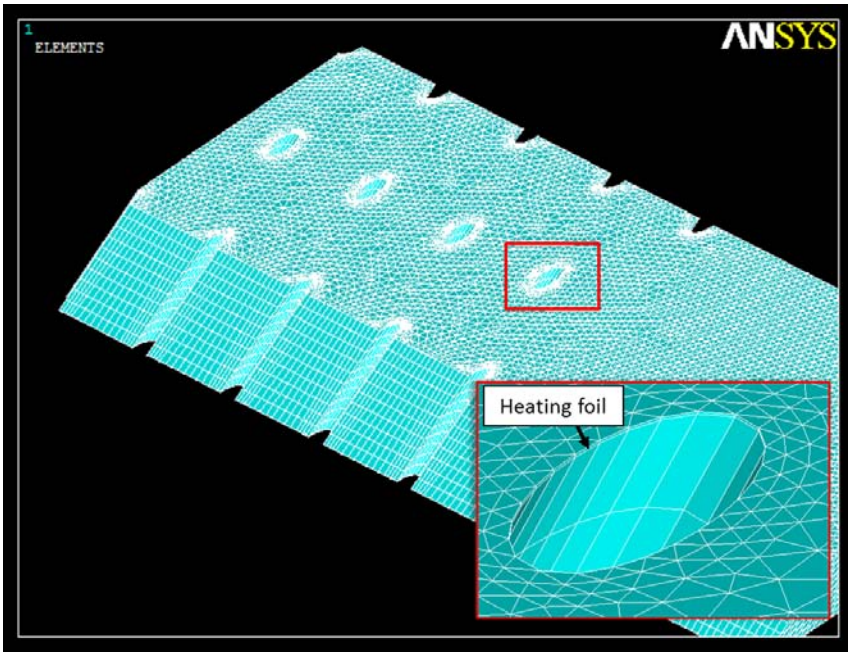

Figure 3.17: Mesh of multi-perforated plate

(Fig. 3.17).

Boundary conditions of FEM are imposed as follow, reproducing typical conditions expected during the experiments:

- Holes interior: a convective load is applied. HTC_{hole} is evaluated by means of proper correlation for turbulent flow considering an expected value of cooling mass flow ($HTC_{hole} = 460 W/m^2K$). The temperature of the flow is set at room temperature ($300K$).

- Coolant Side: convective load is applied. Heat transfer coefficient is fixed at $20 W/m^2K$ and coolant temperature at room temperature. Anyway, this thermal load has a very low influence on the final result as the temperature difference between coolant and surface is negligible.

- Hot gas side: a constant value of the HTC_{main} is imposed. This assumption is consistent with the experiments reported by Baldauf et al. [104] on a single row of hole: in penetration regime the HTC distribution is approximately constant except for a very small and negligible

area around the hole. The convective mainstream temperature is set in the simulation equal to the room temperature, while HTC_{main} is fixed at $172 W/m^2K$ exploiting the results of a previous test campaign [57].

- Inconel heating foil: on the lateral edges of the portion of the heater a constant voltage values is applied. The resulting voltage drop is adjusted using an iterative procedure in order to achieve from the simulation a temperature distribution falling in the activation range of liquid crystal (Cfr. 3.4.1).

- Cyclic conditions are applied on the inclined streamwise faces of the test plate. This condition imposes the same temperature values on the correspondents nodes of the cyclic faces. To apply this condition care must be applied during the meshing procedure in order to generate the same node division on cyclic faces.

The properties of the material in term of electric and thermal conductivities are set based on the data-sheets of the manufacturer. The thermal conductivity of the perforated test plate, made of Arnite, is measured by certified research center at $20°C$ and $60°C$: a value of $k = 0.247 W/mK$ is reported in both the conditions.

The simulation is run iterating on the voltage drop across the heating foil stopping the simulation when the surface temperature are in the activation range of TLC. The obtained temperature distribution is representative of temperature that could be detected by liquid crystal during the experiments. The benefit of this simulation is that we have a temperature distribution associated with an HTC_{main} which is the variable unknown during the tests. The temperature distribution can be used to stress post processing procedures having in mind that the exact distribution of HTC is a constant value of $172 W/m^2K$.

The temperature distribution on the liner surface extracted by the simulation results is reported in Fig. 3.18: it is deeply affected by the non uniform Joule effect (Fig. 3.15) and by the heat sink effect that despite the low conductivity of the Arnite produces halos in the regions around the imprints of the holes.

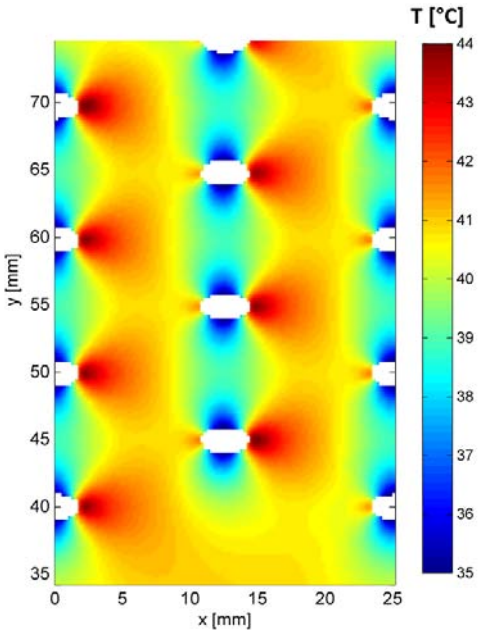

Figure 3.18: Expected temperature distribution on liner surface calculated by means of FEM simulation

1D Model for Data Post Processing

The previous results in terms of temperature distribution can be used to test a 1D conductive model that exploits also the electric FEM simulation of the heating foil.

The temperature distribution on the liner surface points out that the regions around the holes are clearly affected by the current concentration and by the heat sink effect. With the object of developing a fast and reliable procedure, only the bands in the lateral direction located between each rows of holes are considered in the post processing procedure excluding the areas located 1/4 of the streamwise pitch upstream and downstream each rows. In these zones, the aforementioned effects are more intensive and hard to estimate during the post process.

Calculating the term $\dot{q}_{Joule}$, using the Eq. 3.17, and the heat loss through a simple 1D conduction model (conduction trough the test plate and natural convection on the back side and neglecting the heat sink effect), the temperature matrix can be reduced to an HTC distribution using point by

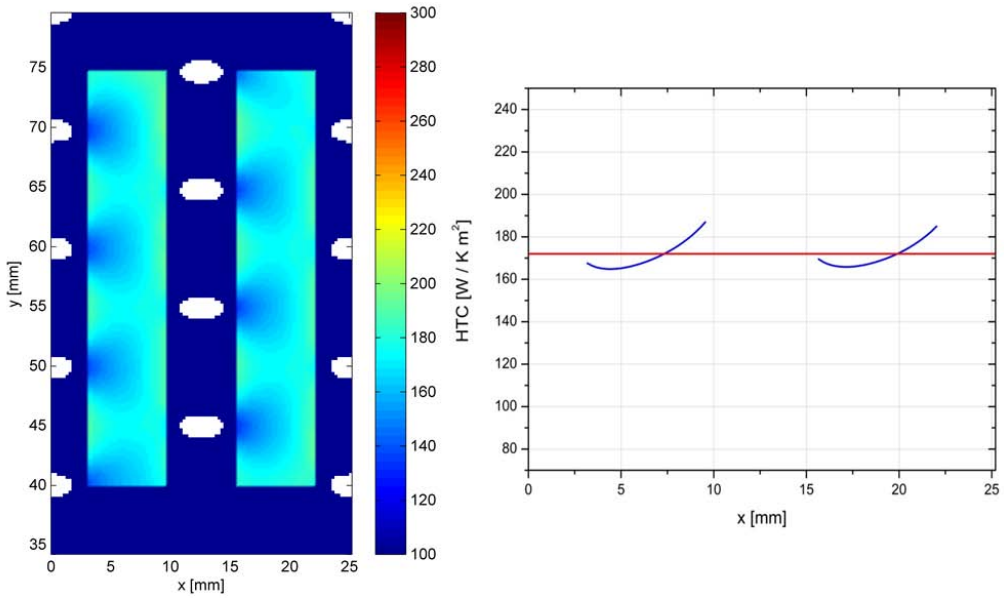

Figure 3.19: Results of 1D post processing procedure based on temperature distribution estimated through FEM simulation

point the basic relation of Eq. 3.14. Results of the present post processing approach is reported in Fig. 3.19, highlighting in the lateral averaged trend the constant target value of $172 W/m^2K$ imposed during the FEM simulation (red line). The average HTC value on the investigated bands between each row is $171.2 W/m^2K$, very close to the target value.
The survey points out that a 1D approach is a reliable method for the data reduction if it is not included the area near the holes, deeply influenced by non uniform surface heat flux and by the forced convection inside the perforation. Moreover it validates the approach for the data reduction adopted in the current research and summarized below:

1) The TLC color play is reduced using calibration curve into a temperature distributions (Cfr. 3.4.2).

2) The electric voltage and current applied to the heater are used to estimate a constant mean value of $\dot{q}_{Joule}$ using the relation Eq. 3.17.

3) The temperature distribution is divided into regions according to the

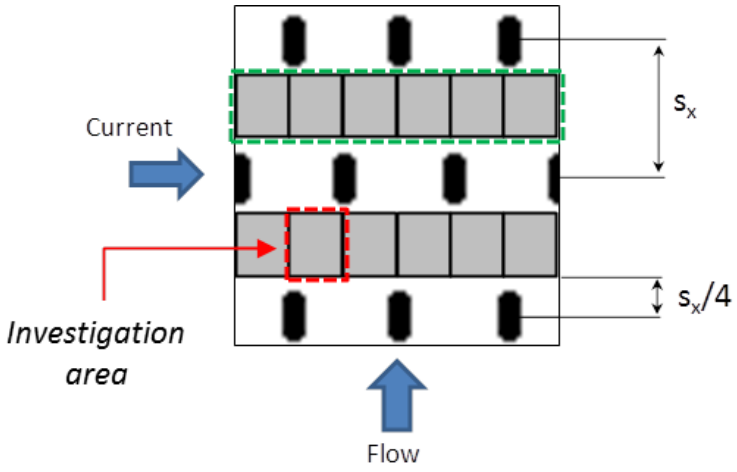

Figure 3.20: Investigation areas for *HTC* post processing procedure

hole pattern excluding the near-holes zones identifying several investigation areas (Fig. 3.20).

4) For each investigation areas an average value of *HTC* is estimated using the Eq. 3.14 and assuming a 1D conduction model, for the evaluation of the term $\dot{q}_{loss}$, in which the contribution of the heat sink effect is neglected. The average *HTC* value is associated to the coordinates of the centroid of each investigation cell.

5) Using the results of the previous step the results are interpolated on the whole liner surface obtaining a distribution with the same resolution of the TLC image used at point 1. The interpolated matrices are finally masked with the hole pattern.

The described procedure is able to answer to the requirements of developing a fast and reliable procedure, nevertheless the main drawback is the loss of resolution around the holes.

It is worth to notice that in case of smooth test plate with no perforation pattern, the post processing procedure can follow with sufficient accuracy a 1D approach without excluding areas from the post process. In this simplified case the heat is uniformly generated by the heating foil and it can be

estimated dividing the total input power by the total area of the heater. In addition, to obtain the distribution of $\dot{q}_{conv}$ on the surface of the test plate, for each pixel of the recorded image the 1D conduction approach can be employed to estimate the overall losses and then subtracted to the total surface heat flux.

3.5 Measurements Uncertainties

Uncertainties associated to direct measurements, inevitably affect the evaluated quantities values, that are obtained by properly combining the former ones (e.g. adiabatic effectiveness, overall effectiveness, mass flow rate). The average experimental uncertainty may be computed through the following procedure proposed by Bell [105], based on the Kline and McClintock method [106].
Let's call G the observed quantity, known function of n independent variables, g_i, which in turn characterised by uncertainties. Suppose that the each g_i quantity, directly measured during experiments, is statistically described by a Gaussian distribution with a standard deviation σ_i, and the final variable G has a total deviation σ, Eq. 3.18:

$$\begin{aligned} G &= f\left(g_1, g_2, \ldots, g_i, \ldots, g_n\right) \\ G \pm \sigma &= f\left(g_1 \pm \sigma_1, g_2 \pm \sigma_2, \ldots, g_i \pm \sigma_i, \ldots, g_n \pm \sigma_n\right) \end{aligned} \tag{3.18}$$

Data-sheets of most of instruments reports the uncertainties usually with a level of confidence of 95% referring to a Gaussian distribution. For this case the standard deviation σ_i of the input quantity g_i, can be easily computed dividing the provided uncertainties for a "coverage factor" of 2.

The influence of the single deviation standard σ_i on the final observed quantity G depends on the relation f with the input parameters. Calling u_i the parameter that express how each input quantity feeds into the final results, it can be calculated following the method of Kline and McClintock [106], based on partial derivative approach, Eq. 3.19:

$$u_i = \sigma_i \cdot \frac{\partial f}{\partial g_i} \tag{3.19}$$

The uncertainty of the final quantity depends not only by the u_i parameters but it is also affected from other aspects. The most important is the standard uncertainties of repeated readings. Let's suppose that the final quantity G is measured z times (at least 10 times in the present work) and that the

	Variable	Exp. Technique	Uncertainty	Units
d	Hole Diameter	-	$\pm 2\%$	$[-]$
T	Temperature	Thermocouples with reference joint	± 0.5	$[K]$
P	Pressure	Pressure taps DSA3217 15psi	± 51	$[Pa]$
$\dot{m}_{cool}$	Cooling mass flow	Orifice/Calibrated Nozzle	$\pm 4\%$	$[-]$
$\dot{m}_{main}$	Main mass flow	Orifice	$\pm 3\%$	$[-]$
BR	Blowing Ratio	-	$\pm 5\%$	$[-]$
VR	Velocity Ratio	-	$\pm 5\%$	$[-]$
η_{ad}	Adiabatic Effectiveness	PSP technique	$\pm 2\%$ for $\eta_{ad} > 0.8$ $\pm 10\%$ for $\eta_{ad} = 0.2$	$[-]$
HTC	Heat Transfer Coefficient	TLC technique	$\pm 10\%$	$[-]$
η_{ov}	Overall Effectiveness	TCs technique	$\pm 2\%$ for $\eta_{ad} = 0.8$ $\pm 5\%$ for $\eta_{ad} = 0.3$	$[-]$

Table 3.1: Uncertainty analysis (results reported with a level of confidence of 95%)

standard deviation of the sample is U; the contribution of this aspect to the final uncertainty u_z is, Eq. 3.20:

$$u_z = \frac{U}{\sqrt{z}} \tag{3.20}$$

In most cases the contribution of u_z is very small compared to the previous estimated u_i values.
All the sources of uncertainties u_i can be statistically combined with a root sum of square to find the standard deviation σ of the final value G, Eq. 3.21:

$$\sigma = \sqrt{u_1^2 + u_2^2 + \cdots + u_n^2 + u_z^2} \tag{3.21}$$

Generally, the combined standard uncertainty σ is expanded with a coverage factor of 2 to achieve a level of confidence of 95%, assuming a normal distribution of the output value G, Eq. 3.22:

$$\Delta G = 2 \cdot \sigma \tag{3.22}$$

The method described above allows to declare: *"the final measured quantity is $G \pm \Delta G$ with a level of confidence of* 95%*, the final quantity is the mean*

of z repeated measurements".

Table 3.1 collects the contributions to the uncertainties of single parameters as well as the absolute or percentage error, calculated starting from the method described above, concerning the major measurements of the present study. The mass flow rates are measured using orifices and calibrated nozzles [107].

Effusion Cooling Performance with Uniform Mainstream Conditions

Chapter 4

Experimental apparatus and Test Matrix

Contents

In this Chapter will be illustrated the test rig and the geometric and fluid dynamic test matrix. Final aim of the present part of the work is the measurement of the adiabatic and overall effectiveness on seven multi-perforated plates in order to point out the effect of the main geometric features and flow parameters on cooling performance.

4.1 Test Rig Description

The thermal test rig, depicted in Fig. 4.1, is an open loop test rig which allows the complete control of two separate flows: the mainstream and the effusion cooling flow. The mainstream is drawn by means of two vacuum pumps from the ambient with a maximum flow rate capability of about $900 m^3/h$. Before entering into the test section the mainstream flows through an elec-

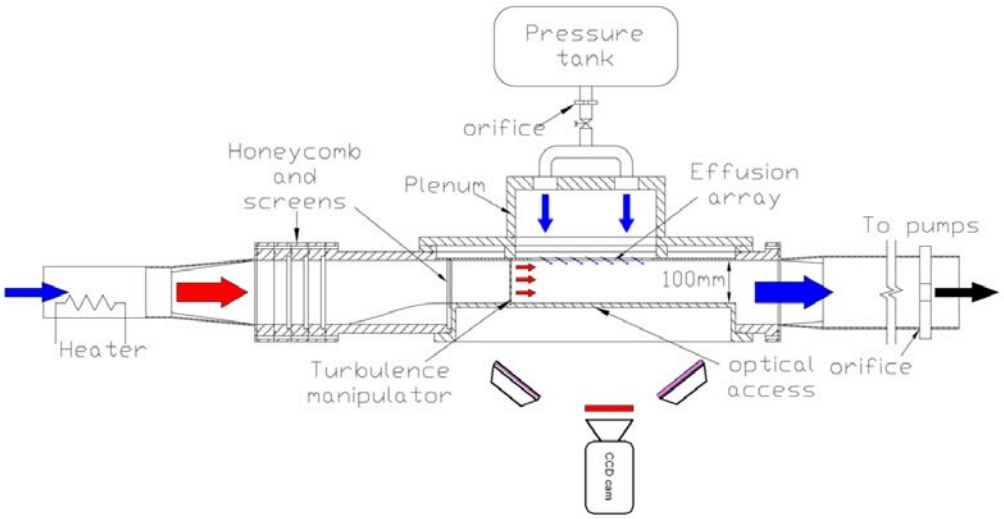

Figure 4.1: Test Rig scheme

tronically controlled electric heater composed by several finned elements with a maximum output power of $24.0kW$. Acting on a dedicated PID controller it is used to heat up the mainstream providing a constant flow temperature throughout the tests.

The effusion array is fed by a plenum chamber connected directly upstream the test plate with air or a pure foreign gas (N_2 or CO_2) stored in a pressure tank ($\approx 290K$); flow rate is set up by throttling the valves located on the cooling line.

The mass flow rate is measured in two different locations of the rig: according to the standard EN ISO 5167-1 [107] one orifice measures the flow rate blown by the pumps, while another orifice measures the effusion mass flow rates.

Two pressure scanners Scanivalve®DSA 3217 with temperature compensated piezoresistive relative pressure sensors measure the static pressure in 21 different locations with a maximum uncertainty of $\pm 51Pa$. Pressure taps are located along the mainstream channel and in the effusion plenum chamber.

Several T type thermocouples connected to a data acquisition/switch unit (HP/Agilent® 34970A) measure the mainstream and the coolant static tem-

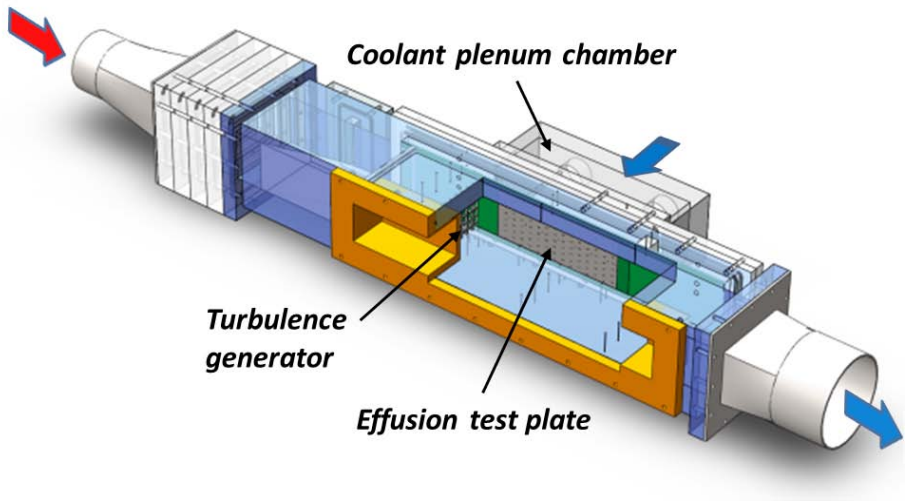

Figure 4.2: Test Model

peratures, and the test plate temperatures. Two TCs located upstream the test section are also used to control the electric heater in order to provide constant inlet temperature. Two more probes are dedicated to coolant flow and are inserted into the plenum chamber. Due to the low Mach number of the mainstream no recovery factor has been employed for the evaluation of the mainstream total temperature T_{main}.
The test rig is also equipped with optical instrumentations to perform adiabatic effectiveness measurements using PSP technique (Cfr. 3.2). Two UV High Power Led 1 Watt filtered with a blue band bass filter provide the correct light source for Pressure Sensitive Paint painted surface excitation, while a $1600x1200$ resolution 14-bit CCD camera PCO.1600 with a $610nm$ red filter records the intensity emitted by PSP.
Details on uncertainties on the measured quantities are summarized in section 3.5.

4.2 Test Model

The tested effusion geometries (described in details in section 4.3) are glued to a proper section of PMMA (Poly-Methyl Methacrylate) test model,

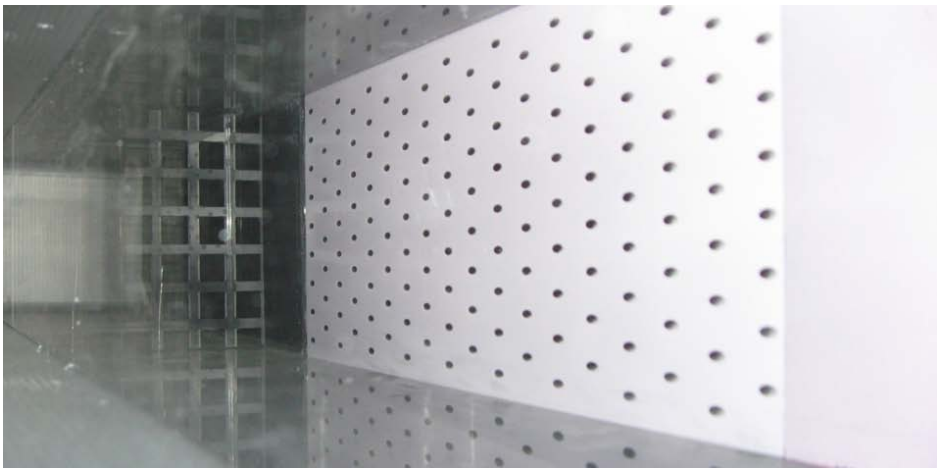

Figure 4.3: Test Section

shown in Fig. 4.2. Such a model is equipped with thermocouples and pressure probes and is able to perform adiabatic and overall effectiveness measurements setting two different flows.

The test article is completely made of transparent PMMA, thus allowing the required optical access for PSP measurements without influence the UV excitation and the emission of the paint. In addition the low thermal conductivity of the PMMA allows to limit the development of thermal boundary layer during overall effectiveness tests.

In the first part of the test model channel the mainstream flow crosses honeycombs and several screens which allow to set an uniform velocity profile before it enters into the test section. Between the first part of the channel and the test section there is a smooth converging duct and afterwards a $150mm$ long entrance region with constant cross section area $100x100mm^2$ equipped with flow straighteners.

A passive turbulence generator (square grid mesh; $4mm$ bar thickness; $16mm$ grid pitch), located $64mm$ upstream the effusion plate, is used to achieve a turbulence level of 17% at the first row of effusion array and a streamwise integral length scale of $7.5mm$. Without the turbulence grid the mainstream has a turbulence level of 1.5% at the same position and a length scale of $3.5mm$. The turbulence level is measured using a DANTEC®CTA

system with a single sensor probe DANTEC®55p04 traversed along the direction normal to the effusion plate surface. The data are sampled at $100kHz$ and the sampling period is set at 1 second; the length scale is evaluated using the frozen turbulence approximation [108].
Experimental results have showed that the mean velocity at the start of the test plate is uniform to within roughly 8% of the mean velocity, while turbulence intensity and integral length scale were uniform to within 15%. The turbulence level generated by the grid mesh are in agreement with the level predicted by the correlation of Roach [109].

The test section ($1000mm$ long) houses the interchangeable effusion test plates, they are mounted removing the plenum chamber and the gas side of the test surfaces is coated with PSP. On the plenum side, each test plate is instrumented with 8 thermocouples, as described in Section 3.3, in order to catch the plate temperature during the overall effectiveness tests.

Figure 4.3, depicting one of the selected effusion cooling geometries mounted on the test model, displays the test surface painted with PSP (light pink color) and the location of the turbulence manipulator.

4.3 Effusion Geometries

The first step of the experimental work, in order to evaluate the impact of geometric features and fluid dynamic conditions on cooling capabilities, is the definition of a test matrix. It is derived directly from previous dedicated acoustic test performed by Andreini et al. [63] to estimate the acoustic damping performances of multi-perforated liners. The main object, is to try to establish the indications for the design of effusion cooled liner taking into account acoustic and thermal requirements.

Seven geometries are considered: starting from a reference geometry (**G1**), representing a typical angled effusion cooling scheme, different geometrical parameters are varied to explore their impact on thermal effectiveness. The geometries are scaled up respect to typical engine configurations about 3 times. Perforations are manufactured by mechanical drilling on planar plates, resulting in cylindrical holes, and arranged in a staggered configura-

tion along the liner axis (Fig. 4.4).

The overall porosity is defined as, Eq. 4.1:

$$\sigma = \frac{\pi d^2}{4 S_x S_y} \tag{4.1}$$

Since it was indicated as the main geometrical parameter driving the acoustic absorption [61, 62], three different levels of perforation porosity are considered, obtained by varying hole diameter, and hole spacing.
The main part of the test matrix deals with classical 30° inclination however a single geometry (**G7**) with normal holes is considered; the perforation length and the thickness are the same for all the geometries tested (Tab. 4.1).

The thermal conductivity of the plates, made of certified steel AISI304 ($k = 15.7 W/mK$), is selected in order to perform experiments with the same levels of Biot number expected at engine condition. The representative heat transfer coefficient $\overline{HTC}$ used to estimate the Biot Number (Eq. 2.7), in both engine and test conditions, is evaluated using an area averaged of the expected heat transfer inside the cooling holes and on the gas side, Eq. 4.2:

$$\overline{HTC} = \frac{HTC_{hole} \cdot A_{hole} + HTC_{main} \cdot A_{main;top}}{A_{main;top} + A_{hole}} \tag{4.2}$$

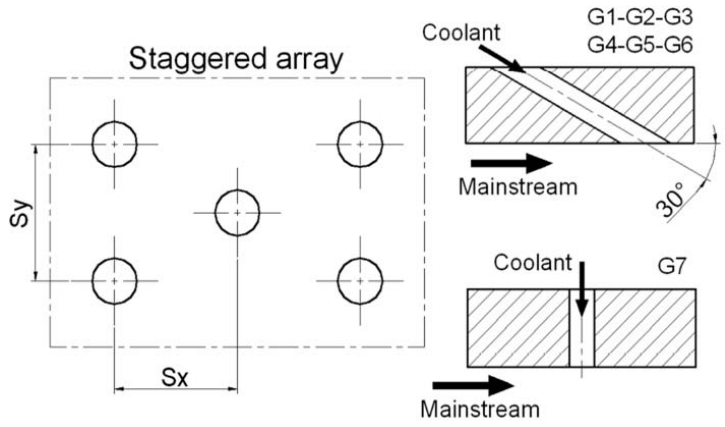

Figure 4.4: Liners effusion array

Geo.	d [mm]	σ [%]	S_x [mm]	S_y [mm]	S_x/S_y [$-$]	α [deg]	N_{rows} [$-$]
G1	1.88	1.82	13.72	11.06	1.24	30	18
G2	1.5	1.16	13.72	11.06	1.24	30	18
G3	2.34	2.84	13.72	11.06	1.24	30	18
G4	1.88	2.84	10.97	8.85	1.24	30	22
G5	1.88	1.16	17.89	13.25	1.35	30	14
G6	1.88	1.82	17.11	8.87	1.93	30	14
G7	1.5	1.16	13.72	11.06	1.24	90	18

Table 4.1: Geometric test matrix

Geometry	TCs positions $[x/S_x]$
G1-G2-G3-G7	1-2-4-6-8-9.5-14-18
G4	1-3-5-7-11-15-19-22
G5-G6	1-3-5-6-7-9-11-14

Table 4.2: TCs positions for overall tests

where $A_{main;top}$ is the portion of the surface of test plate on the gas side related to 1 hole, and A_{hole} is the internal hole surface. The heat transfer coefficients used in Eq. 4.2 are estimated by means of correlation [110], CFD calculations and using direct measurements carried out so far by the research group [111].

Each test plate on the plenum side is equipped with 8 dead holes along the centreline used to house the thermocouples for overall tests (Cfr. 3.3). The TCs location are listed in Tab. 4.2, the position $x/S_x = 0$ refers to the first row of hole.

4.4 Test Conditions

The measurements of the thermal performance consist of two sets of steady state experiments to estimate the adiabatic and the overall effectiveness distributions imposing values of effusion blowing ratio (Eq. 2.5). Main investigation parameters, BR and VR, are calculated as follows, Eq. 4.3:

$$BR = \frac{m_{eff}/\left(\pi \cdot n_{holes} \cdot d^2/4\right)}{m_{main}/A_{main}}$$
$$VR = BR \cdot \frac{\rho_{main}}{\rho_{eff}} = \frac{BR}{DR} \tag{4.3}$$

where m_{eff} is the mass flow rate through the effusion plate; A_{main} is the mainstream channel cross-section ($100x100mm^2$).

In a first test campaign, the cooling system is fed with air for overall effectiveness measurements (η_{ov}) and with pure N_2 for adiabatic effectiveness measurements (η_{ad}), while air is used for the mainstream flow; moreover for η_{ov} tests, the mainstream is heated up to $\approx 330K$. Despite these slight differences between the flows employed for the two sets of measurements, the coolant to mainstream density ratio is approximately one ($DR \approx 1$) and hence the effusion blowing ratio coincides with the velocity ratio.

In a second test campaign the effect of a density ratio on adiabatic effectiveness greater than 1 is investigated by using CO_2 as coolant gas. This allows to reach $DR = 1.5$, which is still lower with respect to expected values in actual combustors (up to 2.5) but is enough to have a perspective of its potential effect on adiabatic film effectiveness distribution. Results at higher DR are carried out for geometries **G2** and **G7** in order to explore the effect of density ratio in relationship with the different inclination angle.

The effusion plates are tested imposing six values of BR within a typical range of an aero-engine combustor ($BR = 0.5 - 5$). For measurements at $DR \approx 1.5$, to explore the effect of both blowing and velocity ratio, adiabatic effectiveness tests on geometries **G2** and **G7** are carried out imposing six BR in the range $BR = 0.5 - 5$ and five VR between $0.5 - 3$.
In addition to explore the effect of mainstream turbulence level, geometry **G2** is tested in two different mainstream turbulence configurations to point

Coolant flow				
η_{ad}; η_{ov}	DR1	G1-G7	$BR = 0.5 - 5$	$Tu = 17\%$
		G2	$BR = 0.5 - 5$	$Tu = 1.5\%$
η_{ad}	DR1.5	G2; G7	$BR = 0.5 - 5$ $VR = 0.5 - 3$	$Tu = 17\%$
Main flow				
$Re_{main} = 160000$; $Ma_{main} = 0.07$				

Table 4.3: Coolant and main flow conditions

out the influence of turbulence on thermal effectiveness. The first configuration has an intensity of 17% at the first row of holes and an integral length scale of $7.5mm$; the second configuration has a turbulence level of 1.5% at the same position and a length scale of $3.5mm$.

Mainstream absolute pressure is kept constant ($Re_{main} \approx 160000$ evaluated using the hydraulic diameter of the mainstream channel as reference length, $Ma_{main} \approx 0.07$), while coolant pressure is varied in order to ensure the desired values of coolant velocity inside the holes.
The coolant mass flow (i.e. the coolant consumption) is direct linked to the BR and to the porosity: a high porosity level demands an high mass flow rate to achieve the same blowing ratio.
To summarize, in Tab. 4.3 are listed the flow conditions of the coolant and main flow.

4.5 Impact of Adopted Scaling Criteria

Due to the limitations and the present characteristics of the test rig thermal experiments are carried out at atmospheric pressure conditions; the main scaling parameter considered is the gas blowing and velocity ratio (Cfr. 4.4). The main issue related to the choice of such scaling criteria, down to atmospheric pressure conditions, leaving aside the simple configuration of the test rig (uniform mainstream condition and no effect of radiative load), is

the reduced levels of Reynolds number inside the cooling holes and density ratio with respect to actual engine conditions. Despite typical values above 25000 in actual engines, thermal tests show holes Reynolds number lower than 10000: even if they are still in the turbulent regime, holes Reynolds number associated to experiments are well below typical engine data. On the other hand, the density ratio replicated in the experimental tests is far below the actual combustor chamber conditions.
The holes Reynolds number in the thermal effectiveness tests should have a direct impact on the overall effectiveness through the heat removed by convection inside the holes (heat sink effect) and, to a lesser extent, on the adiabatic effectiveness through the generation of turbulence at the hole outlets.

To take into account this issue on the overall effectiveness results, the Biot number similarity was considered. The similarity has been assured considering a mean area average value of heat transfer coefficients inside the cooling holes and on the gas side, both expected in test rig and in engine conditions (Eq. 4.2). The Biot similarity has allowed to select the thermal conductivity of the effusion test plates, nevertheless, if the adiabatic effectiveness distribution is replicated in the test rig, a complete similarity of overall effectiveness requires to keep similar not only the Biot number, but also the ratio between gas side and holes heat transfer coefficients.

However, the pure comparative purpose of the survey makes the obtained results unaffected by the issues reported above, especially comparing the geometries with slant holes injection. The adopted scaling criteria is hence able to highlight the relative impact of geometric and fluid dynamic parameters on the effusion effectiveness reaching the final aim of the survey, nevertheless it has limitations and the results, especially in terms of overall effectiveness, can not completely scaled to real engine conditions.

Chapter 5

Experimental Results

Contents

Adiabatic effectiveness results will be reported in terms of bidimensional distributions, lateral averaged and spatially averaged on the whole test surface; overall effectiveness data will be presented in terms of local values along the centreline next to the TCs positions and weighted average values (Eq. 3.12).

In the first part of the present section the impact of turbulence level on film cooling is reported for geometry **G2**, afterwards the work deals with a detailed analysis of all the geometries and then the effect of the main array features are summarized (inclination angle, porosity, pattern aspect ratio and hole diameter). Regarding geometries **G2** and **G7** the effect of DR on adiabatic effectiveness will be discussed. Finally, as far as overall effectiveness is concerned, a data reduction for the angled geometries (**G1**-**G6**) will be proposed.

5.1 Effect of Free Stream Turbulence on Cooling Effectiveness

Geometry G2 is tested in two different mainstream turbulence configurations to point out the influence of turbulence on thermal effectiveness. The first configuration has an intensity of 17% at the first row of holes and an integral length scale of $7.5mm$; the second configuration has a turbulence level of 1.5% at the same position and a length scale of $3.5mm$.

The effect of the free stream turbulence level can be appreciated from bidimensional adiabatic effectiveness distributions reported for three values of blowing ratio in Fig. 5.1(a). For $BR = 0.5$, i.e. in the mass addiction regime, results show that the higher turbulence level leads to an increased lateral jet spreading which is also associated with a reduced length of coolant traces in the streamwise direction. This behaviour is more relevant in the first row of holes where the turbulence level does not suffer from decay effects; Mayhew et al. [112] reported a similar behaviour for a single row configuration.

According to the classification proposed by L'Ecuyer and Soechting [113],

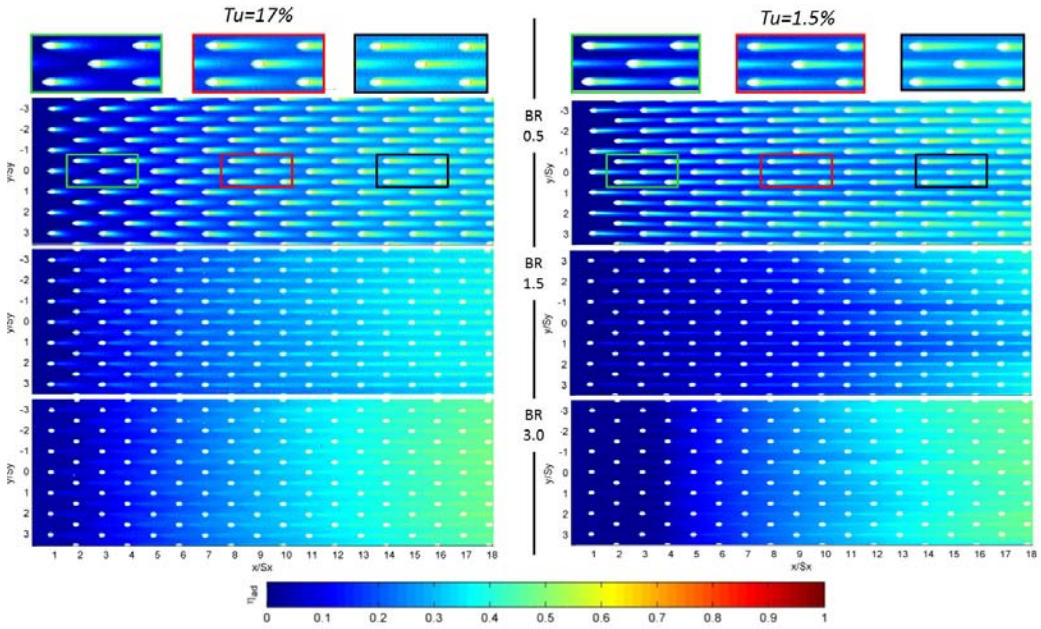

(a) Adiabatic Effectiveness

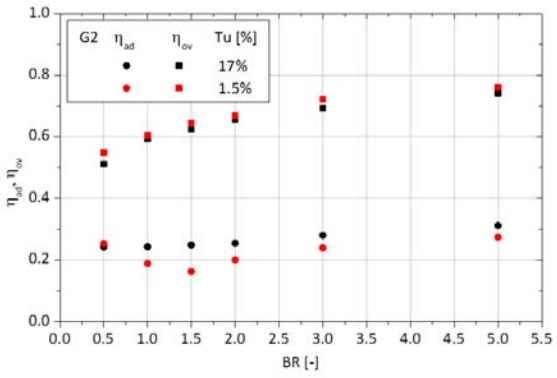

(b) Adiabatic and overall effectiveness averaged values

Figure 5.1: Effect of free stream turbulence on geometry G2 ($DR = 1$)

increasing the BR beyond $BR = VR = 0.8$, the effusion jets work in the penetration regime. It is possible to note that the turbulence transport of coolant, prompted by the high mainstream turbulence level, leads to have beneficial effect on film covering and the coolant jets seem to be more resistant to lift from the test surface. This behaviour was also documented

by Bons et al. [114] testing a single row of holes. As general results, in the penetration regime the high free stream turbulence ensures a best film protection.

For a more quantitative comparison, in Fig. 5.1(b) the effect of free stream turbulence on the spatially averaged η_{ad} is reported for different values of BR. Starting from $BR = 0.5$, where the effect of jet lateral spreading is offset by the reduction of coolant traces, the adiabatic effectiveness for the low turbulence case does not have a monotonic trend and a minimum value is registered for $BR = 1.5$; on the other hand for high Tu configuration the film protection increases with the blowing ratio. A similar trend, testing an angled effusion geometry with $BR < 1.5$ and 7 rows of holes, was recently found by Martin and Thorpe [78].
Regarding the overall results depicted as averaged value in Fig. 5.1(b) the effect of turbulence is negligible: the expected enhancement of HTC on the gas side, that generally deteriorates the overall effectiveness, is balanced by the increase of film covering leading to a not appreciable impact of this parameters on overall results.

5.2 Detailed results

All the achievements obtained from the experimental survey will be reported in details in the following sections, sorted into the seven geometries. More details will be given for array **G1** considered the reference case involving an intermediate hole diameter and axial/circumferential hole spacings. Results will be given for the high turbulence case and at $DR = 1$.

Array G1

In Fig. 5.2(a) the bidimensional adiabatic effectiveness distributions are shown for all the blowing ratios tested. Analysis of the film cooling performance can be conducted using lateral averaged adiabatic effectiveness distributions as a function of the axial distance normalized with axial pitch, which corresponds to the number of rows, varying the test condition. As shown by Fig. 5.2(b), the higher film wall protection is achieved at low blowing ratio for $x/S_x < 6$, whereas opposite behaviour is reported for $x/S_x > 6$. This behaviour can be attributed to the lift-off of the coolant jets, which does not guarantee a correct wall protection at the first rows of holes, while after the sixth row and for higher blowing ratio values, the large amount of coolant mass flow injected and the superposition effect lead to an higher adiabatic effectiveness despite the lift of each jets. Although an asymptotic condition could not be verified at any of the tested blowing ratios even for $x/S_x = 18$, the trend of growth results to be proportional to BR. The poor film protection in the first rows of holes emphasizes the necessity of a starter film, especially in presence of a radiative load.

Concerning the overall effectiveness values, as shown in Fig. 5.2(c), the increase of blowing ratio has beneficial effects. High coolant mass flow permits to lower the wall temperature thanks to the heat removed by the passage of the coolant through the holes ("heat sink effect"); in addition it leads to a best film protection as showed by the adiabatic effectiveness results.

It is worth to notice that the tested geometries have an appreciable number of rows of holes; this means that the film protection, due to the superposition effect of the film cooling and hence to the high values of adiabatic

effectiveness, has a significant impact on the overall thermal effectiveness (η_{ov}). In effusion geometries with limited number of rows of holes the liner protection is mainly driven by the "heat sink effect".

Array G2

In the same way as reported for geometry **G1**, Fig. 5.3 shows the results in terms of adiabatic and overall effectiveness against the blowing ratio. Compared with **G1**, this geometry has a small hole diameter but the same axial e tangential spacing.

Enter into details, the blowing ratio allows to increase both adiabatic and overall effectiveness for all x/S_x values. Furthermore $BR = 0.5$ and $BR = 1$ have similar adiabatic effectiveness values as reported for **G1**: the effect of penetration is offset by the increase cooling mass flow.

Array G3

As shown by the test matrix (Tab. 4.1), geometry **G3** has an high porosity effusion array (2.34%) and the same axial e tangential spacing of the geometries showed before.
First of all let's focus on the adiabatic effectiveness got by means of PSP technique. As shown in Fig. 5.4(a); 5.4(b) up to 0.7 values, having the slope displayed in the graph, have been obtained at the end of the plate for the higher blowing ratio.
Concerning blowing ratio effects on cooling efficiency, remarks quite similar to the ones of **G1** may be drawn for the present configuration too: as a matter of fact the increasing BR always (i.e. for its highest value as well) makes the effectiveness to increase moving downstream, nevertheless for the first rows of holes ($x/S_x < 4$) better film covering is achieved lowering the cooling mass flow.
Fig. 5.4(c) shows the overall effectiveness trend. Once again these values increase as the blowing ratio becomes higher in all position along the centreline.

Array G4

Compared with geometry **G3**, this test plate has the same porosity value (2.34%) but a smaller holes diameter; as a consequence the total number of rows of holes is 22, 4 rows plus the previous configuration.
As reported in Fig. 5.5(a); 5.5(b), array **G4** provides a high wall protection reaching adiabatic effectiveness values close to 0.8 for $BR = 5$.
As far as superposition length is concerned, an asymptotic behaviour is no evident despite the large number of rows: only a reduced effectiveness growth rate as we move downstream the cooled region is to be pointed out.
On the other hand, overall effectiveness (Fig. 5.5(c)) seems to reach an asymptotic value after the 18^{th} rows: once again the blowing rate has a positive effect on overall effectiveness, increasing both the film covering and the heat sink capability; values close to 0.95 are registered for $BR = 5$ case.

Array G5

The present section deal with configuration marked by the same porosity of geometry **G2** but largest hole diameter: keeping constant the perforation length and the hole pattern, the plate is characterised by a reduced number of rows of holes.
This feature reduces the benefit coming from the superposition of film covering; moving downstream the growth rate of effectiveness is low and a moderates values of adiabatic effectiveness are reached at the end of the plate (Fig. 5.6(a); 5.6(b)). Moreover, the trend is well away from the attainment of an asymptotic behaviour.
The overall effectiveness (Fig. 5.6(c)) reflects the behaviour described for the adiabatic results, with moderate and not asymptotic values registered downstream.
With respect to blowing ratio effects, once again thermal efficiency increases as BR is increased. However until the fourth row of holes, the best film wall protection is achieved lowering the velocity ratio; the same behaviour was described for geometry **G1**.

Array G6

To explore the effect of the hole spacing, the present test plate has the same porosity and hole diameter of array **G1** but different axial e tangential spacing.
The adiabatic effectiveness results (Fig. 5.7(a); 5.7(b)) show a curve intersection, varying the blowing ratio, located at $x/S_x = 4$; two rows upstream with respect to the geometry **G1**. For the first rows of holes, the best film protection is achieved at lower blowing rate where the cooling jets work in mixing regime and the coolant traces are well highlighted at hole exit. Nevertheless, the film superposition lead to a greater growth rate of effectiveness increasing the BR and at the end of the plate the best protection is obtained with the higher coolant consumption condition ($BR = 5$), without reaching an asymptotic value.
Regarding the overall results (Fig. 5.7(c)), moving downstream the effectiveness grows row by row with the higher values reached on all the test plate at $BR = 5$. At this condition the TC located at $x/s_x = 14$ registers a value close to 0.9.

Array G7

The main array features of test sample **G7** is the normal holes; moreover it has the same porosity and hole diameter of geometry **G2**. As shown by the bidimensional adiabatic effectiveness distributions (Fig. 5.8(a)) the coolant jets is more prone to lift off from the test surface compared with the tilted holes, and consequently the coolant traces seem less prominent. The spanwise average effectiveness, reported in Figure 5.8(b), is evaluated considering a $1S_y$ width region along the centreline in order to not include in the average values the rig wall effect due to the interaction between mainstream and the highly penetrating jets . This effect leads to a coolant concentration along the centreline when the cooling mass flow is increased (see $BR = 5$ case) and on the lateral sides are clearly visible coolant traces drawn to centreline. Increasing the coolant mass flow over $BR = 0.5$, it is not possible to recognize, in the spanwise averaged trend, peaks of effectiveness downstream

each row of holes: the jets work in full penetration regime providing a spread protection of the plate surface with high mixing rate with coolant and main flow.
Compared with the behaviour of the other geometries, $BR = 3$ and $BR = 5$ test cases have similar adiabatic effectiveness values, however overall effectiveness increase as the blowing ratio ratio number is changed from 3 to 5 (Fig. 5.8(c)). For the present test plate an asymptotic value of overall effectiveness seems to be reached for $x/S_x > 14$.

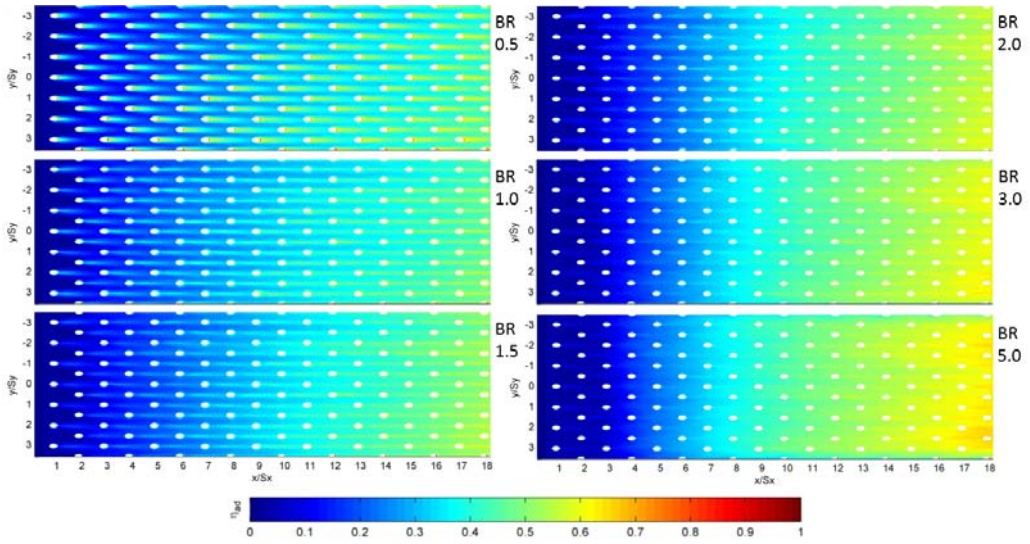

(a) Adiabatic Effectiveness distributions

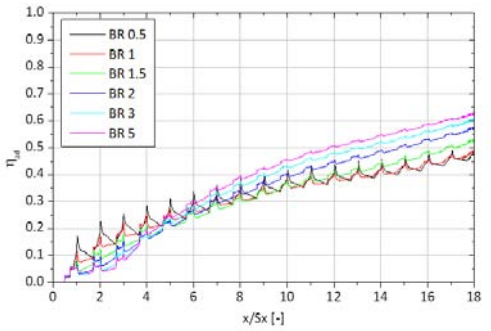

(b) Lateral averaged adiabatic effectiveness

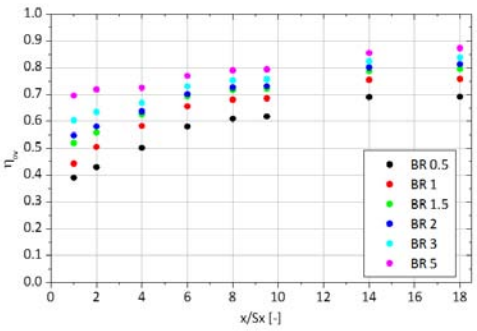

(c) Overall effectiveness distribution

Figure 5.2: Cooling effectiveness array **G1**

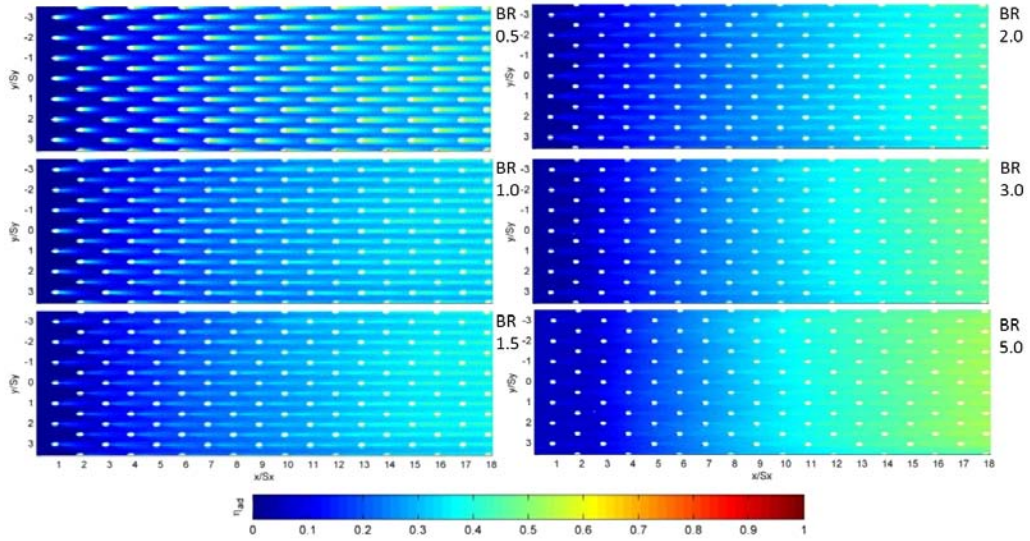

(a) Adiabatic Effectiveness distributions

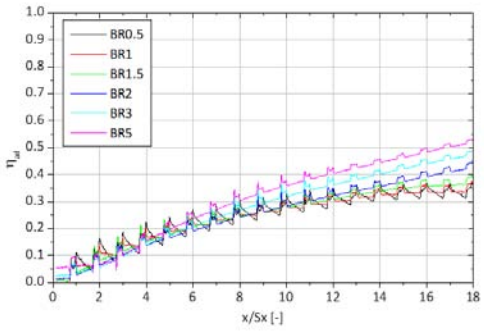

(b) Lateral averaged adiabatic effectiveness

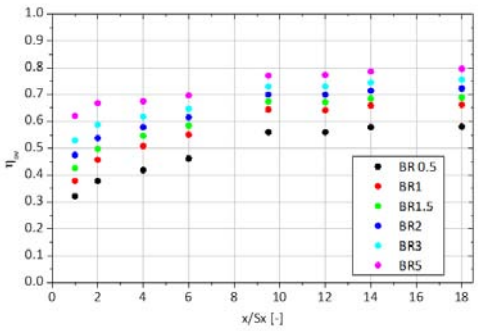

(c) Overall effectiveness distribution

Figure 5.3: Cooling effectiveness array **G2**

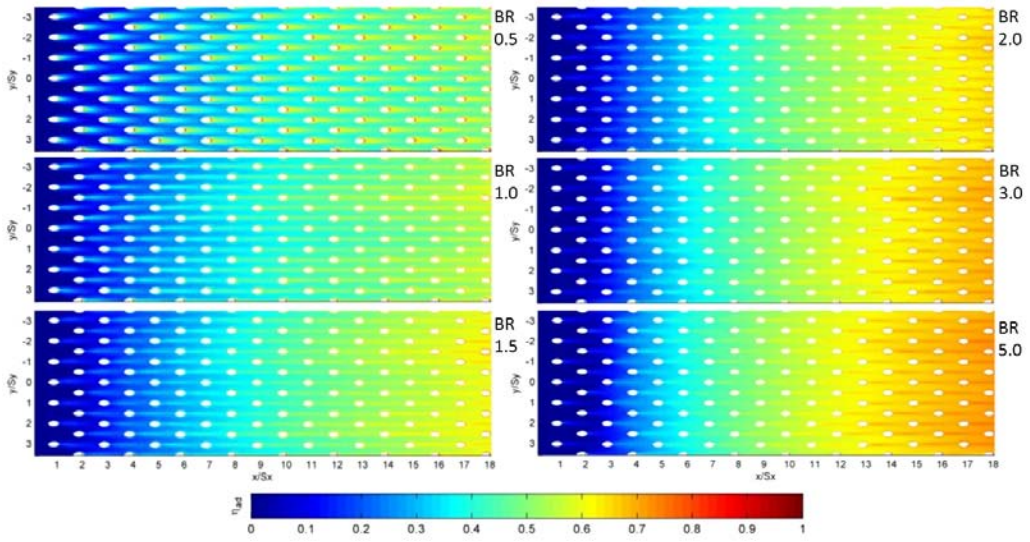

(a) Adiabatic Effectiveness distributions

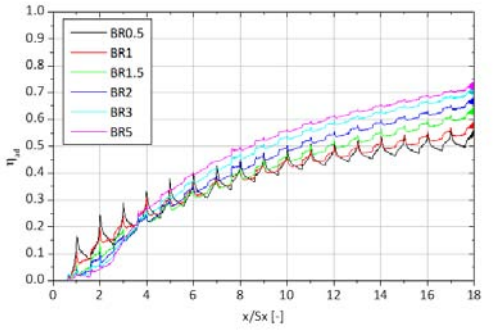

(b) Lateral averaged adiabatic effectiveness

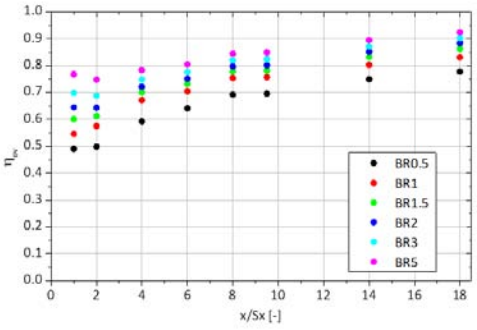

(c) Overall effectiveness distribution

Figure 5.4: Cooling effectiveness array **G3**

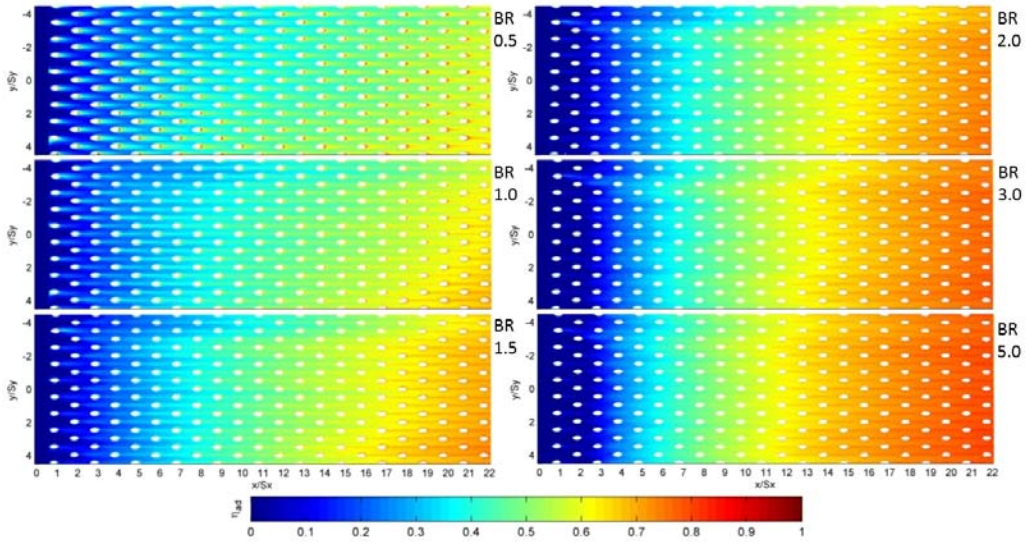

(a) Adiabatic Effectiveness distributions

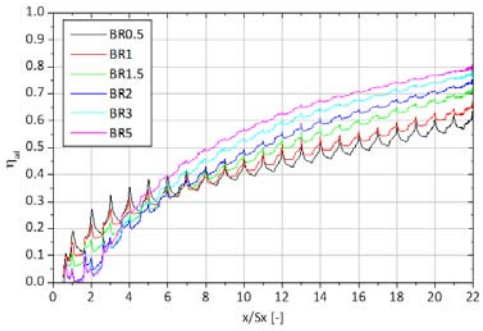

(b) Lateral averaged adiabatic effectiveness

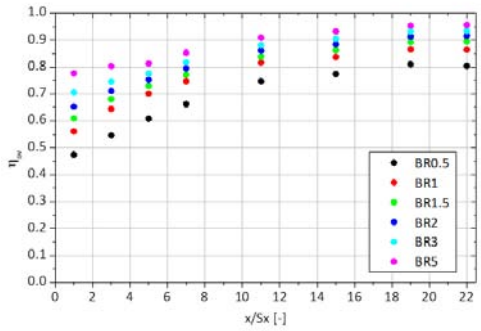

(c) Overall effectiveness distribution

Figure 5.5: Cooling effectiveness array **G4**

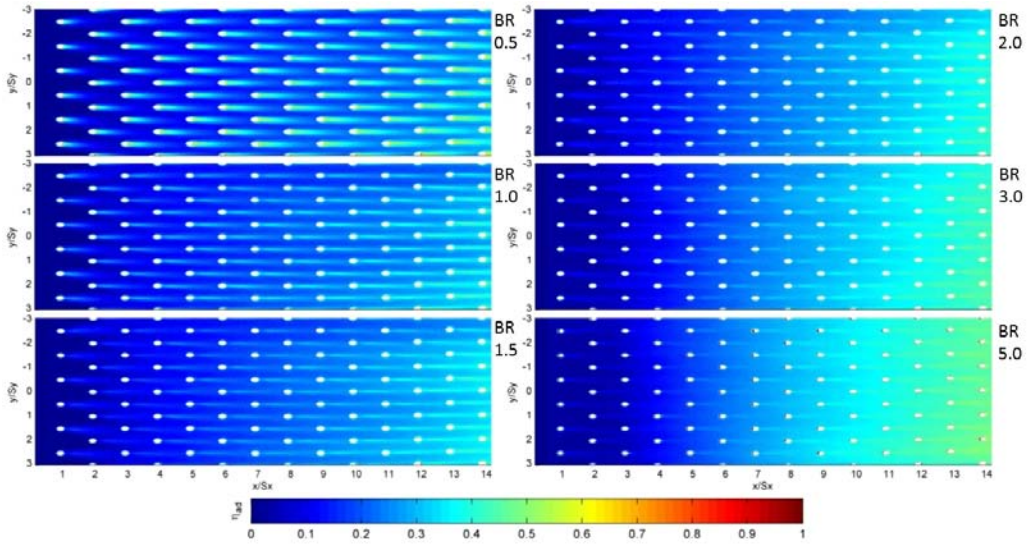

(a) Adiabatic Effectiveness distributions

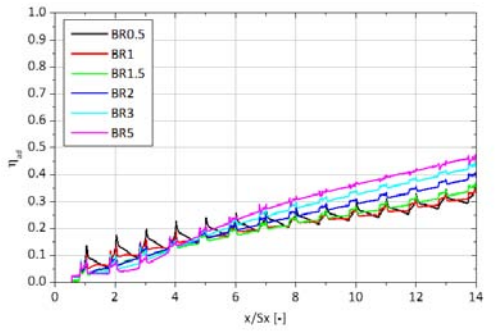

(b) Lateral averaged adiabatic effectiveness

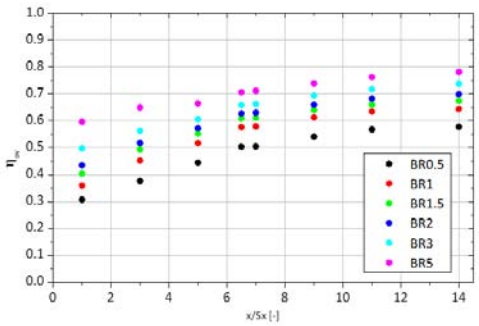

(c) Overall effectiveness distribution

Figure 5.6: Cooling effectiveness array **G5**

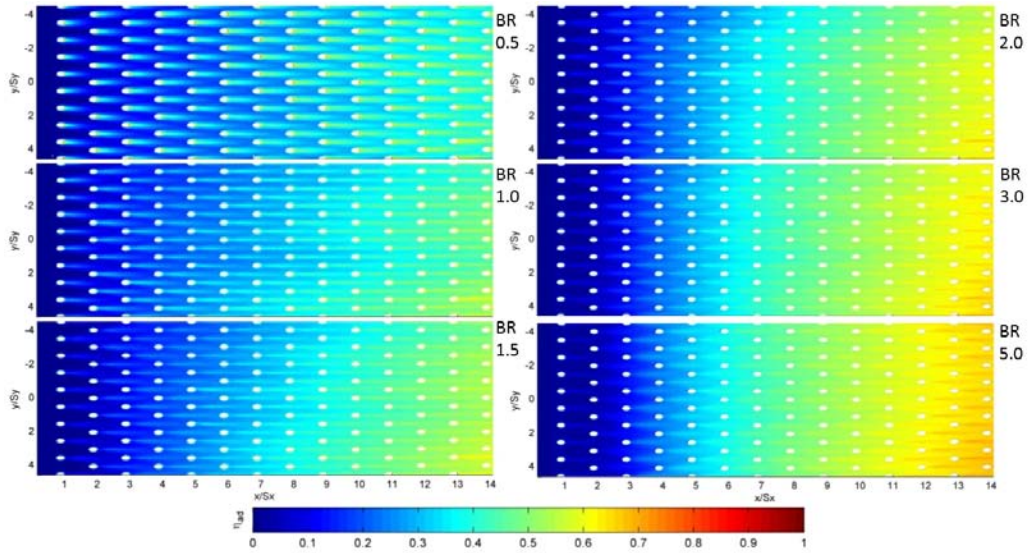

(a) Adiabatic Effectiveness distributions

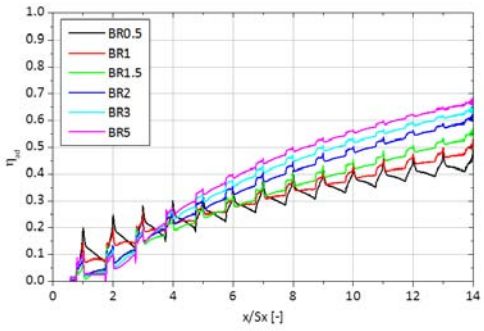

(b) Lateral averaged adiabatic effectiveness

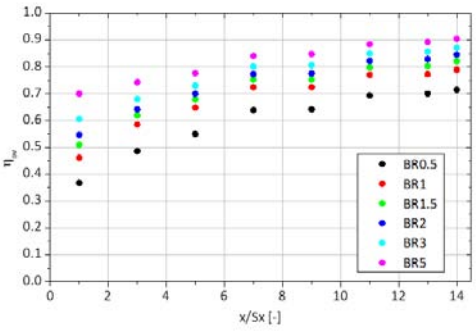

(c) Overall effectiveness distribution

Figure 5.7: Cooling effectiveness array **G6**

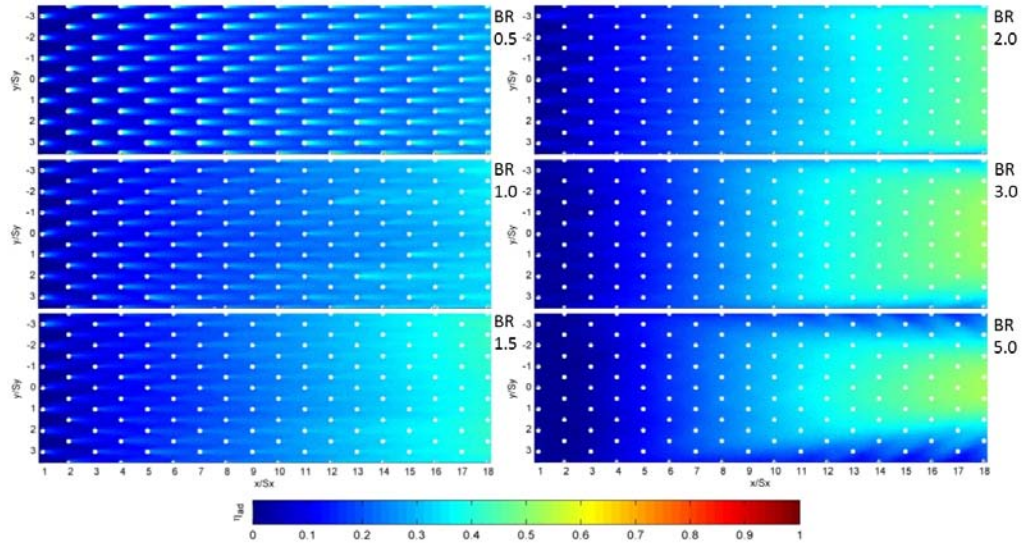

(a) Adiabatic Effectiveness distributions

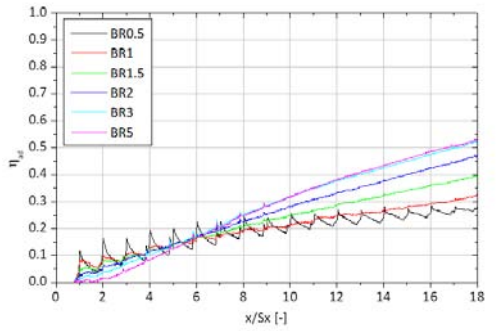

(b) Lateral averaged adiabatic effectiveness

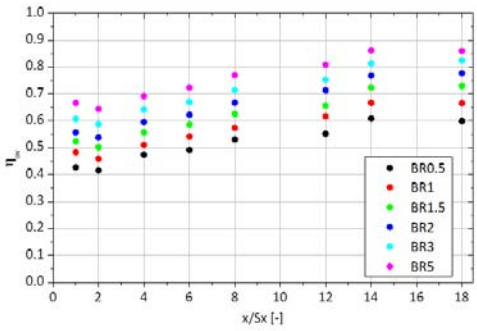

(c) Overall effectiveness distribution

Figure 5.8: Cooling effectiveness array **G7**

5.3 Impact of Main Geometric Features on Cooling Effectiveness

5.3.1 Influence of Porosity

The experimental results in terms of adiabatic and overall mean values for all the geometries with slant-hole injection and for $Tu = 17\%$ configuration are reported in Fig. 5.9 for the three levels of porosity (σ) investigated. In the considered test matrix (Tab. 4.1) there are two possible ways to obtain the variation of the overall porosity: varying hole diameter or axial/circumferential spacing. Two set of liner geometries can be identified: **G2**, **G1** and **G3** have the same holes pattern with an increasing hole diameter from 1.5 to 2.34mm; geometries **G4**, **G1** and **G5** have the same hole diameter with increasing hole spacings. For the two groups of geometries three correspondent levels of porosity (1.16%, 1.82% and 2.84%) are reproduced.
The porosity is considered a relevant design parameter for effusion cooling system due to its role in acoustic absorption capability [63], the half way value in the considered range of porosity could be considered the representative case of actual liner design.

In order to take into account the obvious effect of an increasing coolant mass flow with increasing levels of porosity, both spatially averaged effectiveness values are reported as a function of the product between BR and porosity (σ), which is a direct measure of coolant consumption, Eq. 5.1:

$$BR \cdot \sigma \propto \frac{\dot{m}_{cool}}{\dot{m}_{main}} \tag{5.1}$$

Comparing results of Fig. 5.9(a), it can be observed that, at the same coolant consumption, the geometry with higher porosity (**G3** and **G4**) show the best performance in terms of both adiabatic and overall effectiveness, moreover a positive effects on cooling performance seems to be achieved reducing diameter and hole spacings (**G4**).

These results suggest that, keeping constant the coolant consumption (i.e. the parameter $BR{\cdot}\sigma$), an improvement in overall effectiveness can be achieved working with level of porosity higher than the usual values required for cooling. In fact, the two strategy of porosity variation have both a positive impact on the heat sink effect at the same coolant mass flow and, as reported in the experimental data, it also improves the adiabatic effectiveness.

In order to better assess the effect of the specific geometric feature in the definition of the relationship between effectiveness and plate porosity, results are reported as a direct function of BR in Fig. 5.9(b), where it can be clearly observed the increasing of both adiabatic and overall effectiveness with porosity. The slight increase of adiabatic effectiveness observed for geometries **G4** and **G2** with respect to their correspondent case at the same level of porosity, **G3** and **G5** respectively, is due to the different number of rows for the cases at same level of porosity, which has a direct impact on the results of spatial averaging.

To better explain the behaviour described above, Fig. 5.10 reports the distribution of laterally averaged adiabatic effectiveness for geometries **G3** and **G4** at different BR as a function of the axial distance normalized with axial pitch. It can be observed that, as expected, the evolution of adiabatic effectiveness is practically coincident between the two geometries at same levels of BR: the contribution of the additional four rows (from 18 to 22 as highlighted in Fig. 5.10) of geometry **G4** leads to the higher values of spatially averaged effectiveness observed in Fig. 5.9(b). The same behaviour can be addressed to the comparison between geometries **G2** and **G5**.

Being the test conducted under the same main flow conditions, the trends of Fig. 5.10 confirm that the adiabatic effectiveness is less influenced by the Reynolds number of the hole. Due to the larger hole diameter geometry **G4** exhibit, at the same BR condition, a hole Reynolds number 30% greater with respect to **G3**, despite this difference the impact on adiabatic effectiveness trends is negligible.

5.3.2 Influence of Hole Diameter

The comparison between geometries **G3** and **G4** permits to point out the direct effect of the hole diameter with the same level of perforation porosity ($\sigma = 2.84\%$) and pattern aspect ratio. According to the constant plate

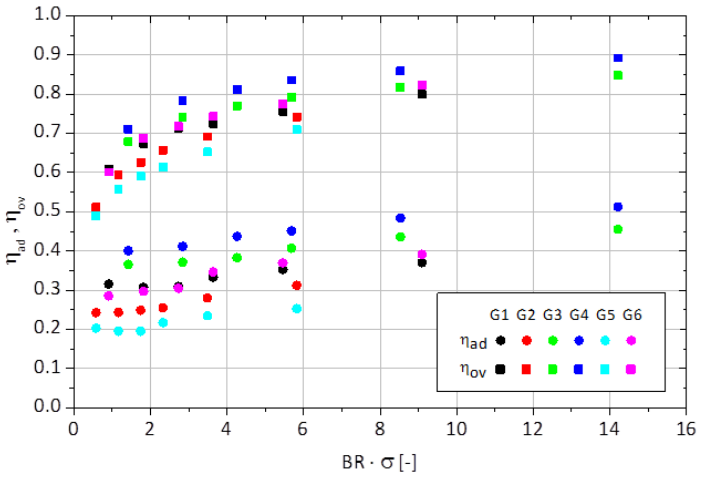

(a) Cooling performance as function of coolant consumption

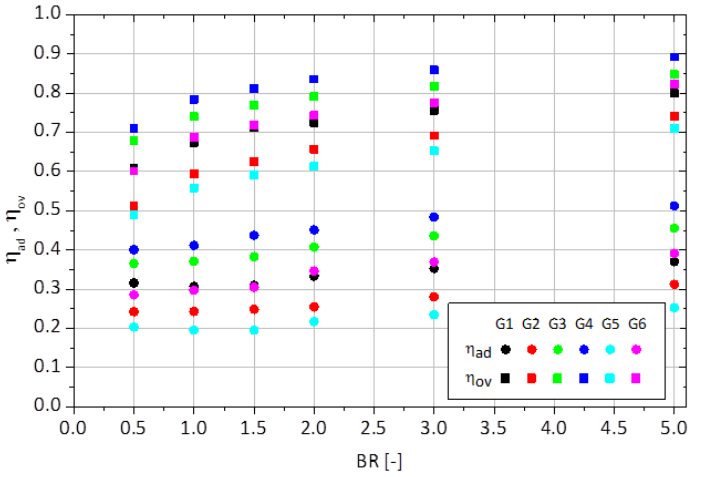

(b) Cooling performance as function BR

Figure 5.9: Spatially averaged adiabatic and overall effectiveness for test plates with 30° hole inclination ($Tu = 17\%$)

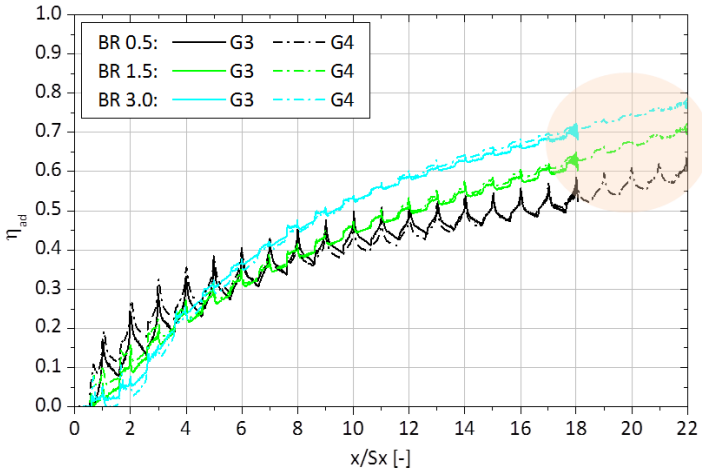

Figure 5.10: Distribution of laterally averaged adiabatic effectiveness for geometries **G3** and **G4** at different BR as a function of number of rows ($Tu = 17\%$)

thickness for the entire test matrix, the main consequence of the different diameter ($d = 2.34mm$ for **G3** and $d = 1.88mm$ for **G4**) is a variation in the length to diameter ratio of the holes ($l/d = 4$ and $l/d = 5$ respectively). The principal effect of the different hole diameter is the heat sink effect capability of the two geometries. The heat removed through forced convection inside holes can be estimated using basic relation of heat transfer, Eq. 5.2:

$$\dot{Q}_{heatsink} = HTC_{hole} A_{hole} \Delta T = HTC_{hole} (\pi \cdot d_{hole} \cdot l_{hole} \cdot n_{hole}) \cdot \Delta T \quad (5.2)$$

where n_{hole}, d_{hole}, n_{hole} are respectively the total number of holes, the diameter and the length of the perforation; while HTC_{hole} is the convective heat transfer inside the hole array. The heat transfer coefficient can be estimated with the Coulburn correlation [115] corrected for the entrance effect due to the low value of l_{hole}/d_{hole}, Eq. 5.3:

$$HTC_{hole} = 0.023 Re_{hole}^{0.8} Pr^{0.33} \cdot \left(1 + \left(\frac{d_{hole}}{l_{hole}}\right)^{0.7}\right) \frac{k_{cool}}{d_{hole}} \quad (5.3)$$

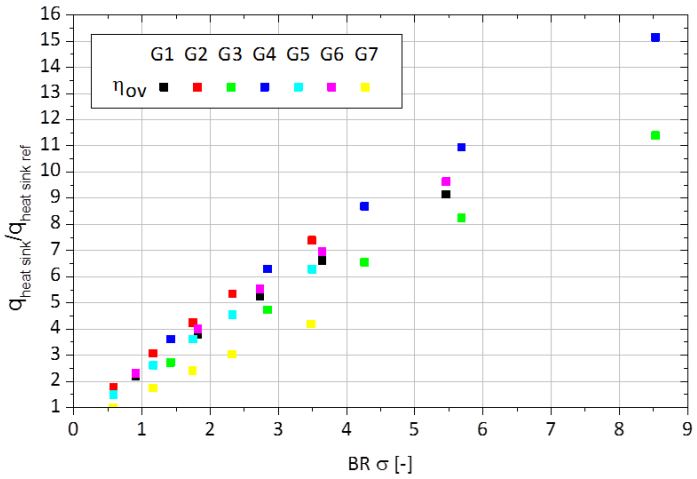

Figure 5.11: Heat sink effect capability

Substituting in Eq. 5.3 the proper geometric dimensions and fluid dynamic parameters recorded during tests for all the geometries, it is possible to estimate the heat sink capability in terms of heat removed inside perforation per unit of temperature difference ΔT. The results normalized with respect to the condition $BR = 0.5$ for geometry **G7** are illustrated in Fig. 5.11 as function of the coolant consumption parameter $BR \cdot \sigma$. The array **G3** and **G4** exhibit the same averaged value of heat transfer coefficient (Eq. 5.3); nevertheless a significant gain in the heat removed by forced convection ($\approx +30\%$) for **G4** is obtained at the same coolant consumption thanks to the term A_{hole}. In addition, despite the same level of laterally averaged adiabatic effectiveness is observed along the plate (Fig. 5.10), the additional 4 rows of holes in the perforation length for the array **G4** leads to an improvement on the spatially averaged adiabatic effectiveness in all tested conditions as reported in Fig. 5.9.

Consequently, a slight improvement on the mean value of overall effectiveness is reported for geometry **G4** driven by the increase of the heat sink effect and by the better average film protection.

More in details, looking at the distribution of η_{ov} along the centreline (Fig. 5.12), up to $x/S_x = 18$ the two arrays show comparable values of overall effective-

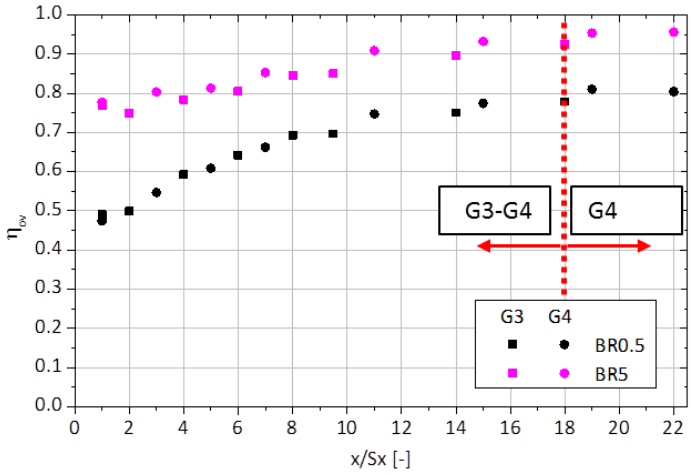

Figure 5.12: Distribution of local values of overall effectiveness for geometries **G3** and **G4** at different BR as a function of number of rows ($Tu = 17\%$)

ness distribution. Once again, the real benefits of the use of small hole diameters come from the possibility to use more rows of holes in the same perforation length.

5.3.3 Influence of Pattern Aspect Ratio

The data, reported in Fig. 5.9, allow to underline the effect of the pattern aspect ratio in hole spacing, defined as S_x/S_y, considering geometries **G1** and **G6**. They present the same overall porosity, hole diameter and inclination but, respectively $S_x/S_y = 1.24$ and $S_x/S_y = 1.93$. In the range of investigated blowing ratio number the two level of pattern aspect ratio seem to have not appreciable impact on overall effectiveness, the effect on the η_{ov} results is roughly 2% at $BR = 5$. This behaviour can be explained by the adiabatic film results: for geometry **G1** the effect of an high spanwise pitch is offset by the reduction of the streamwise pitch with a slight improvement of film covering at the end of the plate as can be appreciated comparing the 2D distributions of Fig. 5.2 and Fig. 5.7. This result is promoted by the high free stream turbulence level of the mainflow that leads to an high lateral

spreading of the coolant jets. In addition it is worth to notice that the two geometries have the same capabilities in terms of heat removed by forced convection through the holes (i.e. the same hole diameter and length).

5.3.4 Influence of Hole Inclination Angle

To discuss the influence of hole inclination angle, two different geometries (**G2** and **G7**) are considered: the first one has a tilted array with an inclination of 30°, while the second one has a 90° holes array. The comparison is reported for the high free stream turbulence configuration ($DR = 1$).
Focussing on the spatially averaged values displayed in Fig. 5.13, at low blowing ratio geometry **G2** shows a better wall protection than geometry **G7**, likely because the tilted holes help the jets to remain attached to the test plate assuring a best film covering. Raising the blowing ratio, the impact of the hole inclination angle seems to be relatively weak.

To better understand this behaviour, let's focus on distributions at $BR = 0.5$ and 3 reported in Fig. 5.3(a) and Fig. 5.8(a). For $BR = 0.5$ case the geometry **G7** shows coolant traces that decays rapidly in the streamwise direction leading to a poor wall protection and the jets are already in penetration regime. Increasing the BR level, despite the high jet penetration due its momentum in the direction normal to the plate, the geometry **G7** reports a similar distribution of film effectiveness with respect to geometry **G2**. The jets detach from the wall and the cooling effectiveness reduces, as can be seen in the first part of the effusion plate. However, due to the higher coolant mass flow injected, the superposition effect is larger and the plate effectiveness is enhanced downstream.

Concerning the overall effectiveness, for low BR levels, **G2** and **G7** have the same thermal efficiency; raising the coolant mass flow ($BR = 3$ and 5) the geometry with perpendicular array shows a best thermal effectiveness (+5% respect to geometry **G2**) in spite of the area for the "heat sink effect" is reduced. This behaviour is ascribable to the low mainstream heat transfer coefficient augmentation and to the higher heat transfer coefficient inside hole due to the entrance effects, with respect to the configurations with slant-hole injection. Looking at the Fig. 5.11, the array **G7** has a reduced heat sink

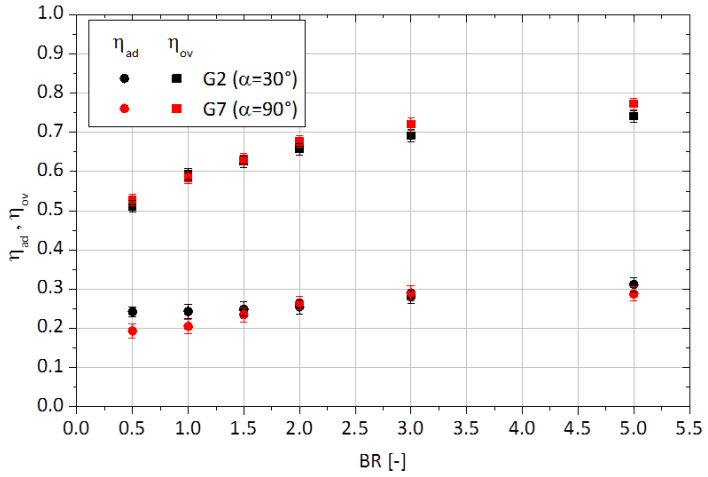

Figure 5.13: Spatially averaged overall and adiabatic effectiveness: comparison between geometries **G2** and **G7** ($Tu = 17\%$)

capability of about $\approx 40\%$ with respect to **G2** even if the geometry with tilted holes provide a twice area for heat sink effect.
For the sake of clarity this aspect will be deal in the next sections by means of a numerical procedure to extend the validity of the survey.

To perform a proper comparison of inclined and perpendicular holes, it is necessary to take into account the actual operating conditions of the engines: η_{ov} values shown here are then strictly valid for tested conditions and there are at least two basic points that can affect the comparison.

First of all the mainstream in the experimental apparatus does not have a 3D flow field. The high jet penetration, typical of 90° hole angle, in real engine operating condition could interact with the tridimensional flow field of combustion chamber influencing the combustion process and reducing the coolant wall protection. In this type of experiment with a simple configuration of the test rig, the jet-mainstream mixing is recorded as near wall coolant, especially in the final rows. The second issue is the absence of heat transfer by thermal radiation in the experiments. As it will be shown in the following sections, the normal arrays with high radiative heat load may have a worse behaviour from a thermal point of view.

5.4 Influence of Density Ratio on Adiabatic Effectiveness

As observed in the previous sections, angled geometries of the test matrix (**G1**-**G6**) exhibit a common behaviour with respect to BR, while more

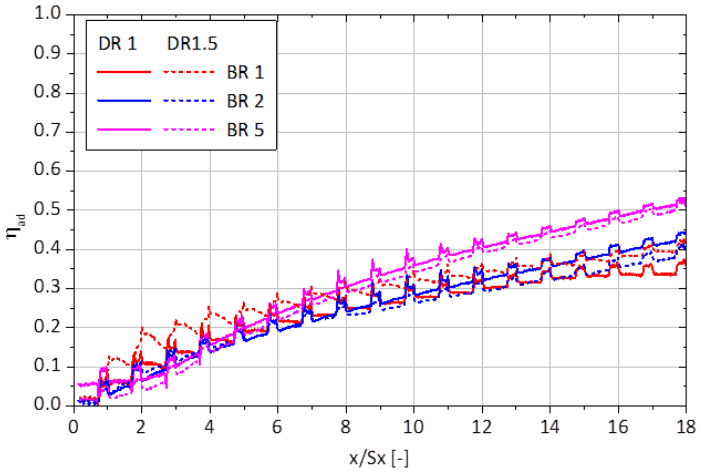

(a) Array **G2**

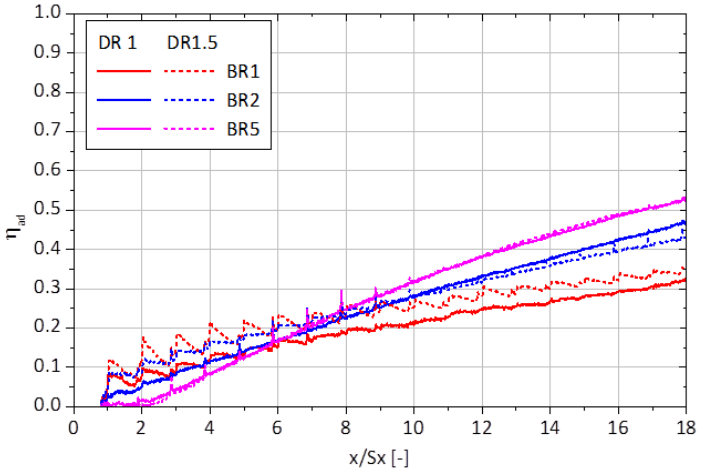

(b) Array **G7**

Figure 5.14: Effect of density ratio on adiabatic effectiveness ($Tu = 17\%$)

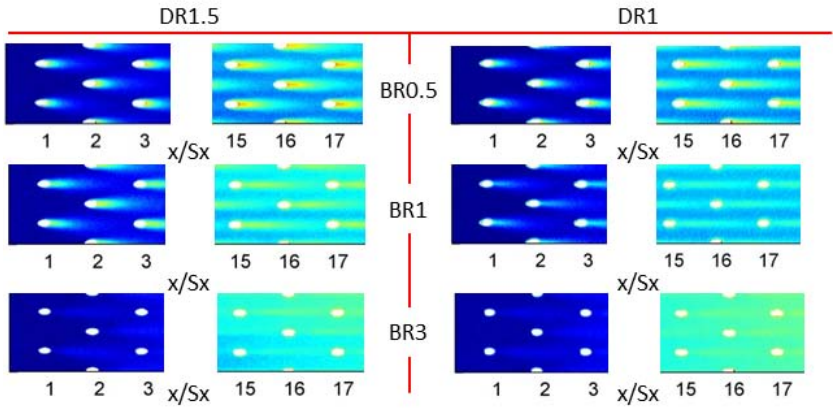

Figure 5.15: Effect of Density Ratio on coolant traces for array **G2** ($Tu = 17\%$)

significant differences can be appreciated when comparing **G2** and **G7** due to the different inclination angle. To investigate the effect of density ratio it is therefore considered only these last two cases, being geometry **G2** fully representative of the behaviour of all remaining angled geometries.

Let's first look at the effect of DR on geometry **G2**, Fig. 5.14(a) shows that it has a relevant impact at $BR = 1$ condition near the transition between mixing and penetration regime and a progressive reduced role for higher BR. Enter into the details, it is clear from the 1D trend the different decay shape of effectiveness between each row of holes especially at $BR = 1$. This behaviour can be attributed to the lower effective velocity ratio at $DR = 1.5$ that, according to the classification introduced by L'Ecuyer and Soechting [113], keeps the jets in the mixing regime whereas $DR = 1$ case at the same BR have moved to penetration ones. This behaviour can be clearly appreciated by looking at shape of coolant traces reported in Fig. 5.15, where some zoomed views of adiabatic effectiveness are depicted for lower BR cases. In addition at lower blowing rate $BR = 0.5$ the density ratio helps the jets to remain attached to the surface enhancing the lateral spreading.

The same discussion can be carried out for geometry **G7** where the described effects are even more pronounced, with an appreciable impact of DR up to $BR = 2$ especially in the first part of the plate (Fig. 5.14(b)).

5.5 Post Processing Procedure trough correlative analysis

In order to carry out a more accurate comparison between geometries **G2** and **G7**, and therefore to better assess the effect of the hole inclination angle, an additional post-processing of measurements is performed by employing a correlative numerical methodology. In particular two different investigations are considered. In the first one it is obtained the augmentation of the gas side heat transfer coefficient due the presence of effusion jets, while in the second one it is analysed the impact on the two effusion arrays of a radiative heat load.

These analysis are carried out using the in house developed numerical procedure Therm-1D. It is a one-dimensional thermal flow network solver coupled with heat conduction solution across the combustor liner. On the coolant side, the procedure solves the coolant fluid network of the system, with a wide library of heat transfer correlations for the most common cooling techniques; on the hot gas side it estimates the convective and radiative heat loads through specific correlations for heat transfer coefficient and gas emissivity, mainly following the one dimensional approach suggested by Lefebvre [6]. The final temperature distribution is obtained considering also the film cooling and the "heat sink effect" due to the presence of cooling holes. Further details on the procedure can be found in Andreini et al. [116, 117].

5.5.1 Gas Side Heat Transfer Augmentation

To retrieve the resulting heat transfer coefficient on the gas side for geometries **G2** and **G7** during overall effectiveness tests, specific models of the two configurations have been prepared with Therm-1D. Calculations are carried out by fixing the measured adiabatic effectiveness on gas side of the plates while heat transfer on the cold side and inside each effusion hole were computed referring to specific correlations:

- Concerning the heat transfer coefficient on the suction side of the effu-

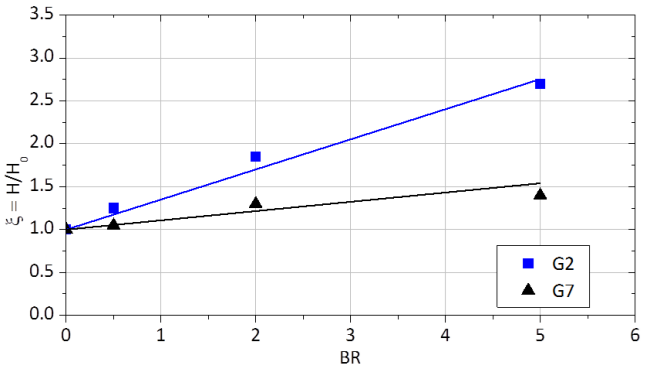

Figure 5.16: Heat transfer augmentation for geometries **G2** and **G7** ($Tu = 17\%$)

sion plate, the correlation proposed by Dorignac et al. [118] is considered. This expression delivers the heat transfer coefficient determined by the flow acceleration around the holes of a staggered array fed by a plenum, which is the same configuration of the modelled test rig.

- The heat transfer inside each effusion holes is modelled referring to the correlation of Cho and Goldstein [110], which is valid for short holes in a wide range of Reynolds number.

For three levels of blowing ratio ($BR = 0.5; 2; 5$) considered during overall effectiveness tests ($Tu = 17\%$), a simulation is performed computing the metal temperature along the plate. Starting from a gas side heat transfer coefficient computed through a standard smooth channel correlation (H_0), a uniform augmentation coefficient $\xi = H/H_0$ is applied along the plate so as to match the measured metal temperature. As discussed in section 2.2.2, due to the injection of coolant, an enhancement of heat transfer is expected in blowing conditions.

The resulting variation of ξ with effusion BR for the two geometries is the desired output. Fig. 5.16 reports the obtained augmentation coefficients for the two geometries: data point for $BR = 0$ correspond to theoretical flat plate results.

The post-processed data for all the angled geometries show a similar level of heat transfer augmentation. As expected, an increase in the heat transfer

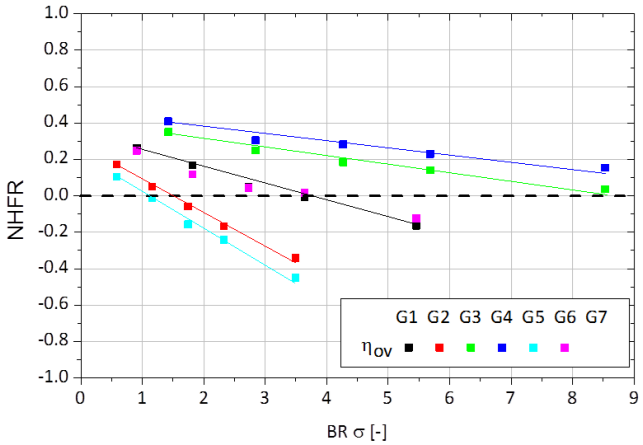

Figure 5.17: Net heat flux reduction

augmentation when increasing the blowing ratio is reported, while the normal hole geometry (**G7**) shows a reduced heat transfer augmentation due to the presence of discrete jets. This behaviour was already observed by others on single hole measurements [104] and on effusion geometries for endwall application in the work of Toni [119]. It can be explained with the greater penetration of normal jets that moves the interaction with the mainstream, and therefore the related vortical structures responsible of a greater convection, far from the plate surface.

The heat transfer augmentation factor calculated for geometry **G2** and valid for all the angled test plates, and the mean values of adiabatic effectiveness reported in Fig. 5.9, allow to compute the $NHFR$ parameter (Eq. 2.3) varying the coolant consumption. In the present study the dimensionless temperature θ, necessary to estimate the $NHFR$, has been calculated using temperature values representative of a combustor, obtaining $\theta = 1.2$. The results in terms average values of $NHFR$ are reported in Fig. 5.17. All the geometries show the same behaviour: increasing the blowing ratio and hence the coolant consumption parameter the $NHFR$ reduces and for same geometries it falls under the zero value which indicates an augmentation of the heat load that affect the gas side liner surface in blowing condition. Anyway,

the major difference between geometries is the difference rate of $NHFR$ reduction: the best performance are obtained by the **G4**, while the $NHFR$ of geometry **G5** decays rapidly increasing the blowing rate.

5.5.2 Effect of Radiative Heat Transfer

The different impact of inclination angle on the gas side heat transfer coefficient augmentation may have a relevant influence on the final metal temperature in presence of a significant radiative heat transfer. With a relevant radiative heat load it can happen that metal temperature goes up the local adiabatic film temperature; in that case a greater gas side heat transfer may have a beneficial effect on wall cooling, limiting the impact of radiation.

To compare the differences between geometries **G2** and **G7** in such type of operating condition, the Therm-1D models considered for the previous investigations have been modified by superimposing a fixed thermal radiation to the described convective heat exchanges. Radiative load was simulated considering an hypothetical gray gas emitter with a temperature of $850K$ and an emissivity of 0.5, while gas side heat transfer was modified according to the discovered augmentation factor. In the simulations the same convective temperatures of tests are employed, thus the gas emitter is considered

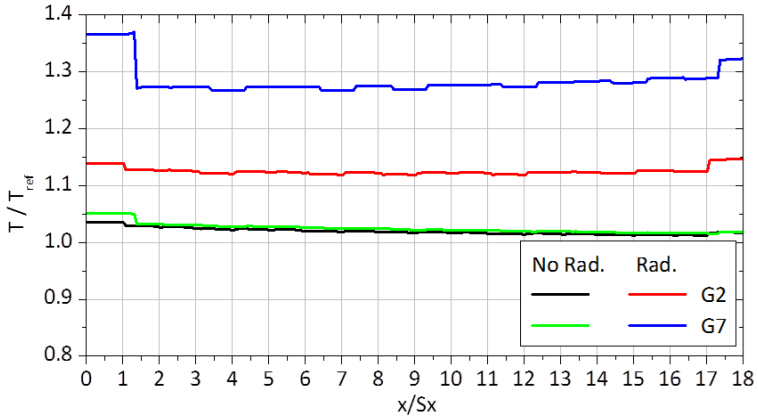

Figure 5.18: Effect of radiative heat load on geometries **G2** and **G7** for $BR = 2$

as a non participated media in the convective phenomena.

Fig. 5.18 reports the normalized metal temperature distributions along the plate for $BR = 2$ obtained with and without the additional radiative heat load. Starting from an almost coincident metal temperature, geometry **G2** is able to keep a lower metal temperature when radiation is added.

5.6 Discharge Coefficient

With the final aim of provide useful indication for effusion system optimization the knowledge of discharge coefficient of effusion system is vital for an accurate reliable design of liner cooling systems. Despite the simple configuration of the test rig without cross flow on the coolant side, the results of discharge coefficients provide good benchmark for design tools.

The discharge coefficient is the ratio of actual mass flow rate and ideal mass flow rate through the effusion perforation. The ideal mass flow rate is calculated assuming an isentropic one-dimensional expansion from the total pressure in the coolant supply plenum chamber (P_t) to the static pressure in the mainflow channel (P_s). This assumption leads to the following definition of discharge coefficient, Eq. 5.4:

$$Cd = \frac{\dot{m}_{cool}}{\dot{m}_{is}} = \frac{\dot{m}_{cool}}{P_t \cdot \left(\frac{P_s}{P_t}\right)^{\frac{\gamma+1}{2\gamma}} \sqrt{\frac{2\gamma}{(\gamma-1)RT_c}\left(\left(\frac{P_t}{P_s}\right)^{\frac{\gamma-1}{\gamma}}\right)} \frac{\pi}{4} d^2 \cdot n_{hole}} \tag{5.4}$$

The total pressure and temperature in the coolant plenum chamber where measured $50mm$ upstream of the effusion plate, while the static pressure in the mainflow is measured on the center of the lateral wall on the main channel.

The results obtained for all tested conditions are reported in Fig. 5.19 as a function of the hole Reynolds number. For the all geometries the ratio P_t/P_s is always below the value 1.1 even for the higher blowing rate conditions.

The test plates with tilted holes show a similiar values of discharge coefficient even if the test matrix offers the possibility to test different values of l/d and hole spacing: increasing the Reynolds number the Cd increases as well and

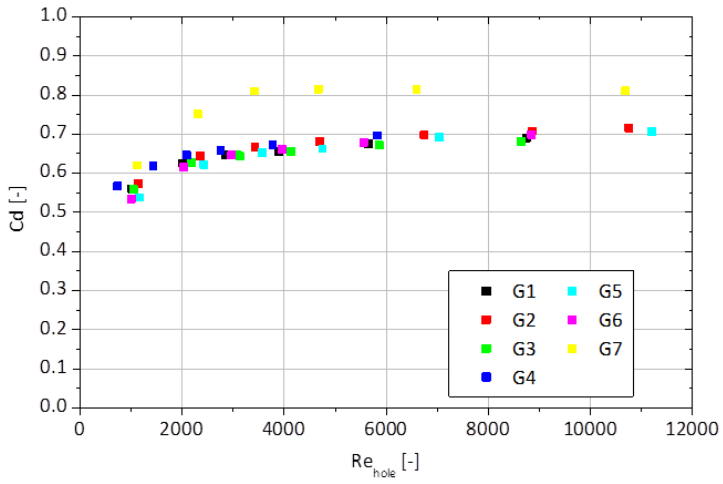

Figure 5.19: Effusion Discharge Coefficient

it reaches an asymptotic value $Cd \approx 0.7$ for $Re_{hole} > 6000$.
On the other hand a different behaviour can be appreciated for the array **G7** with normal holes. In this case the asymptotic value seems to be reached around $Re_{hole} = 4000$, moreover it has a greater discharge coefficient, close to 0.8, with respect to the other tilted plates offering a less pressure losses. This behaviour reflects the finding of Gritsch et al. [120] and Thole et al. [121]. Their flow filed measurements show that the main source of losses can be attributed to the flow separation that occurs when the flow enters the hole. The size of the separation region, which is primarily dependent on the hole angle and on the coolant feeding conditions, determines the amount of total loses. In case of plenum feeding system, like the case dealt in the present work, the minimum size of separation region and hence the maximum discharge coefficient occur for perforation with normal holes. Nevertheless, opposite behaviour it is expected for situation with cross flow on the coolant side like the actual combustor layouts (Cfr. Fig. 1.6).

5.7 Comparison of Results with Literature Data

Despite in the literature several publications regarding the topic of effusion cooling are available (Cfr. 2.3), it is quite hard to find a directly comparable work because of the large number of parameters which play a significant role (diameter, pitches, inclination, compound, turbulence, plate conductivity) and also the different post processing techniques: only really adiabatic effectiveness results are directly comparable, while overall values suffer from specific experimental conditions.

However, in order to support and compare the results with the available literature, in Fig. 5.20 are reported the lateral averaged adiabatic effectiveness results for the first rows of holes of geometry **G4** at different blowing rate. The result are compared with the data derived from the works of Martiny et al. [122] (staggered array, $\alpha = 17°, \sigma = 2.34\%$) and Kakade et al. [123] (staggered array, $\alpha = 20°, \sigma = 3.9\%$). Geometry G4 and the test plate proposed by Martiny et al. [122], which have similar levels of porosity and spacing, show comparable adiabatic effectiveness results in penetration

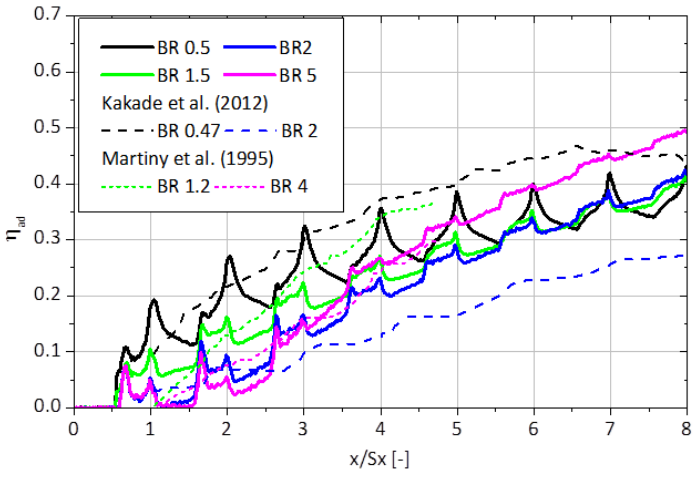

Figure 5.20: Lateral averaged adiabatic effectiveness: geometry **G4** compared with available literature

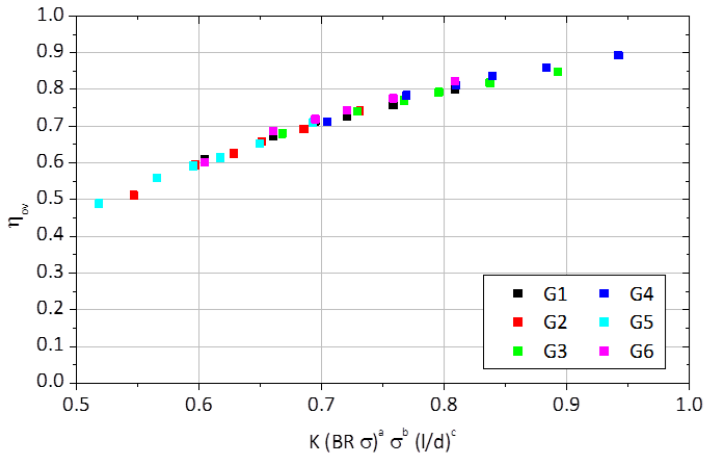

Figure 5.21: Data reduction for spatially averaged overall effectiveness for tilted geometries

regime (BR 4 and 5) in spite of the different inclination angle.

5.8 Data Reduction

In order to point out the actual thermal performances normalizing the weight of coolant consumption, a data reduction strategy is carried out for the tilted geometries; the results are re-casted in terms of spatially averaged overall effectiveness for $Tu = 17\%$ and $DR = 1$ case. Geometry G7 was excluded from data reduction because of the issues related to the actual engine flow conditions, highlighted in the previous section (Cfr. 5.5), influence the comparison with angled geometries. The final aim of the data reduction is to summarize the results and to provide a quantitative comparison between the different arrays.

The variable for data reduction is build up as a combination of three parameters that describe the phenomena involved in the liner thermal efficiency and taking into account the effect of the geometric features:

- the product of blowing ratio (BR) and the array porosity (σ) which represents the coolant consumption;

- the porosity, σ, that has direct impact on the film effectiveness and on the heat sink effect;

- the ratio between the length (l) and the hole diameter (d) which has a significant effect on the heat removed in the hole array by forced convection and on the adiabatic effectiveness.

Fig. 5.21 shows the correlation of the entire data set, for geometries with slat-hole injection, as a function of the parameters listed above:

$$\eta_{ov} = K \cdot (BR \cdot \sigma)^a \cdot \sigma^b \cdot \left(\frac{l}{d}\right)^c \tag{5.5}$$

with $K = 0.3651$, $a = 0.1262$, $b = 0.2171$ and $c = 0.2402$. Eq. 5.5 fits all the test results with a correlation coefficient of 96%, determined through a regression analysis. No extrapolation of presented equation is feasible, rather its use may be significant only within the selected range of input parameters. The data reduction is valid considering an equal perforation length, this assumption allows to perform proper comparison with the final aim to provide indication for effusion system optimization.

5.9 Concluding Remarks and Impact on Combustor Design

The experimental survey has allowed to evaluate the thermal performance of seven multi-perforated plates in terms of overall and adiabatic effectiveness. The geometries are fully representative of a portion of the combustion chamber especially near the combustor exit where the flow field is not influenced by recirculation zones and the gas flow is more uniform. The test plates have been tested imposing several values of blowing ratio and two different values of density ratio. Moreover, the effect of free-stream turbulence on film cooling is investigated on a reference geometry with two different level of turbulence ($Tu = 1.5\%$ and 17%).

As discussed in section 4.5, the adopted scaling criteria and the achieved similarities have limitations and the results, especially in terms of overall effectiveness, can not completely scaled to actual engine conditions, leaving aside the evident simple configuration of the test rig (uniform main flow conditions and no radiative heat load). However, the pure comparative purpose of the survey makes the obtained results unaffected by the issues reported above, especially comparing the geometries with slant holes injection.

On the other hand the geometry with normal hole has shown a good thermal protection capabilities when compared with traditional angled geometries. The result is ascribable to the low mainstream heat transfer coefficient augmentation and to the higher heat transfer coefficient inside hole due to the entrance effects. This unexpected behaviour makes the geometry with perpendicular holes a very interesting solution as it meets most of the industrial requirements in terms of simplicity and cost. Moreover recent study of Bhayaraju et al. [124] indicates in the normal array the best configuration, with respect to 25° degree tilted holes configuration, to damp acoustic instabilities. Nevertheless, its behaviour in a more realistic environments still remain to be verified; there are at least three basic point that can invalidate its performance in engine condition. First of all, the mainstream in the experimental apparatus does not have a 3D flow field. The high jet penetration, typical of 90° hole angle at actual engine operating conditions, could interact with the high swirled flow field of combustion chamber and influences the combustion process reducing coolant wall protection. The second issue is the absence of heat by thermal radiation in the experiments. As shown by the correlative analysis, in presence of an high radiative load the perpendicular array may a worse wall protection. The third issue is related to the scaling criteria: despite an average value of Biot number was replicated, the ratio between the HTC values inside the cooling holes and on gas side was not reproduced in the experiments. This ratio is of outstanding importance to balance the effect of film protection and heat sink effect on the resulting overall effectiveness.

Regarding the tilted holes geometries, the tests have allowed to re-

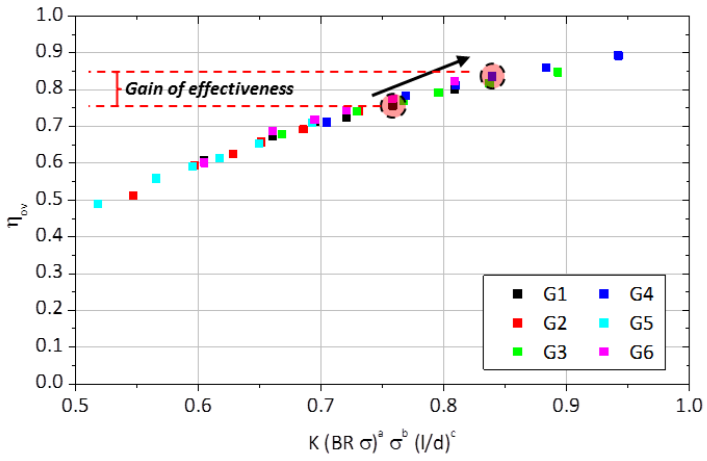

Figure 5.22: Proposed optimization strategy

cast the data of overall effectiveness providing an interesting data reduction. Starting from the data reduction (Cfr. 5.8), it is possible to summarize some general optimization guidelines. An improvement of cooling effectiveness can be obtained by increasing plate porosity, blowing ratio or the hole aspect ratio. Acting on perforation porosity, an increase of σ, higher than the usual range required for the cooling, leads to beneficial effects. However to guarantee the flow air split in the combustor chamber and the same coolant consumption the product between the representative blowing ratio of cooling scheme and the increased porosity must be kept constant, hence a lower BR value is required. Being the exponents of σ greater than the exponent of blowing ratio in the data reduction parameter, working with effusion plate with higher porosity and consequently lower BR leads to an improvement in cooling efficiency.

Beyond that the parameter l/d, actually fixed by manufacturer capabilities, has a beneficial impact on cooling performance. It suggests to work with an high number of micro-holes.

When the experimental overall effectiveness values are used to select new operating conditions to optimize the cooling systems, it is necessary also to consider the relative contribution of the heat sink effect and the reduction

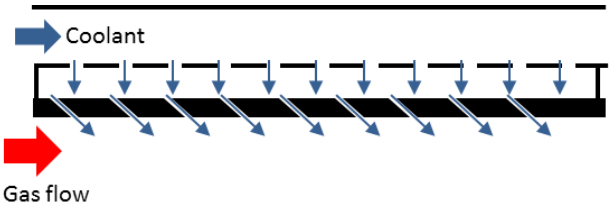

(a) Double skin: impingement with effusion plate

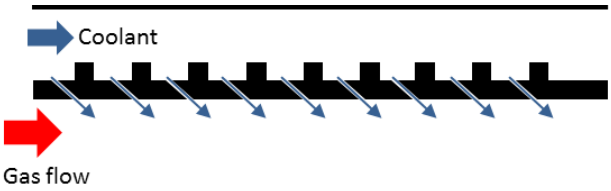

(b) Effusion plate with turbulators on cold side

Figure 5.23: Feasible solutions to reduce the effective pressure drop across liners

of the heat load on the gas side (i.e. $NHFR$) on the global heat balance of the liner. This additional care is due to the limitation imposed by the adopted scaling criteria discussed in section 4.5. To overcome this issue the new configuration should allow not only an increase of overall effectiveness but also an increase of both heat sink effect capability and $NHFR$.

Taking into account the previous considerations, let's consider the array **G1** at $BR = 3$ as reference condition, the proposed optimization strategy suggests to switch to a configuration with high porosity array, such as geometry **G4**, working at $BR = 2$ in order to keep constant the coolant consumption. As shown in Fig. 5.22 the overall effectiveness increases of about 20%, moving from $\eta_{ov} = 0.75$ to 0.95. This selected new configuration allows also to increase both the heat sink capability (Fig. 5.11) and to reduce the heat load on the external surface (Fig. 5.17).

It is worth to notice that in the previous consideration the thermal radiation is not taken into account. However it is expected that its impact on relative weight between heat sink effect and adiabatic film effectiveness does not have a significant effect on the analysis, considering the actual radiative level of modern combustor chamber.

Concerning the optimization previously discussed, some considerations regarding the possible impact of the proposed strategy on combustors design are necessary.
The new selected operating condition request to lower the blowing ratio. This flow parameter is directly linked to the overall combustor wall pressure drop and it is actually a design target not a quantity that can be freely selected. However feasible solutions to reduce the effective pressure drop across the multi-perforated liners and hence the blowing ratio, such as double skin configurations (Fig. 5.23(a)) and multi-perforated liners with turbulators on the cold side (Fig. 5.23(b)), are well known in literature [125, 126]. Despite they introduce complexity in combustor design, are very interesting for their cooling capabilities enhancing in addition the heat transfer coefficient on the cold side.

The proposed optimization highlights the effect of coolant velocity (i.e. blowing ratio) and above all the impact of porosity on cooling performance, which are the main parameters that, as discussed in section 1.3.1, affect the acoustic damping capabilities. The optimization strategy seems to be promising from an acoustic standpoint in accordance with the results reported in a previous work [63] directly linked to the current research.

Effusion Cooling Performance with Representative Mainstream Conditions

Chapter 6

Cold Sector Test Rig

Contents

The experimental campaign on planar plates has highlighted the thermal behaviour of the effusion cooling system and moreover the influence of geometric and fluid dynamic parameters (Cfr. 5). However the survey has been carried out with uniform mainstream conditions, and the effects of a swirled main flow still remain an open question.

The high amount of air admitted through a lean-burn injection system is characterized by very complex flow structures such as recirculations, vortex breakdown and processing vortex core, that may deeply interact in the near wall region of the combustor liner. This interaction and its effect on the local cooling performance make the design of the effusion cooling systems very challenging, accounting for the design and commission of a dedicated test rigs for detailed analysis.

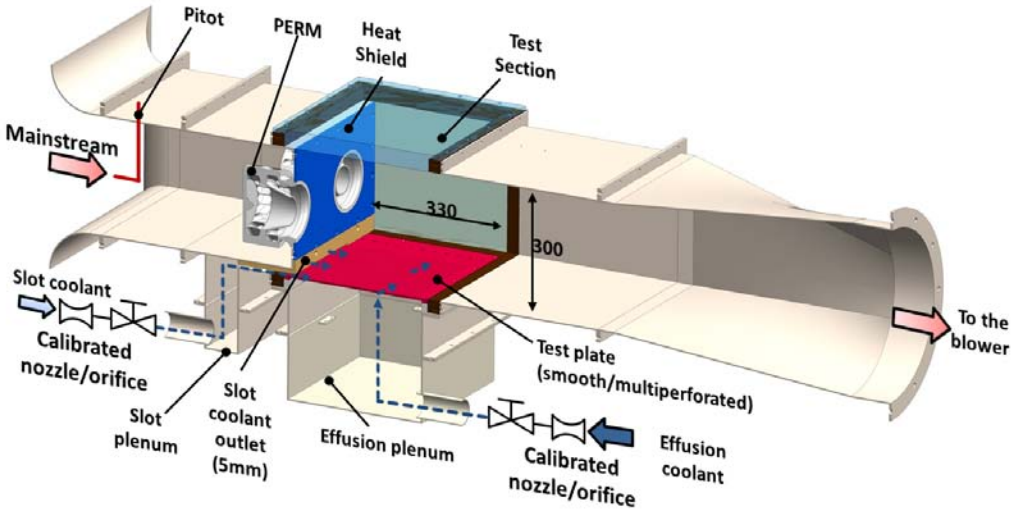

Figure 6.1: Cold Sector Test Rig

6.1 Experimental Apparatus

The experimental arrangement, depicted in Fig 6.1, consists of a non-reactive three sectors planar rig installed in an open loop wind tunnel (*Cold Sector Test Rig, CSTR*), the test model is characterized by three burner and a complete cooling scheme made up of a slot injection and an effusion array. A picture of the experimental facility is reported in Fig. 6.2 where it is possible to observe the layout of the test rig.

The test rig allows the control of three separate flows: the mainstream, the slot and effusion cooling flows. The mainstream is drawn by means of a $90kW$ centrifugal blower with a maximum flow rate capability of about $8400m^3/h$ at atmospheric pressure and ambient temperature; the flow rate can set up by guiding the motor speed between 300 and 1800 rpm. Before entering into the test section, the mainflow passes trough an inlet bell mouth and a $650mm$ long entrance region with constant cross section; afterwards it is swirled by a set of injectors fixed in a planar arrangement at a vertical plate reproducing the combustor dome. Three swirlers are installed to guarantee the periodicity typical of an annular combustor chamber, and to avoid sidewall effects on the central investigation area.

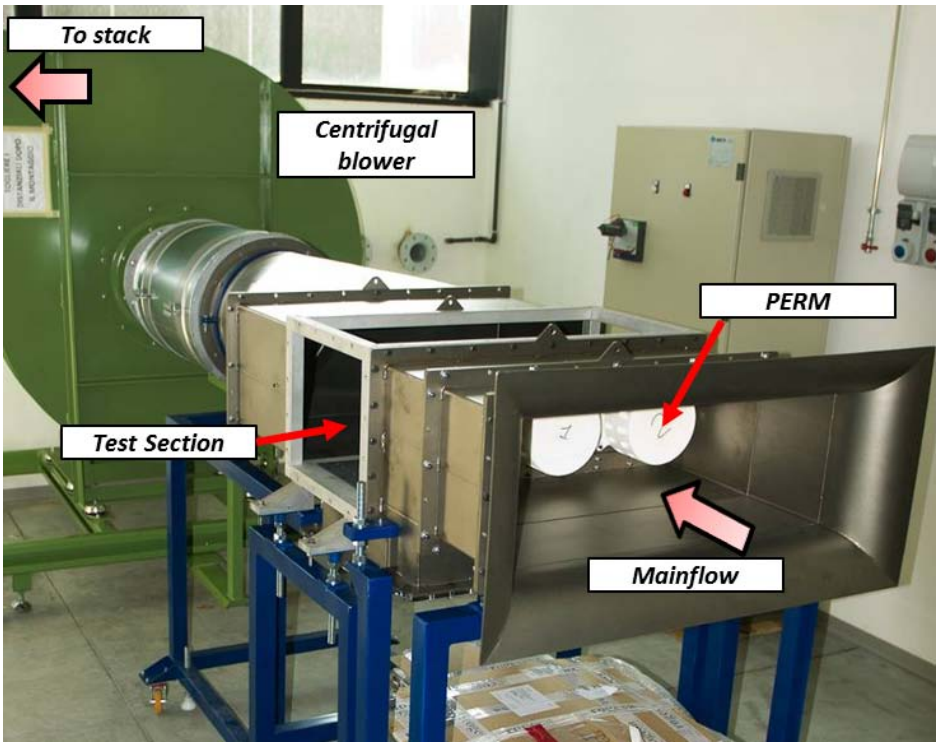

Figure 6.2: Test Rig

The scaled swirlers reproduce the real geometry of a PERM (Partially Evaporated and Rapid Mixing) injector; they are made of plastic material and realized using a rapid prototyping technique. The PERM injectors are developed for Ultra Low NO_x (ULN) combustor core technology and are addressed to achieve partial evaporation inside the inner duct and a rapid mixing within the combustor, optimising the flame position and the stability of the combustion process. they are characterized by two radial co-rotating primary and secondary swirlers used to assign angular momentum on two distinct inlet air flow; before they enter in the combustion region the swirled flows are accelerated in the inner and the outer nozzle thanks to a conical internal body (Cfr. 1.3). A scheme of the PERM injector tested in the experimental apparatus is reported in Fig. 1.10.

Figure 6.3: CSTR test section

The test section (about $300mm$ x $750mm$; $330mm$ long) is representative of an aero-engine lean combustor chamber scaled with respect to the actual configuration (Fig. 6.3). The tested geometries, which represent the inner liner of the combustion chamber, are screwed on the bottom wall of the test section. Two different plates have been tested: a smooth and a multi-perforated plate. A slot system is used to generate film cooling in the very first part of the test section, it is fed using a plenum chamber connected directly upstream the slot exit and equipped with screens and flow straighteners. The slot exit is located below the three burners; it has a constant height of $6mm$ and it extends between the axis of the two lateral swirlers. Another plenum chamber located directly upstream the liner geometry is used to issue the cooling flow to the holes of the multi-perforated test plate. A sketch of the test section, where are visible all the features illustrated above, is reported in Fig. 6.4; while in Fig. 6.5 is reported the cross sectional view of the combustor chamber replicated in the test rig with the expected flow field in reactive conditions. Downstream the test section, the mainstream, mixed with the cooling flow issued by the slot and the effusion system, flows trough a constant cross-section channel and a smooth converging duct directly connected to the silencer installed at blower inlet. The test rig, including the inlet mouth and the exhaust converging duct, is about $2100mm$ long, it is mainly manufactured using stainless steel $5mm$ thick.

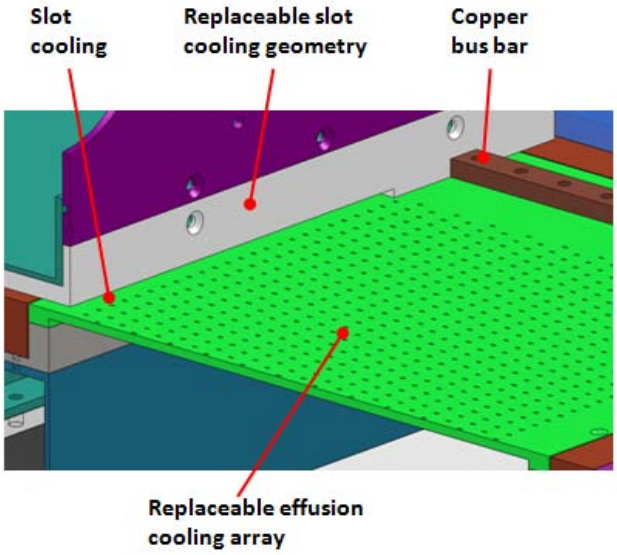

Figure 6.4: Sketch of the test section

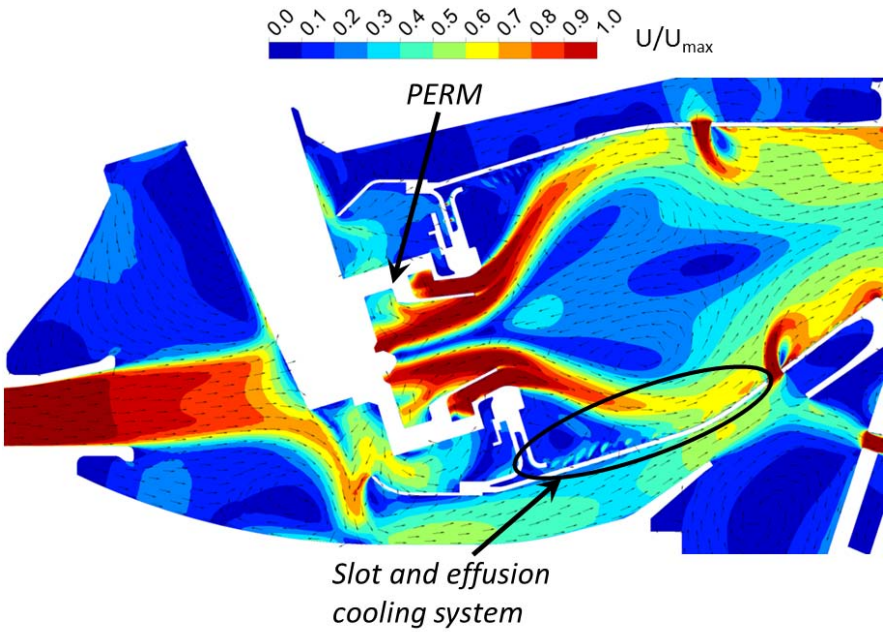

Figure 6.5: Cross sectional view and expected flow field of the reference combustor chamber reproduced in the test section [127]

The test model is instrumented to perform heat transfer coefficient, adiabatic effectiveness and flow field measurements. Heat transfer coefficients are obtained using TLC paint to measure the wall temperature by means of a steady state technique (Cfr. 3.4). The uniform surface heat flux is generated by Joule effect with a $25.4\mu m$ thick Inconel Alloy sheet glued on the test plate. A DC power supply (Agilent®N5763A) is used to feed the Inconel sheet through two copper bus bars fixed on sides of the test plate near the lateral windows. Wide band TLC 30C20W supplied by Hallcrest and active from 30°C to 50°C are used. Crystals are thinned with water and sprayed with an airbrush on the Inconel sheet after the application of a black background paint. The TLC color play on the smooth test plate can be appreciated in Fig. 6.6. The cooling flow is drawn directly from the ambient using two separated lines equipped with calibrated nozzles to estimate the mass flows.

Adiabatic effectiveness tests are performed using the Pressure sensitive paint technique with the intensity method approach (Cfr. 3.2). For this kind

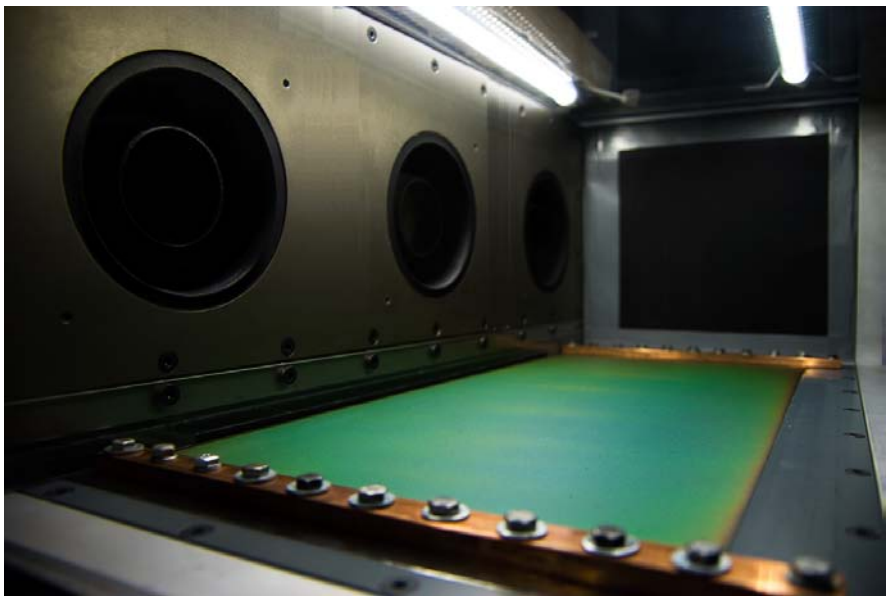

Figure 6.6: TLC color play on smooth test plate

of measurements the test plate is once again sprayed with several light coats of PSP first removing the TLC coating. Regarding the paint excitation, it is provided by an high performance led illuminator DLR-IL104®and the PSP emission is captured by a CCD camera PCO.1600. The illuminator, equipped with a special lens for UV light, provides an uniform illumination spot of about 0.36m of diameter at 1 meter distance.

The selected foreign gas used to perform adiabatic effectiveness is nitrogen stored in a $10bar$ pressure tank. It is used to feed the effusion and the slot plenum chamber, according to the experimental procedure, using two dedicated feeding lines equipped with orifices to measure the cooling flow rates.

Flow field measurements are performed on several plane inside the test section using the 2D PIV technique described in details in section 3.1. The positioning of the camera/laser system is done using a traverse system with the help of a dedicated calibration device located inside the test section. The laser sheet is always generated parallel to the test plate, for this reason when measurements on plane perpendicular to the liner are performed a $45deg$ mirror is used to deviate the laser beam. The seeding necessary for the PIV measurements is introduced upstream the intakes of the mainstream and cooling flows by means of a Laskin nozzle [84].

Since PIV, TLC thermography and PSP techniques require wide optical accesses, the top and the lateral sides of the test rig are made of transparent PMMA (Poly-Methyl Methacrylate): three transparent windows are screwed to a central frame constituting the test section. The cameras for PSP and TLC techniques within the illumination systems focus the test plate from the top window and they are fixed on a dedicated frame.

The pressure drop across the swirlers and hence the mainstream mass flow is imposed guiding the rotating speed of the centrifugal blower trough an inverter. Regarding the effusion and slot mass flow rate, they are set up by throttling the valves located on the two separated cooling line as depicted in Fig. 6.1.

The main mass flow is measured using a Pitot tube positioned $30mm$

downstream the rig inlet mouth in the center of the entrance region, and double checked measuring the swirlers pressure drop and knowing the effective area of the injector system. The effective area is measured using a dedicated test campaign aimed at performing the flow check of the swirlers [128]. On the other hand, the cooling flow rates are estimated using calibrated nozzles or by means of orifice, according to EN ISO 5167-1 [107], when respectively air or foreign gas is used to feed the two coolant plenum chambers.

A pressure scanner Scanivalve DSA 3217 with temperature compensated piezoresistive relative pressure sensors measures the static pressure in 12 different locations:

- Two pressure taps are placed in the entrance region of the test model;
- two pressure taps are located downstream the test section in the main channel;
- for each coolant plenum chamber two static pressure taps are employed.

Several T type thermocouples connected to a data acquisition/switch unit (HP/Agilent®34972A) measure the mainstream at the inlet and outlet of the test section, and the coolant static temperatures in the plenum chambers.

6.2 CFD Calculations to Support Test Rig Design

CFD calculations have been performed to asses the rig operability and to support the design of the test model. The simulation have been performed using the commercial code Ansys CFX®14 following a steady state RANS approach.

The objective of the CFD investigation is to verify that the flow field generated by the three injectors is periodic so as to have significant future measurements in front of the central swirler and the entrance and outlet region are long enough to avoid influences on the test section. The computational domain with a detailed view of the mesh in the plane of the injector is

reported in Fig. 6.7. It includes the whole domain of the main flow field, and the mesh is composed by $20.3 \cdot 10^6$ cells using tetrahedra and prism elements.

The calculations have been performed at isothermal conditions using the well-known $k - \omega$ SST turbulence model with the following boundary conditions:

- Inlet: imposed mass flow rate.
- Outlet: uniform static pressure.
- The domain in the test section is divided in three regions, one for each swirler, separated by planes with free slip condition.

(a) Computational Domain

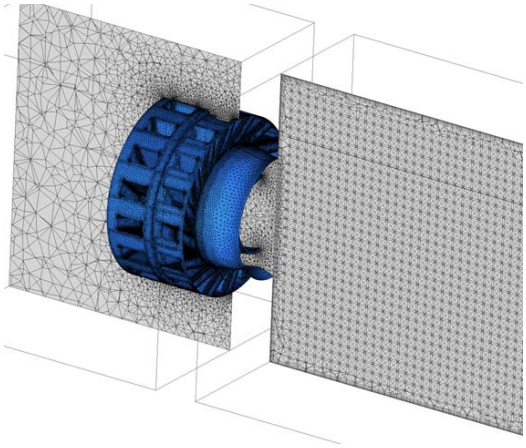

(b) Mesh Details around PERM

Figure 6.7: Setup for CFD simulations

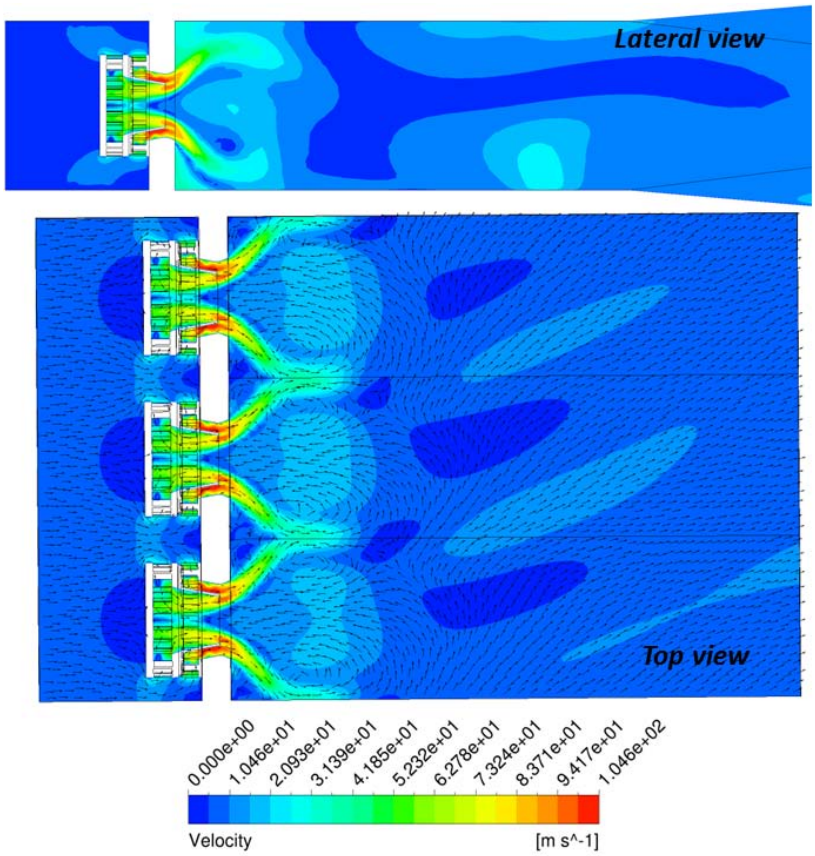

Figure 6.8: Velocity contours from CFD simulations

Fig. 6.8 reports a combined vector-contour map of the velocity module where it's possible to observe an acceptable repeatability of the flow field generated by the three swirlers. Moreover the velocity contour on the central swirler from lateral view highlights that the downstream test rig contraction seems to be far enough from the swirling flow region.

6.3 Scaling and Design Criteria

Experiments under real engine conditions usually require huge efforts in the development of the experimental setup and also in the application of measurements techniques. Considering the final aims of the work which are

the full characterisation of flow field, its interaction near the wall with the cooling system and the measurements of thermal performance of the cooling arrangement, the achievement of this objectives is challenging in a real combustion chamber. Moreover, the need to provide high detailed results, gave reason for the design of a test rig working at nearly atmospheric conditions with no reactive flow.

In order to ensure comparability with the engine conditions, a dimensional analyses aimed at identify the relevant dimensionless quantities were performed in the first design phase of the rig. With the final aim to perform HTC and adiabatic effectiveness measurements, the relevant parameters considered during the preliminary design phase of the test rig are divided in two categories, one for the mainstream and one for the cooling flow. For the main flow, drawn from the ambient at atmospheric condition, the relevant parameters are, Eq. 6.1:

$$Re_{main} = \frac{\dot{m}_{main} \cdot d_h}{A_{ref} \cdot \mu_{main}} \qquad \Delta P/P = \frac{P_{inlet} - P_{oultet}}{P_{inlet}} \tag{6.1}$$

where the Reynolds number is evaluated using the cross section area and the hydraulic diameter of the test section as reference length d_h; while the $\Delta P/P$ represents the non dimensional pressure drop across the burner evaluated using the static pressure in the main inlet channel (*inlet*) and downstream the test section (*outlet*). This last parameter is directly linked to the mainstream Mach number and consequently to the reduced mass flow.

Due to the necessity to work at atmospheric conditions and considering the maximum mass flow rate limited by the characteristic of the blower, it is not possible in the CSTR to replicate both the Reynolds and pressure drop across the injectors (Eq. 6.1). As the combustor pressure drop can be considered the most important parameter in the definition of the flow field inside the combustor, it was decided to replicate only such parameter neglecting the Reynolds number similitude. Anyway to obtain a mainstream Reynolds number in fully turbulent regime and to achieve e good resolution of the measurements in terms of flow field and spatial accuracy of the optical measurements, the test model has been designed in a 3:1 scale with respect

to actual engine configuration. Such scale factor represents the maximum value that can be selected considering the capability of the facility.

Despite the pressure drop across the swirler will be replicated during the experiments, the expected flow field in the test section will be different with respect to reactive condition, as extensively discussed in section 2.1. Nevertheless, the cold flow field can be considered representative of the flow inside a lean combustor chamber, moreover it allows at the same time to stress the liner cooling system as required to reach the objectives of the survey.

In a real annular aero-engine combustion chamber for regional turbofan about 18 swirlers are equally distributed along the engine circumference, for this reason the flow field can be considered periodical. The capability of the facility in terms of mass flow does not allow to test all the annular combustion chamber at enlarged scale, however to reproduce such periodicity and to avoid sidewall effects, it was decided to install three swirlers: this compromise solution has been supported by CFD survey discussed in section 6.2. Moreover for the necessity of the selected measurements techniques, in particular TLC thermography, a planar arrangement of the injectors has been selected: the resulting planar effusion liner allows to perform more accurate and detailed measurements reducing at the same time the complexity of the rig.

Regarding the cooling line, first focussing on the effusion system, the relevant parameters that affect adiabatic effectiveness, heat transfer distribution and the interaction with the main flow are, Eq. 6.2:

$$Re_{eff} = \frac{\dot{m}_{eff} \cdot d}{A_{hole} \cdot \mu_{cool}} \qquad DR = \frac{\rho_{cool}}{\rho_{main}}$$
$$\Delta P/P_{eff} = \frac{P_{eff} - P_{oultet}}{P_{cool}} \tag{6.2}$$

The last parameter is the pressure drop across the effusion array directly proportional to the mean velocity ratio. Once again, the adopted scaling criteria described for the main flow and the capability of the facility do not allow to reproduce all the parameters listed in Eq. 6.2. The main scaling parameter considered and replicated during tests is the effusion pressure drop.

Moreover, using air and nitrogen at ambient temperature for the cooling line (Cfr. 6.1), the obtained density ratio at test condition is $DR = 1$.

The main issues related to the choice of such scaling criteria, down to atmospheric pressure conditions, are the reduced levels of Reynolds number inside the cooling holes and density ratio with respect to actual engine conditions. Despite typical values above 25000 in actual engines, tests shows hole Reynolds numbers lower than 5000, well below the typical engine data even if they are still in fully turbulent regime. Moreover the density ratio, is far below the actual combustor chamber conditions, typical it is around $DR = 2.5$.

The holes Reynolds number is expected to have a reduced impact on the measured thermal quantities, which are more influenced by the pressure drop and to the density ratio. It has a negligible influence on the turbulent generation at hole outlets that could impact on heat transfer and film covering especially in a limited region around holes. On the other hand, the density ratio has an impact on the adiabatic effectiveness distribution particularly in the transition between mass addiction and penetration regime and its effect seems to be negligible in full penetration regime. These aspects have been already debated by the author by means of dedicated experimental survey reported in the first part of the current research (Cfr. 5). Regarding DR impact on heat transfer distributions, previous studies performed by the author's research group and discussed in the introduction of the present work (Cfr. 2.2.2), have demonstrated that the main scaling parameters of HTC augmentation in combustor effusion cooling situations is the velocity ratio directly linked to the effusion pressure drop.

The cooling system of the CSTR considers a slot injection realized on the heat shield. Tests are performed imposing different values of the slot mass flow to simulate several levels of coolant consumption W; this parameter is defined as the ratio between the slot and the mainstream mass flow:

$$W = \frac{m_{slot}}{m_{main}} \cdot \frac{3}{2} \tag{6.3}$$

Engine Reference Conditions	CSTR Exp Conditions
Annular combustor 18 PERM injectors	Planar sector, scale 3:1 3 PERM injectors
$Re_{main} = 540000$; $\Delta P/P_{main} = 3.5\%$	$Re_{main} = 160000$; $\Delta P/P_{main} = 3.5\%$
$Re_{eff} = 25000$; $\Delta P/P_{eff} = 3\%$ $DR = 2.5$	$Re_{eff} = 5000$; $\Delta P/P_{eff} = 3\%$ $DR = 1$
$W = 3\%$; $Re_{slot} = 15000$	$W = 3\%$; $Re_{slot} = 4000$

Table 6.1: CSTR similarity and design criteria

the coefficient 3/2 in the Eq. 6.3 takes into account that in the test section the slot is located between the axis of lateral swirlers, covering only two sectors. The coolant consumption can be considered representative of the slot blowing rate. In slot cooling situations, the blowing ratio is the relevant parameter affecting the adiabatic effectiveness distributions.

However, as reported for the effusion system, the slot Reynolds number, defined using the slot height, assumes values in the order of $Re_{slot} = 4000$, below typical engine values. This discrepancy with respect to the engine condition can influence the HTC distribution especially in the first part of the liner where the slot flow acts its covering. Nevertheless, the slot Reynolds number is reduced, respect to the engine reference condition, with about the same ratio expected for mainstream Reynolds number (about 3.5 times). This aspect allows the scaling of HTC results to engine conditions with good confidence.

To summarize, the design criteria and the values of the main similarity parameters are reported in Tab. 6.1.

6.4 Test Matrix

The experimental campaign is performed imposing several fluid dynamics conditions ranging among typical engine values. In order to separate the effect of slot system an effusion cooling system, two different test plates are tested: a smooth test plate (made of PVC; $k_{PVC} = 0.177 W/mK$); and a

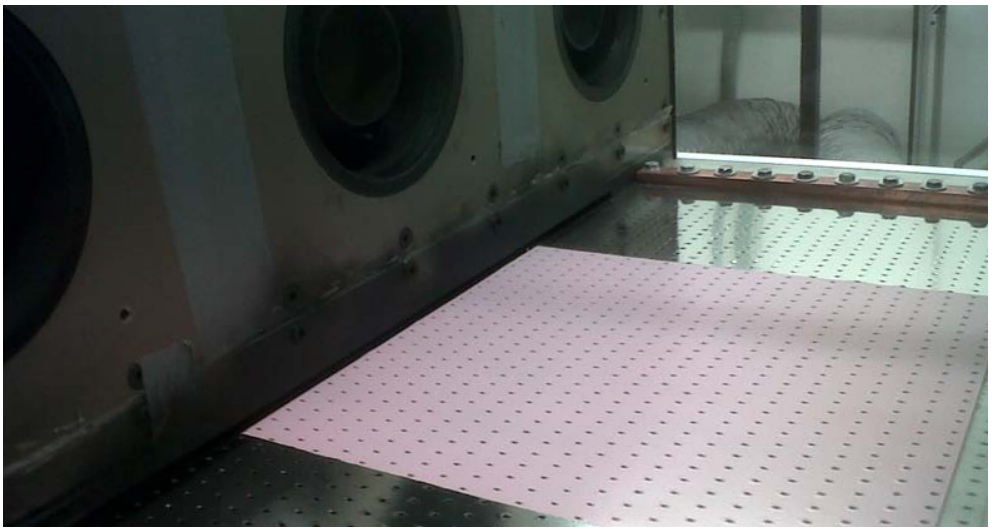

Figure 6.9: Effusion Array coated with PSP

multi-perforated plate to investigate the complete liner cooling arrangement (made of ARNITE; $k_{Arnite} = 0.29W/mK$ - $\rho = 1360kg/m^3$). The slot system has a constant section area, $6mm$ thick, and it is extended in the central region of the test section between the axis of the two lateral swirler as described in section 6.1.

The effusion cooling array has been designed starting from the pattern of the geometry G1 tested in the first part of the current research (Cfr. 5). It consists of a staggered array of 1236 circular holes (24 rows, $d = 1.55mm$), with an inclination of 30deg, drilled in a $5mm$ thick plate, with a length to diameter ratio of $l/d = 6$. The spanwise and the streamwise pitches are respectively $S_y = 9.9mm$ and $S_x = 12.6mm$.

In order to perform the HTC measurements by means of TLC thermography, the test plates are made in low conductivity material and covered with a thin heating foil made of Inconel 600®(thickness 0.0254mm). The Inconel sheet is electrically supplied by two lateral copper bus bars connected to a low voltage DC generator. It should be remarked that the sheet has exactly the same hole pattern of the plate. Depending on the experimental technique, the Inconel sheet is coated with TLC or PSP; a view of the effusion test plate with central region painted with the light pink Pressure Sensitive

Configuration ID	Description	Tests
LM0	Smooth test plate without coolant injection (slot system disabled)	PIV, HTC
LM1	Smooth test plate with Slot cooling system enabled	PIV, HTC
LM2	Multi-perforated test plate with slot and effusion cooling systems	PIV, HTC, η_{ad}

Table 6.2: CSTR Test Matrix

Paint is reported in Fig. 6.9.

With respect to the thermal conductivity values indicated above for the test plates, k_{PVC}, being the smooth plate made of a certified material, derives from material databases; k_{Arnite} has instead been measured according to standards ISO 8302 by a certified research centre. It is well worth to note that the exact conductivity knowledge will avoid the introduction of a further uncertainty source within the experimental data post-processing (Cfr. 3.4).

The two different test plates involved in the analysis and the presence of slot and effusion cooling systems leads to the definition of three different configurations of test model summarized in the Tab. 6.2, including the typologies of measurements performed.

Flow field measurements using 2D PIV technique are performed for all the test model configurations, thanks to the large optical accesses, it is possible to introduce the light sheet at different locations: measurements are carried out on planes (Fig. 6.10) positioned either orthogonal (*center plane*) and parallel (*median plane*) to the liner wall passing for burner axis, and on a plane parallel to the liner $4mm$ above the wall (*wall plane*). Concerning the *center plane*, the investigation area, about $150mm$ x $250mm$, is too large to be covered with a single framing and at the same time to guarantee enough image resolution for subpixel interpolation: as a consequence, 8 different camera/laser positions are employed to cover the whole *center plane*, with a scale factor of ≈ 9. To avoid loss of information, each camera framing

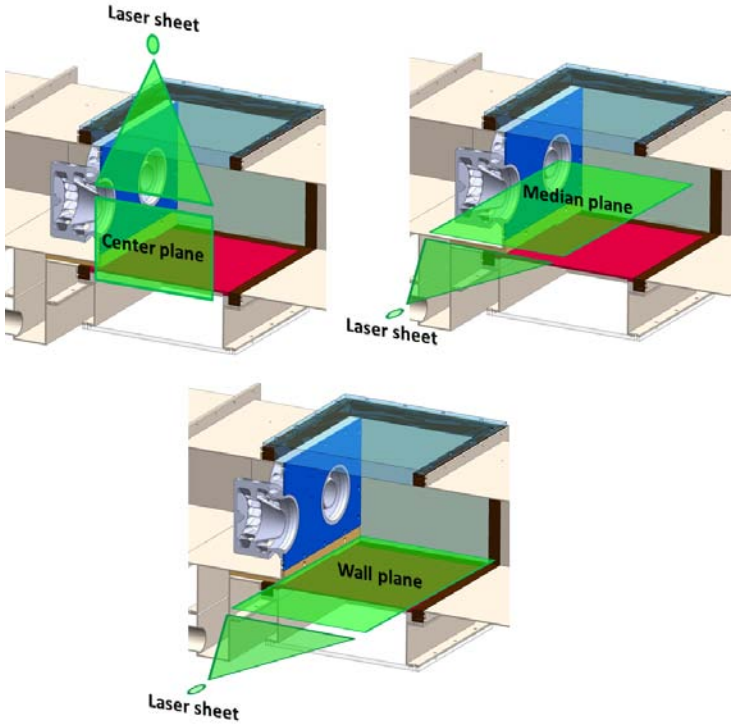

Figure 6.10: Positions of PIV measurements plane

is overlapped with the neighbouring ones of about $5mm$ for each side. The same approach has been employed also for the *median and wall plane*: here, 16 camera framing are taken to cover two sectors and thus to investigate an area of about $450mm$ x $250mm$.

The main investigation parameter of the mainflow is the pressure drop across the burners defined in Eq. 6.1. Tests are carried out imposing three different values of pressure drop in the range $2 - 5\%$. In the range of the imposed pressure drop, the Reynolds number, evaluated using the hydraulic diameter of the test section, is between $129000 - 200000$.
Concerning the cooling system, different values of the slot cooling mass flow are set up to simulate three levels of coolant consumption W (Eq. 6.3) in the range $0 - 3\%$. For test with multi-perforated plate (**LM2**), several pressure drop across the liner cooling system $\Delta P/P_{eff}$ (Eq. 6.2) are set in the range $0 - 3\%$ to reproduce the velocity ratio of the effusion array.

6.5 Impact of Results on Combustor Design

Starting on the adopted scaling criteria discussed in details in the section 6.3, it is necessary to spend few words on how the results will impact on combustor design.
First of all, let's consider the flow field measurements performed by PIV technique with and without cooling injection. Despite the cold flow field it is not fully representative of the flow inside the combustor chamber, the PIV survey gives useful information regarding the interaction of coolant and swirled main flow and how this interaction reflects on the thermal behaviour and on the typical flow structures. Detailed 2D velocity contours are hence of outstanding importance to optimize the hole pattern and they represent, of course, a severe benchmark test for CFD calculations.

Regarding the heat transfer coefficient distributions, the adopted scaling criteria allows to extrapolate results, with sufficient confidence, to the engine conditions when they are normalized with correlations for turbulent flow, such as the *Colburn's correlation*. The lateral averaged Nusselt number distributions find applications especially in the first phase of combustor design when reliable HTC trends are necessary for the 1D design tools.

The adiabatic effectiveness generated by the cooling system is well reproduced in similarity in the test rig. Results can be used to highlight critical region, the behaviour of the cooling flow on liner wall and moreover they could suggest possible effusion pattern optimizations.

Chapter 7

Flow Field of PERM Injector

Contents

In this chapter the extensive survey performed on the cold sector test rig through 2D PIV technique will be illustrated. In the first part the analysis deals with the mean flow field generated by the lean injection system in absence of cooling flow, while in the second part the effect of the cooling system will be investigated focussing on the near wall effects.

The space coordinates are normalized with respect to the exit diameter of the PERM injector D, while the different configurations of the test model refer to the acronyms listed in Tab. 6.2.

7.1 Flow Field Characteristics

Figure 7.1 illustrates the characteristics of the flow field generated by the three burners for the reference working condition, $\Delta P/P = 3.5\%$, on the *center plane* without cooling flow. The distribution reports the magnitude of the velocity measured on the investigation plane normalized with respect to the maximum.

The main features of the swirled flow are the corner vortex, the central

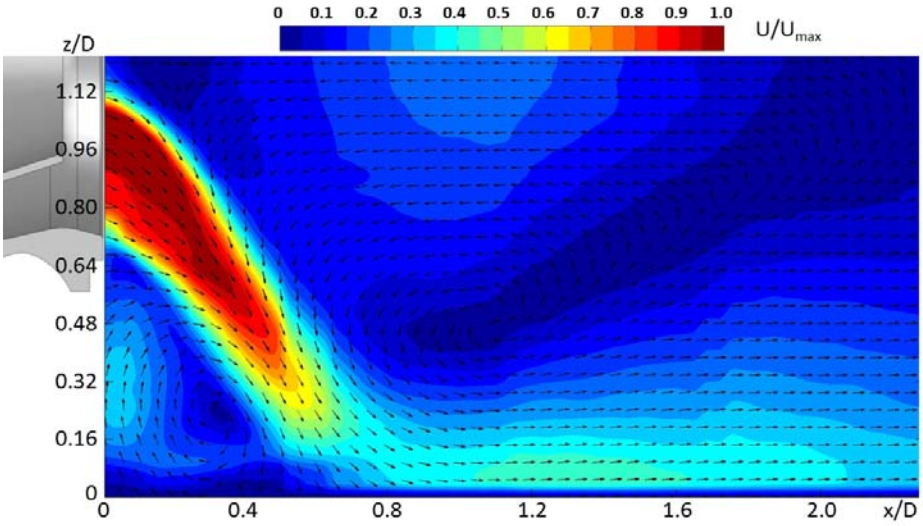

Figure 7.1: Flow field on center plane

RCZs generated by the vortex breakdown and the high velocity jet at swirler exit; the presence of the large recirculation zone indicates that the swirl number is beyond the value of 0.6 [38]. The jet, exiting from the swirler, deviates toward the liner surface with an angle of about $35°deg$, after which it is subjected to a rapid deceleration before it reaches the wall. The jet impinges on the liner wall generating a stagnation point at about $x/D = 0.6$. Slightly downstream, at $x/D = 1.1$ and $z/D = 0.48$, it can be observed the center of rotation of the recirculating flow: it causes the acceleration of the impinging jet near the wall resulting in an high axial velocity gradient. Similarly, at the same non dimensional abscissa, an high velocity bubble is highlighted on the centreline of the swirler.

Under the high velocity jet, in the area limited by the heat shield and the liner wall, a typical corner RCZ is established; this flow structure rotates in the clockwise direction resulting in negative velocity component in x direction at the liner surface.

The velocity field on the *median plane* is shown in Fig. 7.3: the streamlines illustrate the closure of the central recirculating flow at about $x/D = 2$ on the central swirler axis. The central RCZ is sustained by two macro vor-

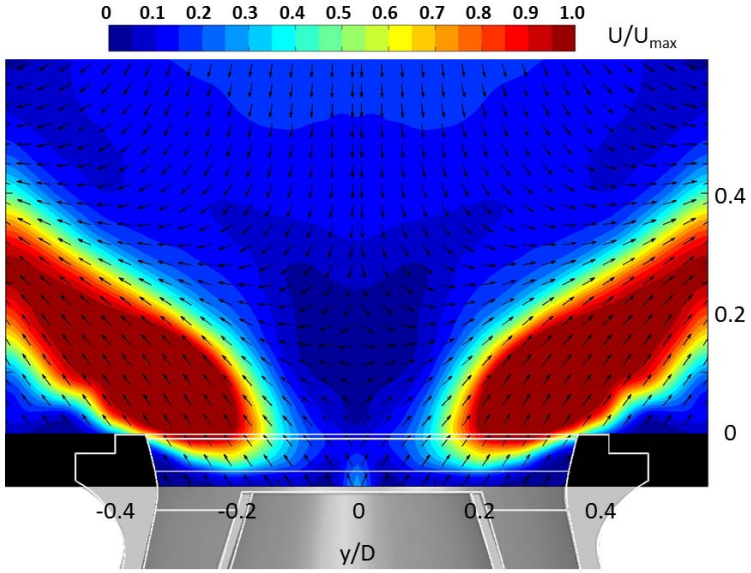

Figure 7.2: Zoomed view of the flow field on center plane

tices symmetrical with respect to the central axis. The jets of neighbouring injectors, after a deceleration, generate a region of strong interactions with high velocity in axial direction. Moreover under this structure near the heat shield, the flow field is characterized by low velocity recirculation regions with two counter rotating vortices. In addition, the behaviour of the central swirler seems to be not influenced by the lateral walls resulting in a periodic distribution.

To deeply understand the behaviour of the flow field at the injector exit, an additional dedicated survey is performed on the central burner on the median plane. The camera is tilted of about $10°deg$ with respect to the direction normal to the liner surface and it is positioned more close to the injector in order enhance the measurement resolution. This new set up allows to catch the flow field $10mm$ upstream the heat shield plane, inside the injector. Nevertheless, the main drawback is that the images acquired suffer from perspective distortion, meaning that the scale factor is not constant, but varies across the camera field of view. To correct such perspective distortion, the vector maps derived from warped images are compensated us-

ing a de-warping procedure implemented in the commercial software Dantec FlowManager®.

The zoomed view is reported in Fig. 7.2; the vector map confirms that the main recirculation region starts from $x/D = 0.1$ on the centreline; upstream the heat shield plane, the velocity has positive components in x direction and the swirler jets are subjected to a strong acceleration immediately before the burner exit.

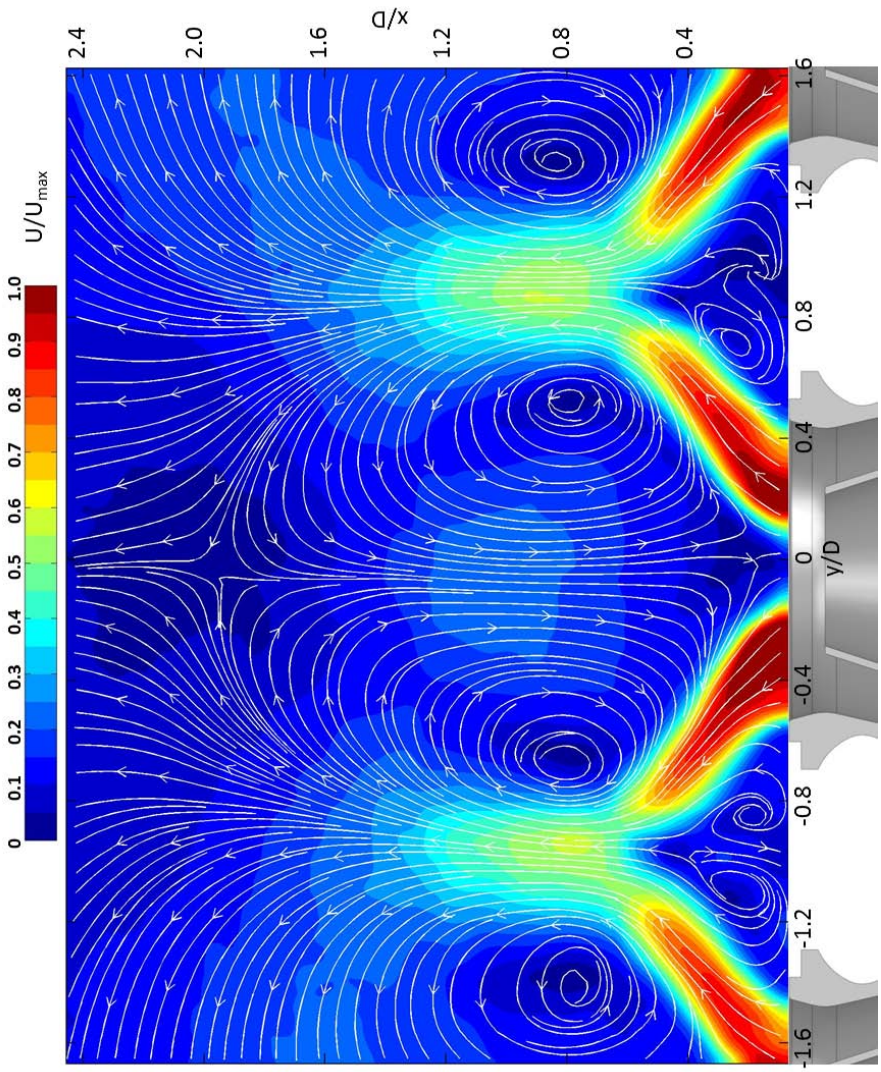

Figure 7.3: Flow field on median plane

7.2 Impact of Slot Injection

In order to deepen the behaviour of the slot cooling system, a dedicated PIV survey is carried out in the area of the corner RCZ on the *center plane* and on the *wall plane*. Focusing on the velocity flow field at $W = 3\%$ in the first plane of measurement (Fig. 7.4), it is clear how the coolant issued by the slot is early lifted up by the backward recirculating flow (light blue area near the lateral wall). As underlined in the previous section the corner vortex rotates in the clockwise direction generating a flow near the wall that moves against the slot flow.

This aspect is underlined by Fig. 7.5, which shows the axial velocity normalized with the velocity magnitude: the interaction between the coolant and the corner vortex causes the lift of the slot flow and clearly alters the shape of the recirculation with respect to the no blowing condition ($W = 0\%$). Furthermore, the injection of slot cooling flow causes the deflection of the swirler jet: the exit angle increases and the impingement location is slightly moved downstream.

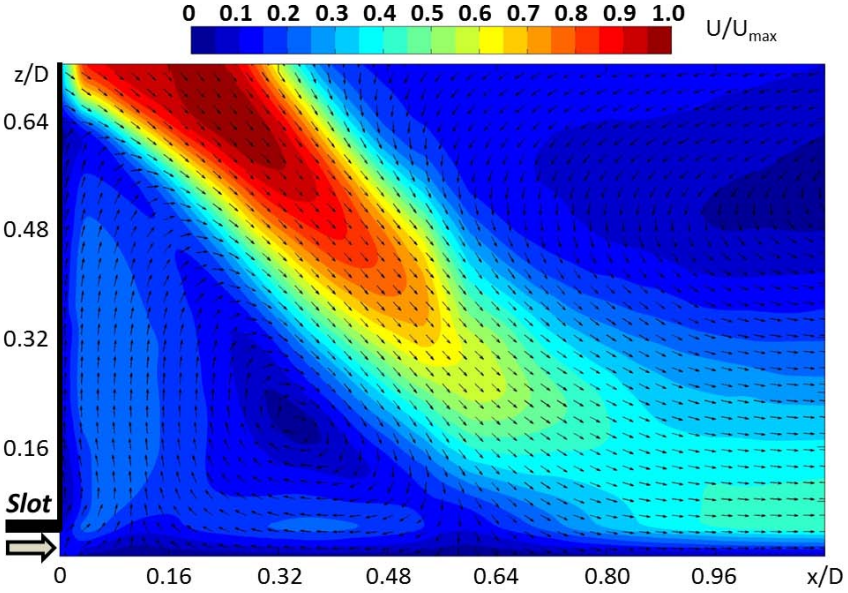

Figure 7.4: Flow field on center plane with slot injection ($W = 3\%$)

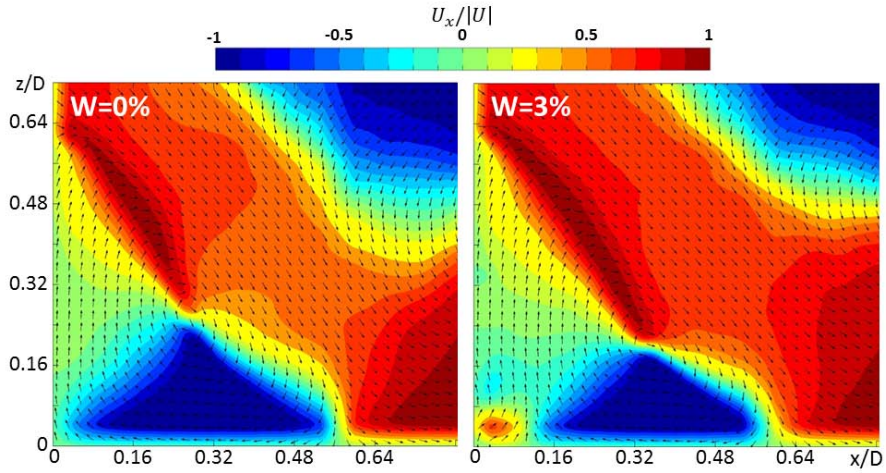

Figure 7.5: Velocity component on streamwise direction (*center plane*): effect of slot injection ($W = 3\%$)

The effect of slot injection can be clearly appreciated on the measurement plane located $4mm$ above the liner (*wall plane*). The vector maps reported in Fig. 7.6 show that the slot generates a region with low velocity immediately downstream the slot exit. The shape of this region is not uniform on lateral direction: the entire test section is affected by a macro flow structure which rotates around the three injectors and tends to direct towards the right side the flow near the test surface, this leads to a to a non uniform flow field near the wall (Cfr. 8.1.2).

In the first part of the wall plane, the slot generally reduces the velocity intensity leaving substantially unchanged the velocity direction, while for $x/D > 0.6$ its effect is negligible.

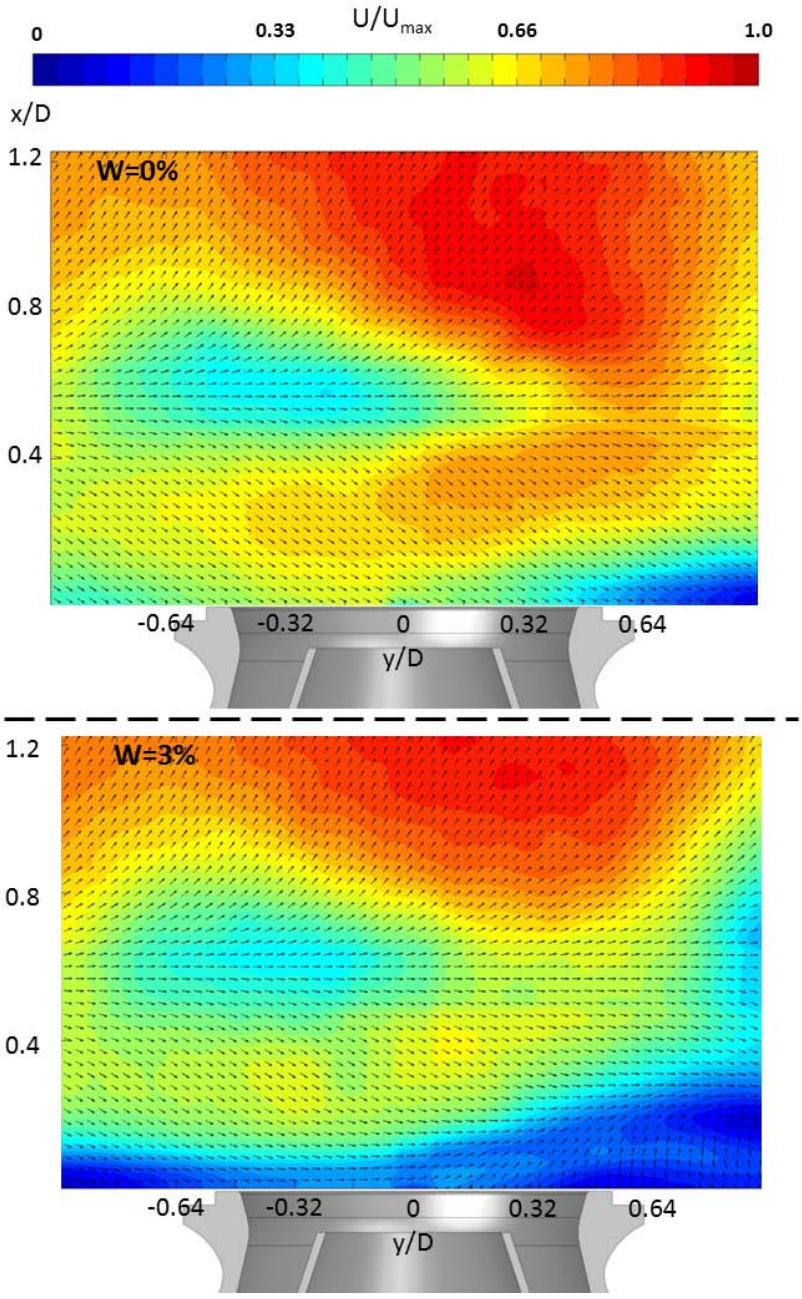

Figure 7.6: Effect of slot injection on wall plane

7.3 Impact of Effusion Cooling Flow

The test configuration equipped with the multi-perforated plate (**LM2** configuration, Tab. 6.2) allows to appreciate the impact of the effusion and slot coolant injections on the flow field. The massive injection of coolant near the wall is expected to have a potential effect on the flow structures especially on the corner vortex. For this reason, the PIV analysis on **LM2** configuration is focussed on the center plane.

In Fig. 7.7 are reported the streamlines on the center plane in the area of the corner vortex setting the pressure drop across the multi-perforated plate at 3%, disabling the slot system and imposing the nominal pressure drop across injectors ($\Delta P/P = 3.5\%$).

The flow field highlights a severe impact of cooling flow especially in the corner vortex region. The streamlines evidence that the characteristic corner RCZ, described for the no coolant condition (Fig. 7.1), is suddenly altered by the effusion injection. Two counter rotating vortices are established un-

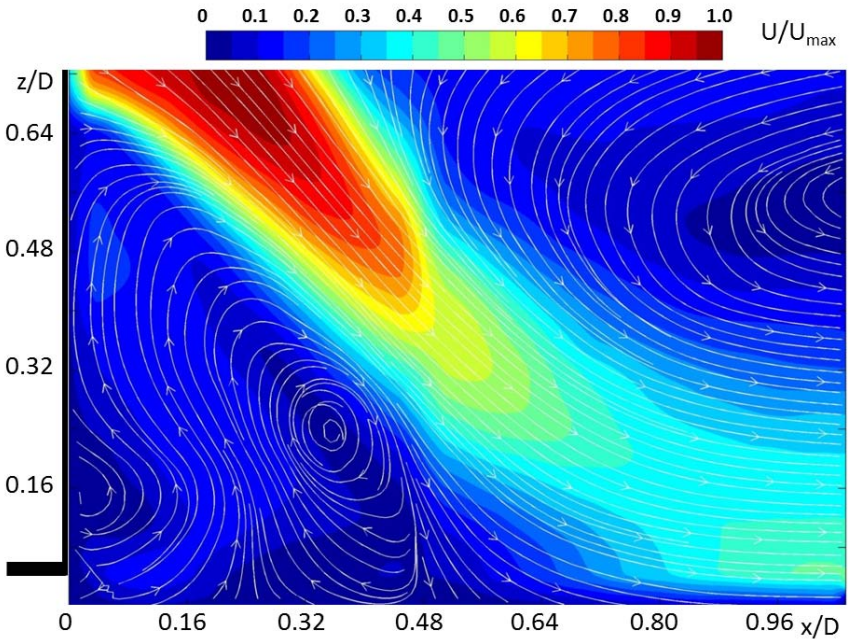

Figure 7.7: Flow field on center plane with effusion injection ($\Delta P/P_{eff} = 3\%$)

der the jet, they generate near the wall positive velocity component in x direction up to $x/D = 0.24$ where streamlines lift up from the liner surface. The vortex located near the slot exit, rotating in anti-clockwise direction, could help to enhance the film protection generated by the slot system. The velocity vector maps with slot injection have shown that the coolant flow exiting from the slot system is early lifted up by the backward recirculating flow compromising its film protection capability.
The spread angle of flow expanding into the test section is much higher than in case with no cooling flow, which results in flow impingement more close to the inlet of combustor ($x/D = 0.48$).

To explore the effect of both effusion and slot cooling on the flow field behaviour, a dedicated PIV survey in the corner region is performed setting the slot mass flow rate at $W = 3\%$ and the effusion pressure drop at 3%. This condition represents a flow setup more close to the engine one.

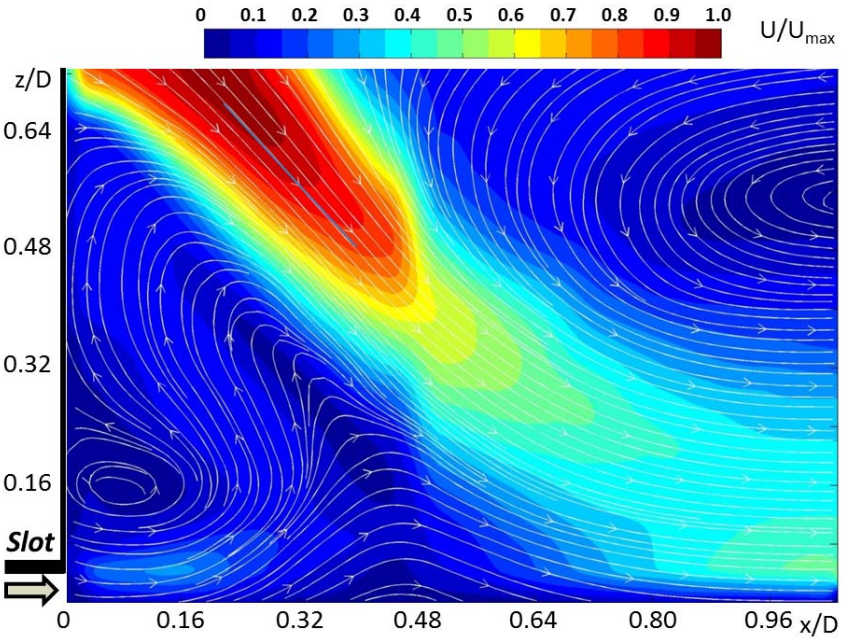

Figure 7.8: Flow field on center plane with effusion and slot injection ($\Delta P/P_{eff} = 3\%$; $W = 3\%$)

As documented in Fig. 7.8, the corner vortex deeply altered by the injection of effusion flow seems to improve the behaviour of the slot coolant. In this case, the slot flow is clearly dragged and energized by the corner vortex structure generating a region with moderated velocity near the wall ($U/U_{max} \approx 0.4$). Moreover, unlike the case with only effusion flow, the slot injection inhibits the development of a region with reverse flow near the wall, despite at $x/D \approx 0.48$ the streamlines tend to lift up from the liner surface. Positive velocity components in x direction near the wall, generated by the mutual interaction of effusion and slot flows, could help the film covering generated by the effusion array; this aspect will be dealt in more details using a dedicated survey carried out for adiabatic effectiveness measurements.
Regarding the jet exit angle, the insertion of the slot flow does not induce appreciable changes respect to the case reported in Fig. 7.7.

Chapter 8

HTC and Adiabatic Effectiveness Experimental Results

Contents

This Chapter deals with the heat transfer and adiabatic effectiveness measurements performed on the Cold Sector Test Rig, according to the test matrix depicted in Tab. 6.2.
The survey will be supported by the flow field measurements illustrated in Chapter 7: the velocity maps will help to understand the thermal behaviour of the different test model configurations.

8.1 Heat Transfer Coefficients

The heat transfer results are presented in terms of Nusselt number augmentation ratio, which is the measured Nusselt number normalized by means of a reference value obtained from the Dittus-Boelter correlation for fully developed and turbulent flow in straight pipe, Eq. 8.1 [6]:

$$Nu_0 = 0.023 \cdot Re_{main}^{0.8} \cdot Pr^{0.33} \tag{8.1}$$

Regarding the space coordinates, as reported for the PIV results, are normalized with the diameter of the injector at the exit into the test section, D.

8.1.1 LM0 Configuration

The first configuration considered in the present survey is the **LM0** setup in which the smooth test plate is used to reproduce the liner wall without slot and effusion flows. The results obtained with this configuration represent the baseline values that will be used to correctly understand the effect of the cooling flow on HTC distributions. Figure 8.2 displays the normalized Nusselt number distribution at different pressure drop across the burners. To asses the effect of main pressure drop, the Nusselt number used to normalize the results is calculated at the nominal condition ($\Delta P/P = 3.5\%$) using Eq. 8.1.

As a general results, the 2D distributions point out the presence of an elliptic area where the heat transfer coefficient reaches the peak values. A slight shift of this area on the right side of the center of the swirler is coherent with the sense of rotation of the three swirlers (Cfr. 8.1.2). As raised up by the PIV results, this zone, located between $x/D = 0.4 - 0.8$, corresponds to the location of stagnation point of the impinging jet and the following strong acceleration of the flow near the wall. Low heat transfer values are registered in the other zone of the test plate, especially in the corner RCZ.

Increasing the main mass flow rate, as expected, the HTC increases as well leaving unchanged the shape of the central region with high heat transfer. To better understand the influence of the swirler pressure drop

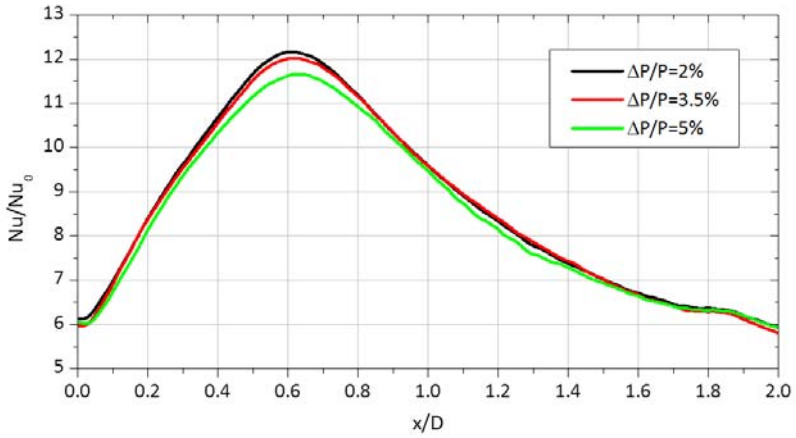

Figure 8.1: Laterally averaged Nusselt augmentation: effect of swirler pressure drop

on the Nusselt distribution, the laterally averaged trends are computed and reported in Fig. 8.1. In this case the values are normalized with a reference Nusselt number evaluated for each of the three tested conditions.

As highlighted by the 2D distributions, the heat transfer coefficient is low at the entrance of the test section but quickly reaches a maximum, after which the magnitude decays slowly. The effect of varying the $\Delta P/P$ on the Nu/Nu_0 is almost negligible except between $0.4 < x/D < 0.8$, around the peak location. In fact, it is possible to observe that an increase of the relative pressure drop leads to a decrease of the normalized Nusselt number peak and its slight shift towards the rig outlet. Moreover, the shear layer and the flow acceleration due to the impingement of the jet and the consequently high turbulence levels resulting in heat transfer coefficients that are substantially higher than those that would be obtained at the same Reynolds number in fully developed pipe flow. These Nu/Nu_0 values, up to 12 in the peak region, are consistent with previous findings reported in the open literature [51, 52, 129]. Summarizing, this plot points out that, far from the peak location, trends obtained at different $\Delta P/P$ are almost coincident: this indicates that the Nusselt number can be roughly scaled with a dependency proportional to $\approx Re_{main}^{0.8}$, being the Prandtl number constant for each test conditions. This relation, as well known, is typical of turbulent flow in duct. On the

other hand, in the area of the maximum Nu the appropriate exponent to reduce data is $\approx Re_{main}^{0.6}$. In this region, as remarked by the PIV survey, the behaviour of the flow field is characterized by the impingement of the burner jet diminishing from the description of turbulent flow in duct. A reduced value of the exponent of the Reynolds number is in agreement with the typical approach adopted for the impingement phenomena [96]. This scaling criteria is of outstanding importance to extrapolate the experimental results to the engine conditions (Cfr. 6.5).

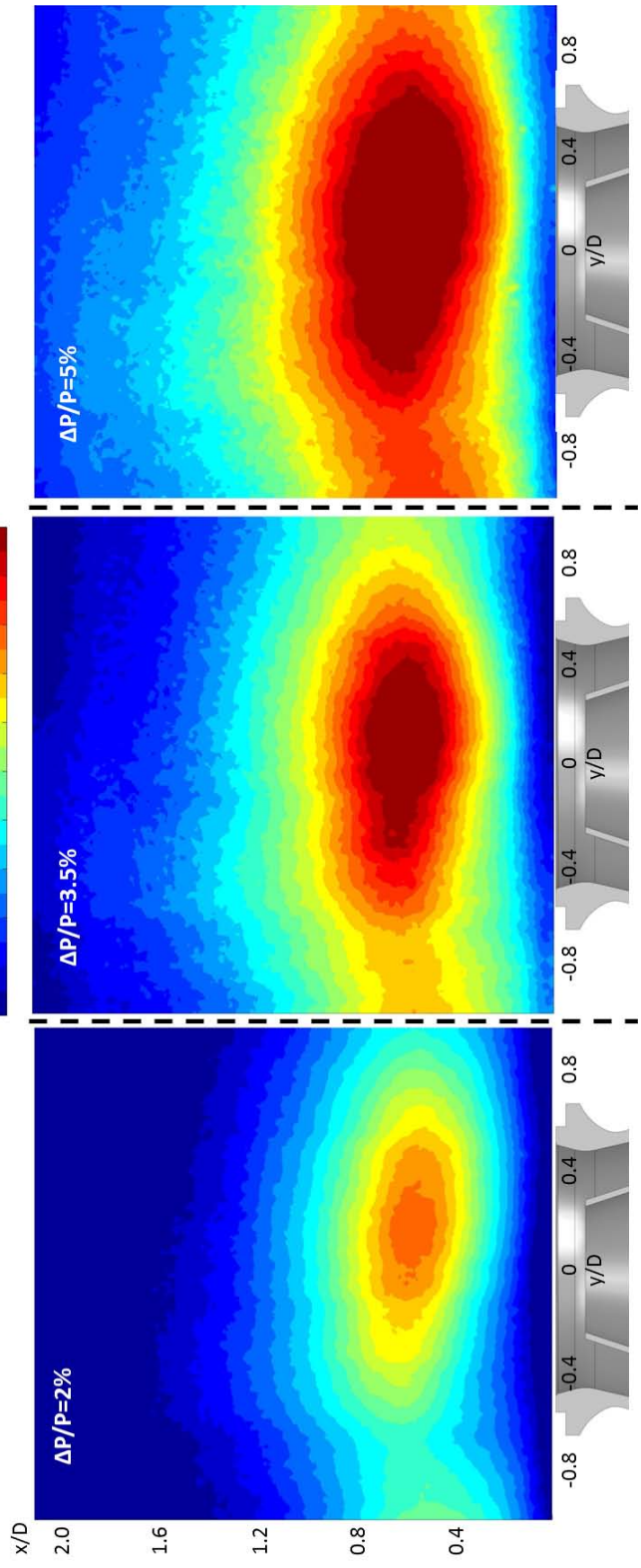

Figure 8.2: Nusselt number distributions for **LM0** configuration: effect of burner pressure drop

8.1.2 LM1 configuration

The **LM1** configuration considers the injection of coolant from the slot realized on the heat shield, at the inlet of the test section (Cfr. 6). The current setup of the test model allows to appreciate the effect of the slot injection on the heat transfer, imposing several values of coolant consumption W.
First of all, let's consider the 2D distributions of Nusselt number, reported in Fig. 8.3, in which the effect of slot injection can be easily caught.

The cooling flow injection moves downstream the impingement region and increases the extension of the low heat transfer area at the slot exit. As a general results, the presence of the coolant causes an overall reduction of the HTC up to $x/D = 1$. Both pictures in Fig. 8.3 highlight a non symmetric distribution of Nusselt number in the proximity of the slot exit, due to a non uniform flow field near the wall: this aspect has been remarked by the PIV measurements performed on the *wall plane* (Fig. 7.6). In fact the entire test

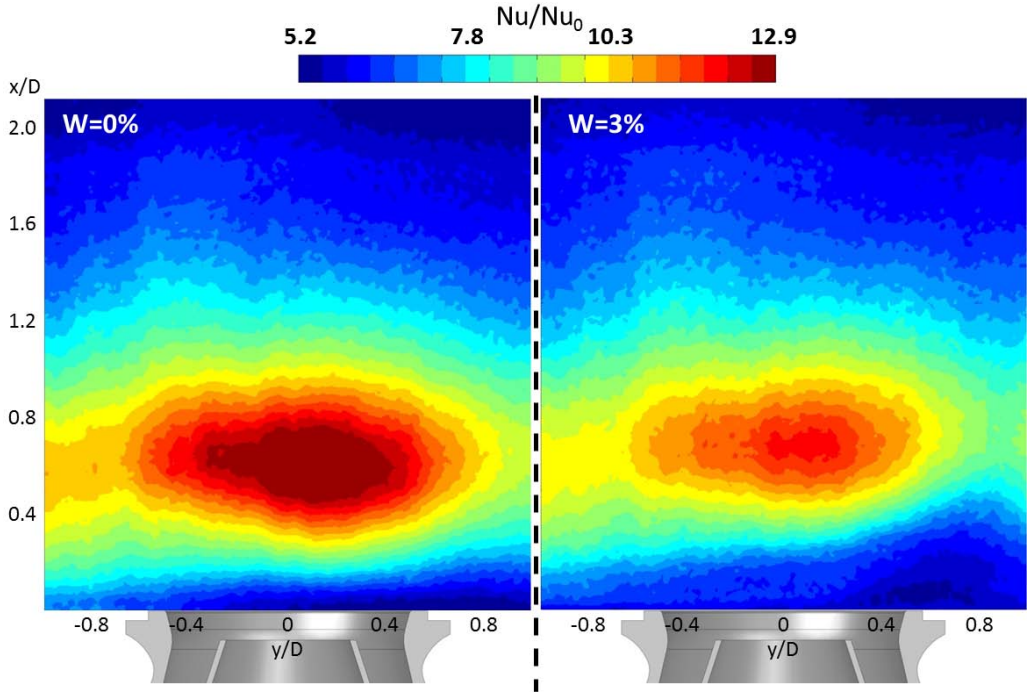

Figure 8.3: Nusselt number distribution: effect of slot injection

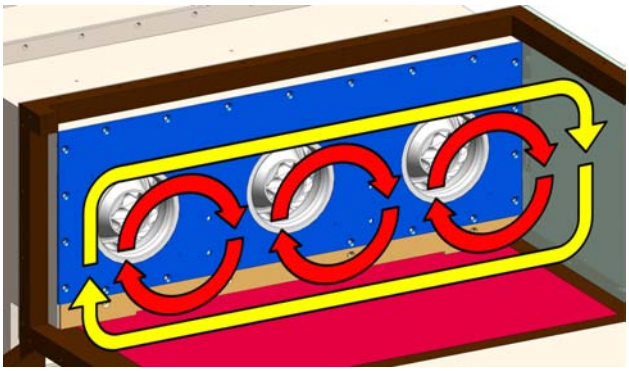

Figure 8.4: Macro recirculation in the test section

section is affected by a macro flow structure which rotates around the three injectors and tends to direct towards the right side the flow near the test surface (towards the left on the opposite side of the test section). The sense of rotation of this macro recirculation is concordant with that impressed to the flow by each swirler; it is worth to notice that three burners are co-rotating (Fig. 8.4).

The laterally averaged trends, depicted in Fig. 8.5, confirm the system behaviour described above: an increase in W inhibits the heat transfer and shifts downstream the peak location. The flow field measurements, illustrated in section 7.2, have already shown a change of position of the jet stagnation point increasing the slot mass flow that drives downstream the burner jet.

Furthermore, after $x/D = 1.2$ the influence of the slot becomes negligible in the range of coolant consumption tested. Once again, the flow field have already highlighted this aspect, confirming a slight effect of coolant injection on the flow field measured on the *wall plane* downstream the peak location.

Fig. 8.5 shows also the $Nu/Nu_{W=0\%}$ curves: these trends show how the HTC is affected by the coolant injection. The maximum relative difference with the $W = 0\%$ case is located upstream the stagnation point, around $x/D = 0.2$, with a reduction of HTC of about 15% for $W = 3\%$. Changing the pressure drop across the burners, the impact of the slot injection on the heat transfer distributions is similar to the case described

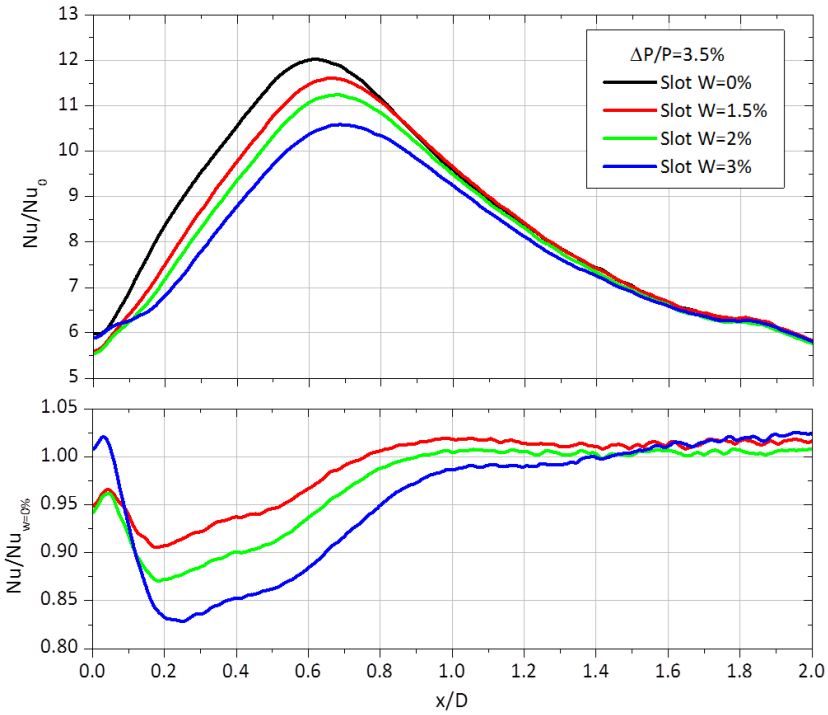

Figure 8.5: Laterally averaged Nusselt augmentation: effect slot injection

above ($\Delta P/P = 3.5\%$).

To summarize the HTC results for the **LM0** and **LM1**, a value of Nu/Nu_0, spatially averaged over the investigated area in front of the central swirler is computed and reported for each tested condition (Fig. 8.6): the Nusselt number augmentation factor is enhanced by either the decrease of the pressure drop and of the slot coolant consumption.

8.1.3 LM2 configuration

The distributed injection of coolant from the effusion array and the mixing with the main flow near the wall is governed by complex and unsteady structures. Respect to the baseline case with no coolant injection (**LM0**), the *HTC* is expected to change with a generally augmentation of the heat transfer. The knowledge of the heat transfer distribution under coolant injection conditions is hence essential to correctly predict the heat load to the

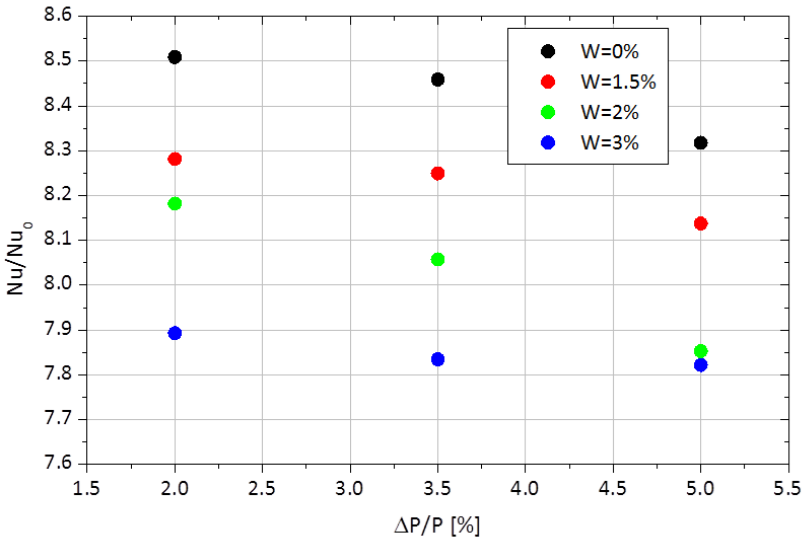

Figure 8.6: Spatially averaged Nusselt augmentation: effect of slot injection

combustion liner in presence of active effusion system. Moreover, results of HTC augmentation factor can be combined with the adiabatic effectiveness values to understand if the cooling system provides a reduction of the heat load on the gas side surface, in addition to the contribution offered by the heat removed trough forced convection inside the perforation.

Fig. 8.11 shows the impact of effusion cooling on the normalized Nusselt number; the main flow is set at nominal condition ($\Delta P/P = 3.5\%$) while the slot is disabled. In presence of the only main flow, the results are in good agreement with those obtained for **LM0** geometry. Even though at the maximum effusion flow rate the distribution exhibits a central region involved by high values of heat transfer coefficient, the injection of coolant produces an overall increase of HTC and provides a more uniform distribution on the whole test plate.

The system behaviour illustrated above is confirmed by the laterally averaged trends displayed in Fig. 8.7: an increase of effusion mass flow promotes the heat transfer and shifts downstream the peak location. Despite an high HTC region can be clearly detected in lateral trends, its relative intensity,

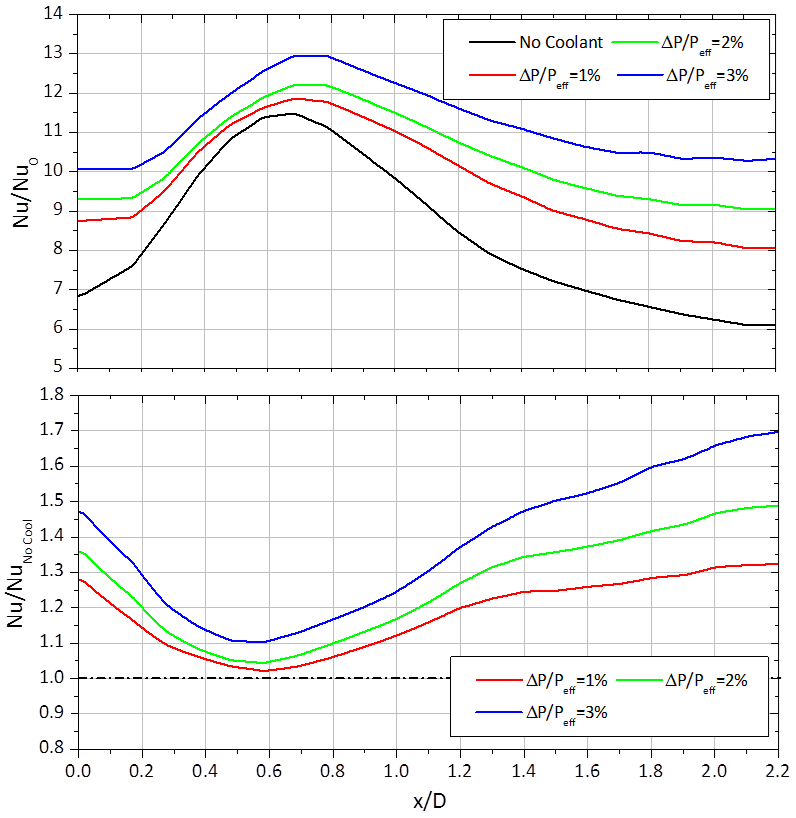

Figure 8.7: Spatially averaged Nusselt augmentation: effect of effusion injection

respect to the heat transfer value registered at the inlet of the test section, is reduced.

To better understand the effect of coolant injection on *HTC* distribution, the spatially average results are also normalized with respect to the condition with no coolant and reported in Fig. 8.7 (bottom). The Nu augmentation factor ($Nu/Nu_{No\,Cool}$) is high at the immediate entrance to the test section but quickly reaches a minimum value, after which the magnitude increases slowly. The lower values are located in the proximity of the stagnation region: here the flow field structures generated by the impingement of the swirler jet and the consequently strong accelerations in the axial direction are predominant with respect to the impact of effusion injection. Moreover, it is expected that in this zone the effective velocity ratio is generally low due

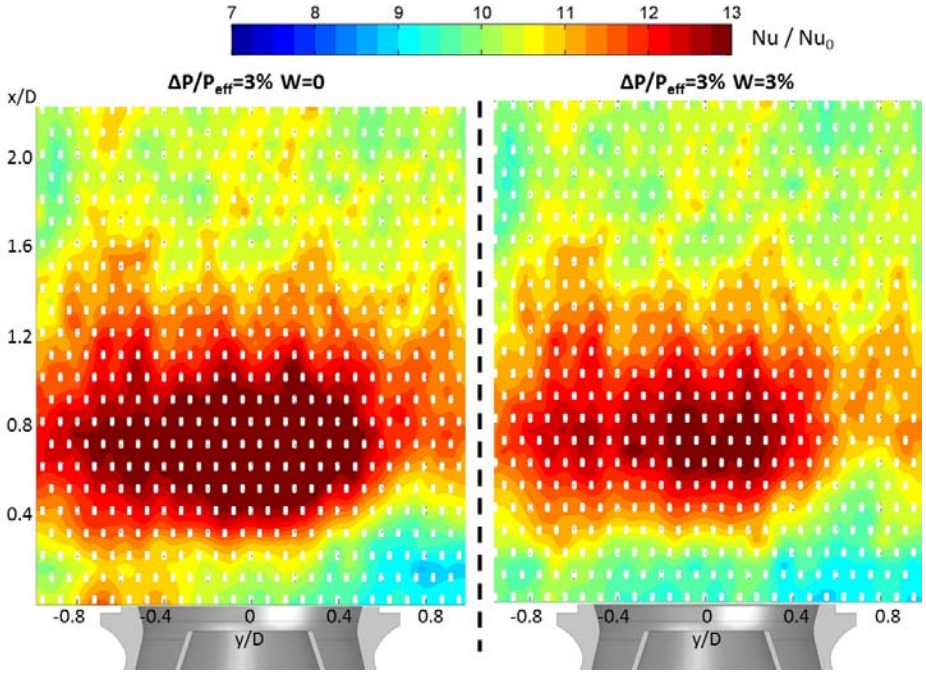

Figure 8.8: Nusselt number distribution: effect of slot and effusion cooling flow

to the high static pressure on the liner surface generated by the stagnation region.

The heat transfer enhancement values registered at the inlet of the liner combined with the expected poor adiabatic effectiveness, in presence of only effusion cooling flow, emphasize the necessity of a slot system to improve the film covering and consequently to reduce the heat load on the external liner surface.

The impact of effusion cooling becomes more intense approaching the test section exit, with the higher values of heat transfer enhancement, close to 1.75, registered for the $\Delta P/P_{eff} = 3\%$ condition. An inflection point can appreciated at $x/D \approx 1.2$ for each flow condition, downstream the 13^{rd} row of effusion holes.

To highlight the effect of the slot injection when the effusion system is activated, the 2D Nusselt number distributions obtained at $\Delta P/P_{eff} = 3\%$ with and without slot injection are compared in Fig. 8.8. A slight effect of

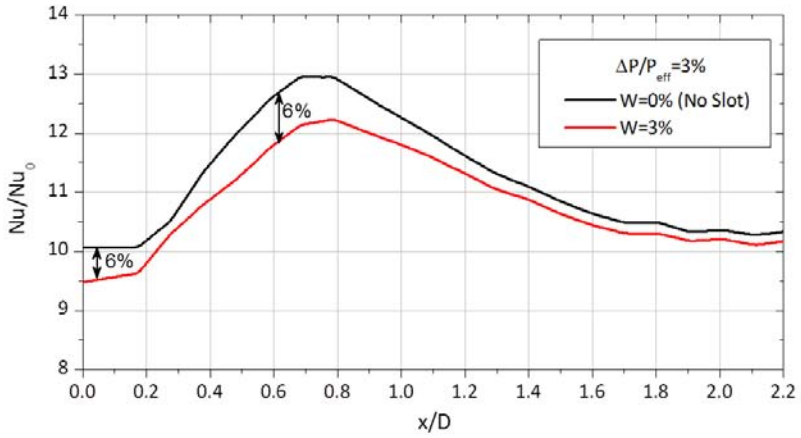

Figure 8.9: Spatially averaged Nusselt augmentation: effect of slot and effusion cooling flow

slot injection is appreciable only in the inlet area of the test section, it inhibits the heat transfer driving downstream the peak location. The laterally averaged trends (Fig. 8.9) confirm the behaviour pointed out with the 2D maps, the main differences in the order of 6% are located at the slot exit and near the peak location; with respect to the **LM1** configuration the impact of slot injection is even more reduced. As expected, thanks to the PIV survey, for $x/D > 1.2$ the impact of slot can be considered negligible.

To support the validity of the survey, a comparison of the results with previous works performed by the research group of the author has been performed. The comparison, carried out in terms of $Nu/Nu_{No\,Cool}$, is aimed at highlight the effect of the effusion injection on heat transfer. In the work of Andreini et al. [57], considered for the comparison, the heat transfer measurements were carried out on a test rig which reproduced, with uniform mainstream conditions (no swirled gas flow), a complete cooling scheme with slot and effusion systems on the liner wall with the same hole perforation tested in the current research.

Starting from the velocity field on the wall plane, reported in Fig. 7.6, and assuming an equal distribution of the cooling mass flow among the effu-

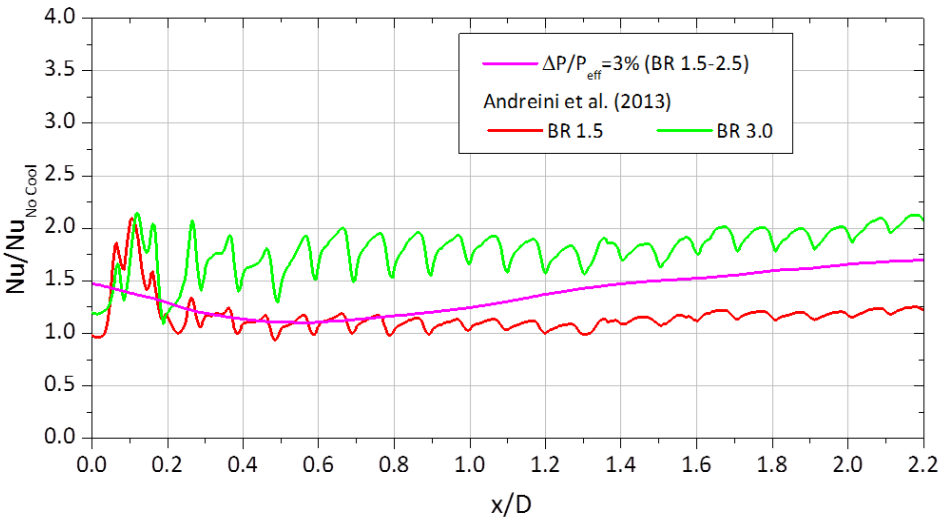

Figure 8.10: Laterally averaged $Nu/Nu_{No\,Cool}$: comparison with results of Andreini et al. [57] (no slot flow)

sion holes, the working blowing ratio for the case $\Delta P/P_{eff} = 3\%$ is estimated to vary approximately in the range $BR = 1.5 - 2.5$. The comparison, reported in Fig. 8.10, shows a good agreement with the literature data and the trend achieved in the current research is bounded by the curve obtained with uniform mainstream conditions by Andreini et al. [57] for $BR = 1.5$ and $BR = 3$ cases. This behaviour suggests that the presence of a swirled flow on the gas side has a little effect on the heat transfer augmentation factor when the Nusselt number is normalized with respect to the no cooling condition.

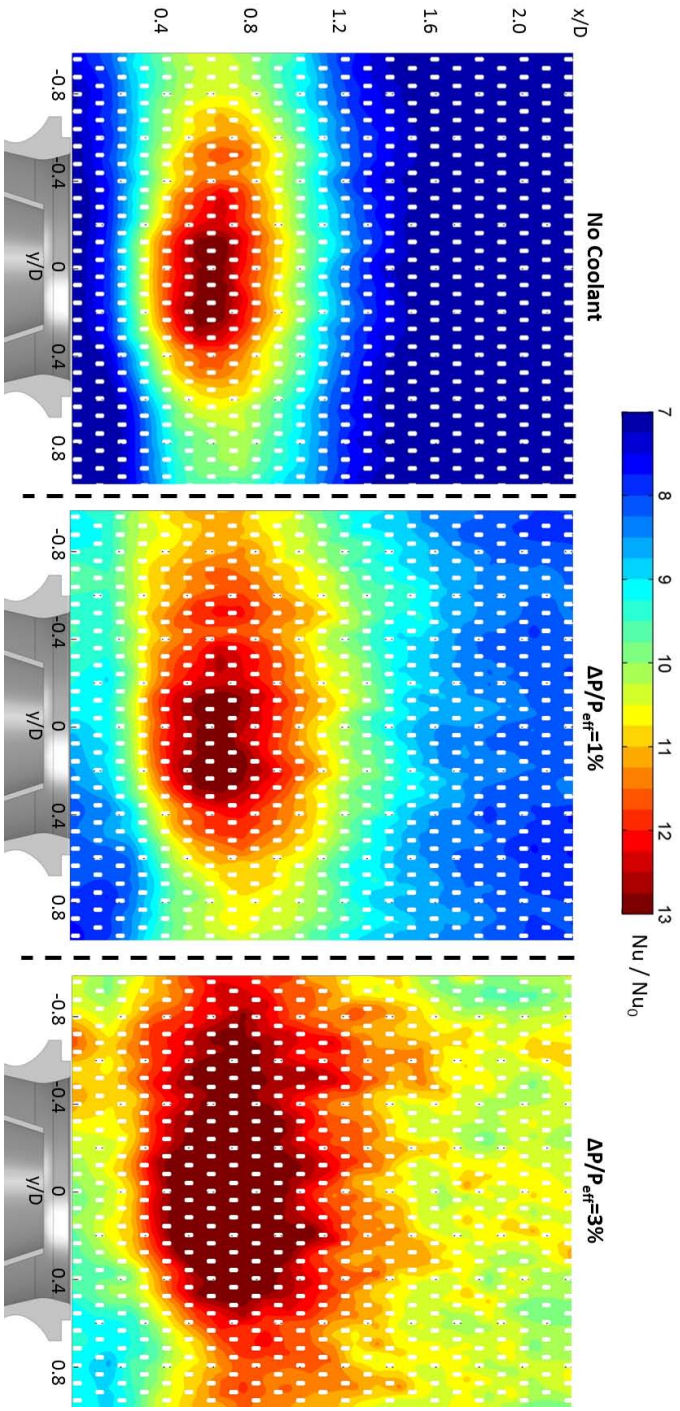

Figure 8.11: Nusselt number distributions for **LM2** configuration: effect of effusion system pressure drop

8.2 Adiabatic Effectiveness

The adiabatic effectiveness tests were carried out on the **LM2** configuration imposing the nominal condition in terms of pressure drop across the burner ($\Delta P/P = 3.5\%$) and varying effusion and slot mass flow rate, in order to appreciate their contribution and effect on film covering. Spatial dimensions are normalized with the axial (S_x) and tangential pitch (S_y) of the hole pattern.

8.2.1 Effect of Effusion Cooling System Pressure Drop

To asses the effect of cooling pressure drop on adiabatic effectiveness, dedicated tests are performed varying the effusion pressure drop, in the range $1\% - 3\%$, and disabling the slot cooling line.

The impact of effusion injection can be appreciated looking at the 2D distributions reported in Fig. 8.15 and using zoomed views on the center line depicted in Fig 8.12. As a general results, the distributions are characterized by a non-symmetric central region with low effectiveness, that corresponds to the zone with high heat transfer values. Here the coolant traces are subjected to a strong lateral spreading, prompted by the unsteady flow structure and by the high turbulence level generated by the impingement of the swirler jet. Moreover, looking at the 6$^{\text{th}}$ row of holes in proximity of the more intensive

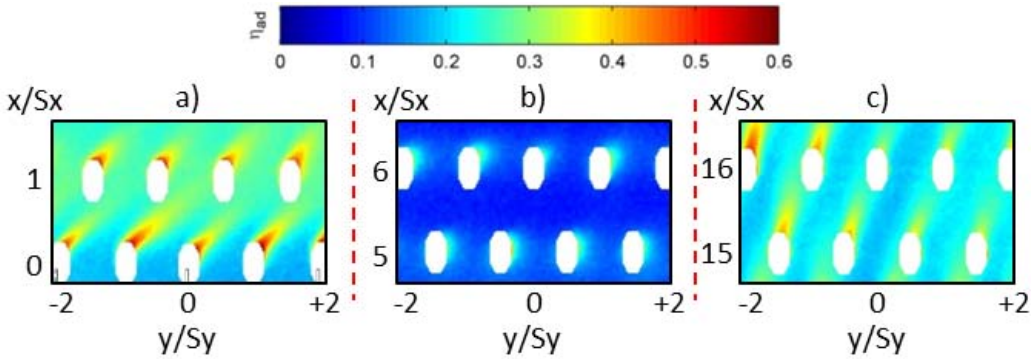

Figure 8.12: Detailed views of adiabatic effectiveness distribution ($\Delta P/P = 3.5\%$; $\Delta P/P_{eff} = 1\%$; no slot cooling)

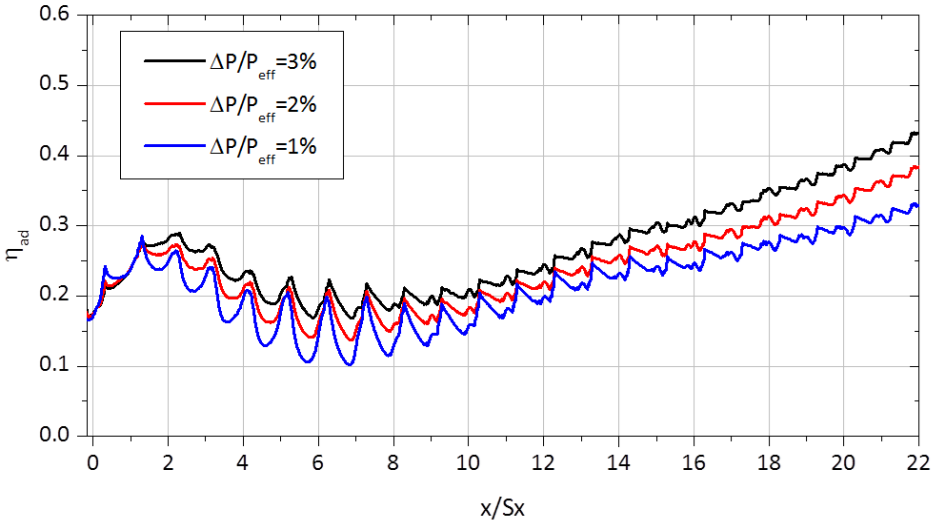

Figure 8.13: Laterally averaged adiabatic effectiveness distribution: effect of effusion pressure drop ($\Delta P/P = 3.5\%$; no slot cooling)

axial acceleration of flow near the wall (Fig. 8.12b), the coolant injection produces very short traces on the right side of the holes exits, and it contributes only to a local spread protection.

Thanks to the flow structure generated in the corner region with positive axial velocity near the wall up to $x/S_x = 3$ (Cfr. 7.3), the cooling flow generates well defined coolant traces deviated towards the right hand side of the test section (Fig. 8.12a). Downstream the fourth row of holes, the coolant is subjected to a rapid mixing with the recirculating main flow: it is first captured and lifted up by the corner vortices, thereafter it is redirected to the liner surface, promoting the film covering especially on the first rows of holes. Thanks to this phenomena, the adiabatic effectiveness starts from a value close to 0.15 for all the coolant conditions.

At the first rows of holes and for $6 < y/Sy < 12$, the 2D distributions highlight a portion of the liner with low effectiveness: here for $6 < y/Sy < 8$ the coolant traces are directed towards the right side of the test section while opposite behaviour is registered for the other holes.

Approaching the exit of the test section, where the main flow field is more

uniform (Cfr. 7), the effectiveness is enhanced by the superposition effects. The coolant traces are here more longer (Fig. 8.12c) and they still presents an appreciable lateral spreading mainly due to the high unsteadiness of the main flow. Starting from the velocity field reported in Fig. 7.6 and assuming an uniform distribution of the cooling flow across the liner perforation, the cooling jets work in this zone at a velocity ratio close to 1.7 and with a compound angle of about 20°.

The lateral averaged adiabatic effectiveness at different effusion pressure drop are reported in Fig. 8.13. The 1D trends highlight the coolant behaviour described by means of 2D distributions. In correspondence of the first row of holes the effectiveness reach values close to 0.17 thanks to the recirculating main flow; moving downstream it first reaches a maximum ($x/S_x = 2$) and then decays rapidly to the minimum values located in the proximity of the jet stagnation region ($x/S_x = 7$). This trend is due to the effect of the corner vortices that destroy the film covering and lift up the effusion flow. For $x/S_x > 10$ the superposition effect helps the film covering and the effectiveness growths almost linearly. The effusion pressure drop supports the film effectiveness on the whole test plate, with the exception of the first two rows of holes where its effect is negligible.

The results in terms of adiabatic effectiveness can be compared with those obtained in the first part of the research on geometry **G1**, which has the hole pattern and spacing close to the multi-perforated plate installed in the Cold Sector Test Rig. The comparison will help to quantify the effect of the swirled gas flow on the film covering at the reference test case of $\Delta P/P_{eff} = 3\%$. The main difficult to perform a proper comparison is the definition of a mean blowing ratio of the test carried out on the CSTR: starting from the velocity field on the wall plane reported in Fig. 7.6 and assuming an equal distribution of the cooling mass flow among the effusion holes a mean gas and coolant velocity have been computed (respectively $\approx 21m/s$ and $\approx 40m/s$); as a result the blowing ratio is close to $BR = 2$ for the case $\Delta P/P_{eff} = 3\%$. Fig. 8.14 reports the comparison in terms of lateral averaged adiabatic effectiveness up to the 18^{th} row of holes. The swirled gas flow deeply affects the effectiveness distribution on the whole test surface; in the first part it

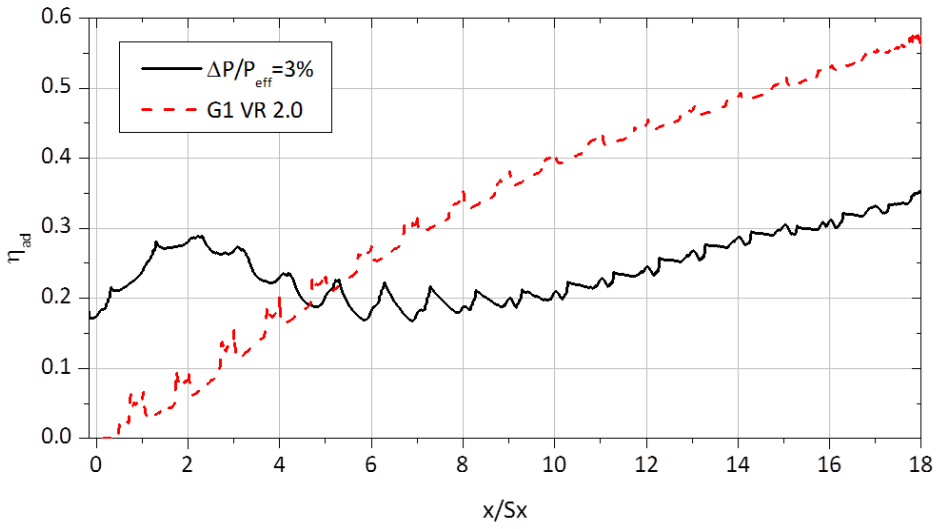

Figure 8.14: Laterally averaged adiabatic effectiveness distribution: comparison with test with uniform mainstream conditions

helps the film covering thanks to recirculating main flow while the case with uniform mainstream conditions presents low effectiveness values. Despite the **G1** test case shows a poor film covering in the first part, it rapidly grows reaching values at the end of the plate well above the effectiveness obtained on the CSTR. Even if the differences between the two proposed test cases are clearly evident, after the 10^{th} row of holes the growth rate of the distributions are almost comparable and the effectiveness increases of $\eta_{ad} = +0.15$ in the last eight rows. This confirms that the results of the first experimental campaign can be used to estimate the film effectiveness only in the last part of the plate where the flow is more uniform.

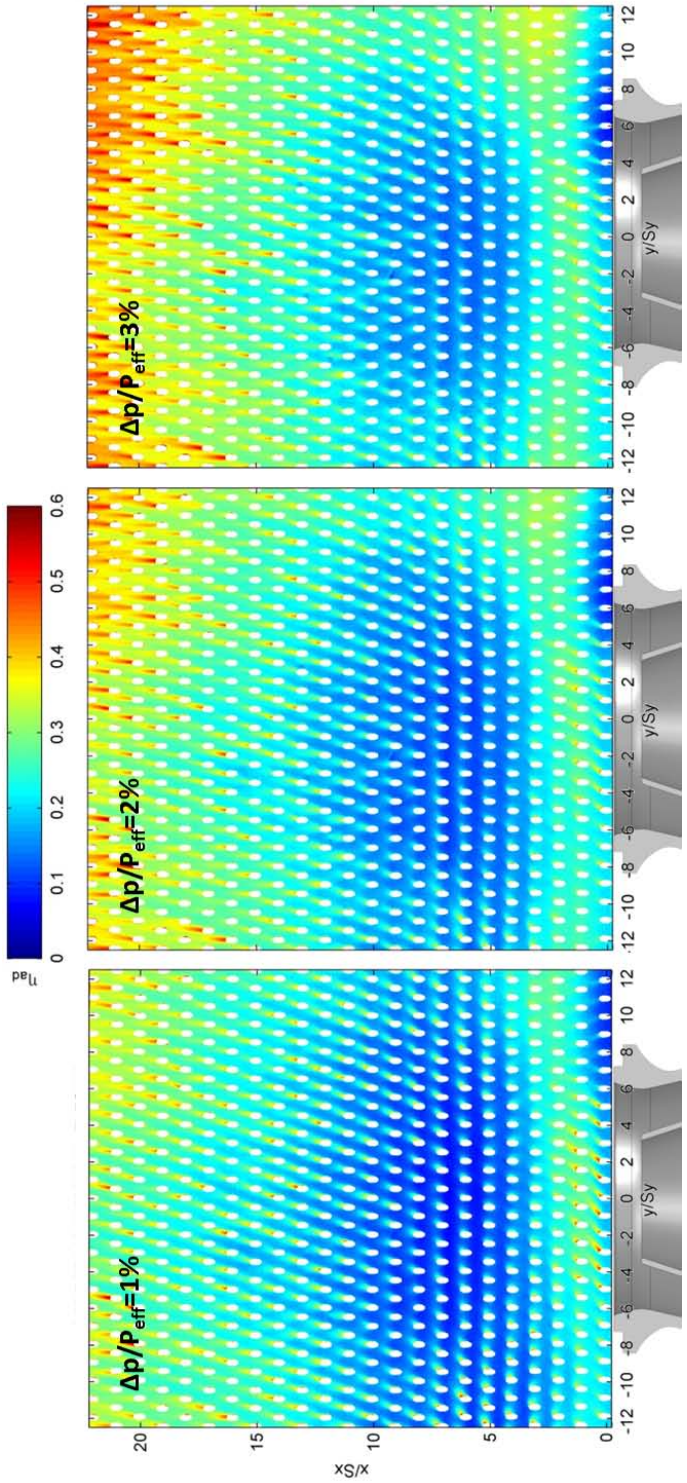

Figure 8.15: Adiabatic effectiveness distribution: effect of effusion system pressure drop ($\Delta P/P = 3.5\%$; no slot cooling)

8.2.2 Effect of Slot Injection

To appreciate the effect of slot injection decoupling the contribution of slot and effusion flow to the adiabatic effectiveness, a novel approach is used exploiting the capability of PSP technique. Two different tests were carried out:

- **Test 1**: the first test is carried out setting the slot and effusion flow at nominal condition and using nitrogen for both the cooling lines.

- **Test 2**: the second test is performed with the same fluid dynamic conditions of the previous test but using N_2 for effusion flow and air for the slot flow rate. The difference between **Test 2** and **Test 1** represents the contribution of the slot system to the film covering.

This method allows effectively to separate the contributions of the two cooling flows to the film effectiveness; classical methods usually deal with this kind of problems testing separately the contribution of the distinct flows. Anyway, as demonstrated by the PIV results, the flow field is heavily influenced by the mutual interaction of slot and effusion flows, especially in the first part of the test plate, making ineffective the classical approach.
Due to the fact that the slot flow, that represents the discharge of the dome cooling system, and the effusion flow have different temperatures in a real liner cooling scheme, the decoupling operation is essential to correctly use the experimental effectiveness results for the design of the liner.

The results of the two aforementioned tests with the experiment with only effusion flow are illustrated in Fig. 8.19 by means of 2D distributions. The slot clearly generates a non-symmetric film distribution in tangential direction: as remarked describing the HTC and PIV results with slot flow, the entire test section is affected by a macro flow structure which rotates around the three injectors and tends to direct towards the right hand side the flow near the liner surface, this leads to a non uniform flow field near the wall (Cfr. Fig. 8.4).

For a more quantitative comparison the lateral averaged effectiveness profiles for the cases illustrated in Fig. 8.19 are computed and reported in

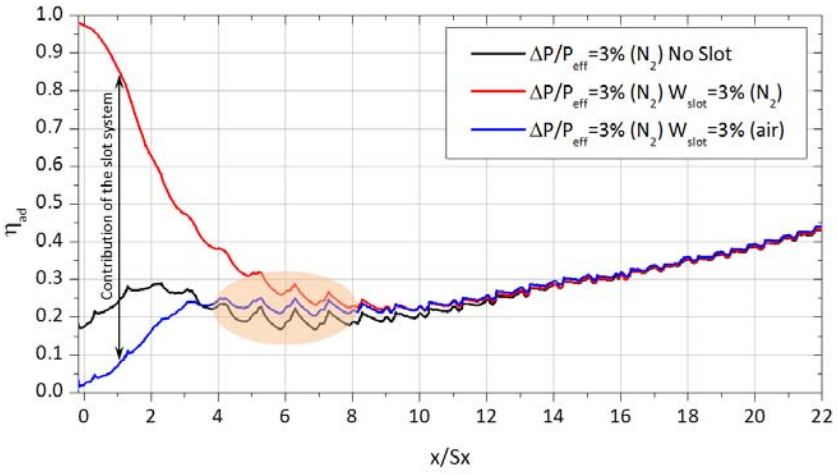

Figure 8.16: Laterally averaged adiabatic effectiveness distribution: effect of slot injection ($\Delta P/P = 3.5\%$)

Fig. 8.16. Up to $x/S_x = 5$ a relevant contribution of the slot can be appreciated: it is represented by the difference between the red and the blue curve. On the other hand for $x/S_x > 10$ the contribution of the slot is practically negligible and the film covering can be described by the test with only effusion injection. In this region the three distributions exhibit the same values, this behaviour confirms that the film protection is generated only by the effusion system and the flow field near the wall is not influenced by the slot. It is interesting to note that in the stagnation region ($4 < x/S_x < 8$), circled in Fig. 8.16, the flow field generated by the interaction of slot and effusion flows improves the behaviour of the film produced by the effusion array. In fact, in this region the effectiveness values marked in blue, which are the contribution of the effusion flow to the film effectiveness in case of both slot and effusion injection, are greater than the values generated disabling the slot system (*black distribution*). This aspect can be explained with the behaviour of the main flow near the liner surface discussed in details in section 7.3: in the corner region, suddenly influenced by the injection of slot and effusion flow, it is no longer possible to recognize a region with reverse flow and the positive axial velocities help the film covering.

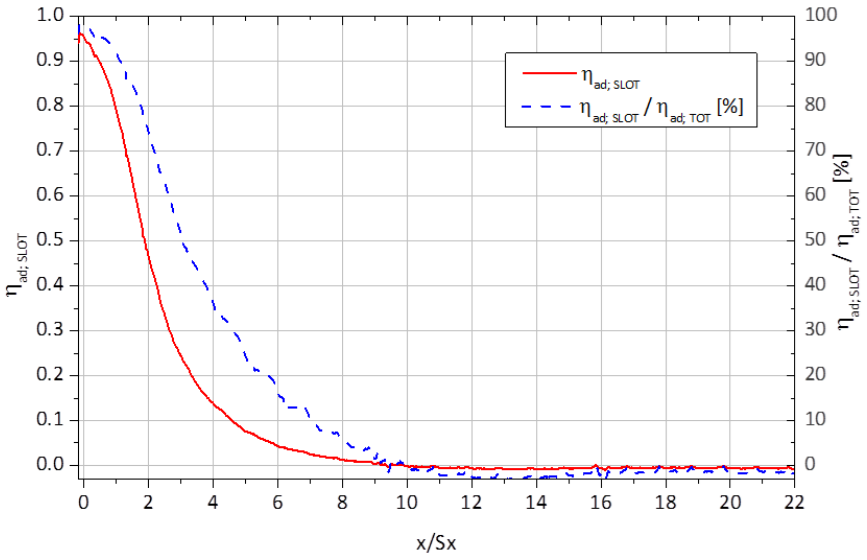

Figure 8.17: Contribution of the slot system to the adiabatic effectiveness ($\Delta P/P = 3.5\%$, $\Delta P/P_{eff} = 3\%$; $W = 3\%$)

On the other hand up to $x/S_x = 1$ (i.e. the first two rows) the contribution of effusion flow (blue curve) is very low, with values below 0.1, and the protection is mainly driven by the slot system that produces a superimposed flow with high efficiency.
To summarize the behaviour of the slot, its contribution to the adiabatic effectiveness has been extracted from the effectiveness profiles of Fig. 8.16 and reported in Fig. 8.17 as $\eta_{ad;SLOT}$ values and in percentage of the total effectiveness; $\eta_{ad;SLOT}/\eta_{ad;TOT}$.

Thanks to the high definition of the results, four efficiency profiles are extracted at different x/S_x values on lateral direction, they help to deepen the explanation of film behaviour pointing out the effect of slot and effusion flow (Fig. 8.20).

Downstream the second rows of holes ($x/S_x = 1.5$, Fig. 8.20(a)), the behaviour that stood out against the other one is the profile obtained in case of slot injection. A non uniform distribution on the lateral direction can be appreciated with a minimum for $y/S_y = -6$, here the slot flow is subjected to a

strong interaction with the mainstream flow and starting from $\eta_{ad} \approx 1$, close to the slot exit, the protection decays rapidly in the axial direction reaching value of 0.5 just downstream the second rows of holes. On the other hand at $y/S_y = 9$ are necessary about 6 rows to reach the same film protection. Regarding the case with only effusion flow, the holes injection generates a more uniform film covering with constant value close to $\eta_{ad} = 0.3$.

Moving downstream ($x/S_x = 5.5$, Fig. 8.20(b)), the slot still produces a non uniform effectiveness profile on lateral direction; moreover, as discussed before, on the right hand side of the test model ($y/S_y > 0$) the covering offered by the effusion flow is improved by the flow field generated when the slot system is activated.

Approaching the exit of the test section ($x/S_x = 10.5 - 20.5$, Fig. 8.20(c); 8.20(d)), the flow protection is clearly more uniform in lateral direction and the effect of slot injection is not more recognizable.

To highlight the strong effect of the swirled flow field on the adiabatic effectiveness, in Fig. 8.18 the results, achieved on the Cold Sector Test Rig with effusion and slot cooling systems activated, are compared with the trend obtained by the author downline of the work performed to tune the PSP technique during the Ph.D. course [98]. Measurements of adiabatic effectiveness were performed on a test article replicating a combustor cooling system composed by a slot system and an effusion array with the same perforation of the pattern included in the CSTR. Unlike the CSTR, the test model considered by the author in [98] provided uniform flow conditions on the gas side (no swirled flow): a detailed description of the test rig can be also found in the works of Andreini et al. [57], Facchini et al. [111] and Ceccherini et al. [130].

The test condition chosen to compare the results obtained on the CSTR has a Blowing Rate of the effusion array of $BR = 1.5$ which is, as already discussed, a mean value representative of the condition $\Delta P/P_{eff} = 3\%$ and the slot system is activated at a test point close to the one investigated in present research activity.

From the comparison (Fig. 8.18), it is clear the impact of the swirled gas flow and the effect of the interactions with the liner wall on the film covering.

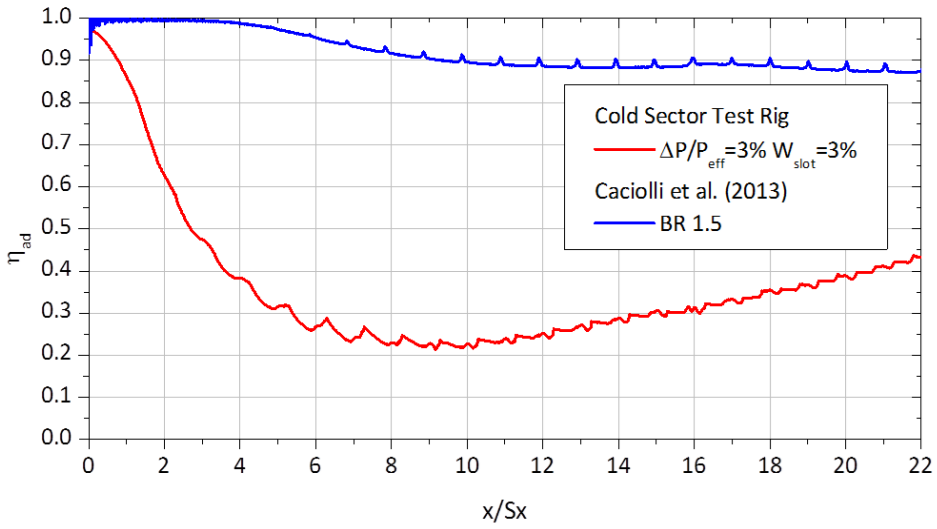

Figure 8.18: Laterally averaged adiabatic effectiveness: comparison with results obtained downline of the work of Caciolli et al. [98]

In case of uniform conditions on the gas side (blue curve), the slot flow and the effusion array keep the effectiveness close to $\eta_{ad} = 0.9$ on the whole test plate. In addition, the slot clearly contributes to an evident high effectiveness core region at the first rows of holes. On the other hand for the test case with representative gas conditions (red curve), the film covering is subjected to a rapid deterioration, showing values well below the trend obtained by the author in Caciolli et al. [98].

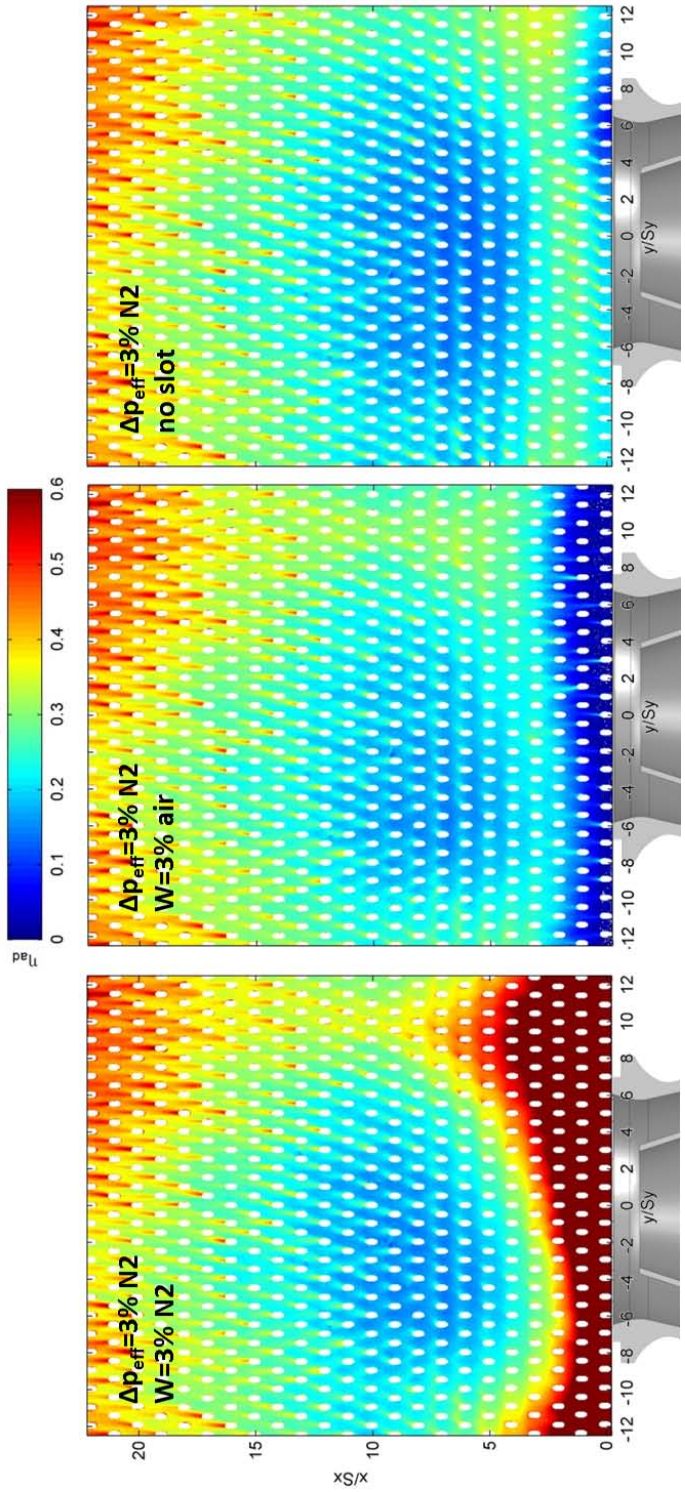

Figure 8.19: Adiabatic effectiveness distribution: effect of slot injection ($\Delta P/P = 3.5\%$)

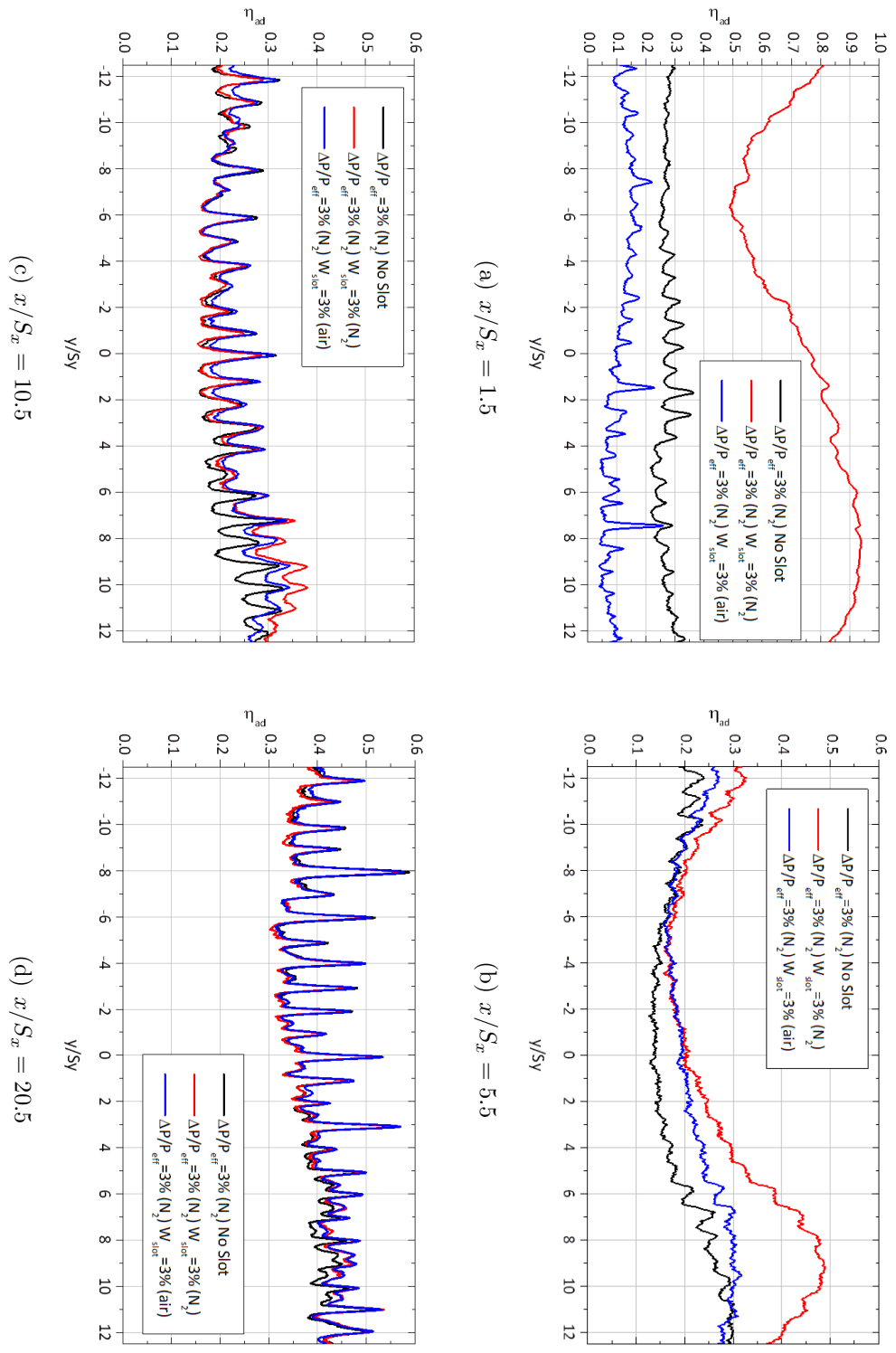

(a) $x/S_x = 1.5$ (b) $x/S_x = 5.5$

(c) $x/S_x = 10.5$ (d) $x/S_x = 20.5$

Figure 8.20: Adiabatic Effectiveness profiles

8.3 Net Heat Flux Reduction

A powerful parameter to summarize the impact of effusion cooling system on HTC and adiabatic effectiveness is the Net Heat Flux Reduction, $NHFR$, Eq. 8.2 (Cfr. 2):

$$NHFR = 1 - \frac{\dot{q}}{\dot{q}_0} = 1 - \frac{HTC_{main}}{HTC_{main;\,0}} \left(1 - \eta_{ad} \cdot \theta\right) \tag{8.2}$$

$NHFR$ is a commonly used parameter to evaluate the reduction of heat flux across the external cooled surface with respect of the baseline situation, one of the goal of the effusion systems is to increase the NHFR as much as possible. It is worth to notice that, in presence of high radiation the $NFHR$ parameter is not representative of the reduction of heat load to the liner surface. In addition, it can not be used as performing parameter comparing different effusion arrangement because it does not take into account the contribution of heat sink effect which plays a significant role in lowering the liner temperature. In the present study the dimensionless temperature θ, necessary to estimate the $NHFR$, has been calculated using temperature values representative of a combustor, obtaining $\theta = 1.2$.

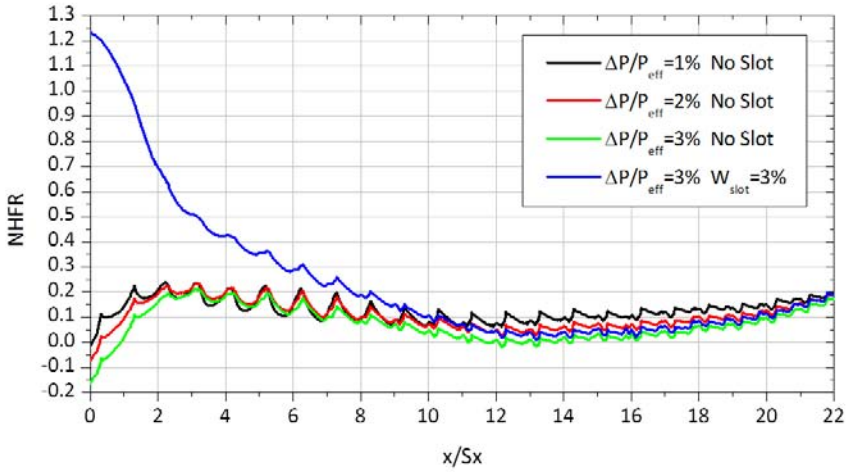

Figure 8.21: Net heat flux reduction ($\Delta P/P = 3.5\%$)

Combining the results in terms of film covering (Cfr. 8.2) and heat transfer augmentation factor (Cfr. 8.1), the lateral averaged trends of $NHFR$ have been computed and reported in Fig. 8.21.

Starting from the conditions without slot injection, the effect of effusion pressure drop seems to be generally negligible except for the entrance region ($x/S_x < 2$) and the zone $13 < x/S_x < 18$. Here, despite the effusion pressure drop is able to enhance the film covering, the increase of adiabatic effectiveness is not sufficient to compensate the increase of the heat transfer coefficient on the liner surface resulting in a reduction of $NHFR$ parameter moving from $\Delta P/P_{eff} = 1\%$ to $\Delta P/P_{eff} = 3\%$.

The benefits achieved by the use of a slot system to start the film covering at the inlet of the combustor is clearly summarized in the $NHFR$ trend. Values greater than 1 are reached in the first part of the liner where the cases with only effusion flow exhibit an augmentation of surface heat load ($NHFR < 1$). Here, the product of η_{ad} and the dimensionless temperature θ is greater than 1; this means that an increase of the heat transfer coefficient, with respect to the baseline value, has positive effects: the slot injection not only produces a covering of the surface but more importantly it colds down the liner.

A minimum value for all the test conditions is located at $x/S_x = 13$ at the end of the low effectiveness and high heat transfer region where the HTC/HTC_0 distributions have an inflection point and, downstream, the growth rate of the heat transfer augmentation factor is slight reduced (Fig. 8.7).

8.4 Concluding Remarks

The results of the experimental campaign, analysed in details in the previous sections, have allowed to reach the objectives of the survey measuring the effusion performances under representative/swirled mainstream conditions. The extensive PIV survey showed that the flow field, generated inside the test rig, can be considered representative of a lean combustor replicating all the characteristic flow structures. Moreover, the main similarity parameters of the cooling system were replicated during the experiments. For these reasons, the results in terms of adiabatic effectiveness and heat transfer coefficient can be scaled to engine conditions with sufficient accuracy to support the design of the cooling system (Cfr. 6.3). With respect to the experimental campaign reported in the first part of the work, that has a Technology Readiness Level (TRL) of about 2, the results achieved on the Cold Sector Test Rig enhance the level up to 4.

At the end of the experimental campaign some words need to be spent about the performance of cooling system, proposing indications to optimize it. In the first part of the liner, it is clear that the slot system can be deeply improved in order to achieve a more uniform film covering on lateral direction. One of the possible way to achieve this object is to perform a 2D contouring of the slot exit, increasing the height of the slot where it produces effectiveness profiles that decay rapidly in axial direction. It is worth to notice that the $NHFR$ distributions have highlighted the capability of a well designed slot system to obtain a significant reduction of surface heat load. Thanks to the performance of the slot system, in the first part of the liner the porosity of the effusion pattern could be reduced saving coolant for other zones of the liner. Other possible improvement solutions for the slot system are the introduction of an extended slot lip up to the jet stagnation region or the design of an heat shield with inclined lip near the slot exit. This last solution has been already tested and discussed in literature by Wurm et al. [82]: they showed that an improvement of the film effectiveness can be achieved acting on the inclination angle of the lip (Fig. 8.22). However, it

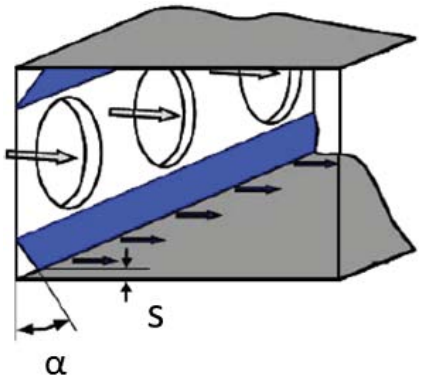

Figure 8.22: Scheme of heat shield with inclined lip [82]

should be remembered that a different shape of the heat shield could have an impact on gas flow field, especially in the corner region.

The central part of the liner can be considered a critical region from a thermal point of view: it is characterized by a region with high external heat load sustained by high values of HTC. An improvement of the liner design must take into account this critical zone proposing solutions able to keep low the temperature of the component. Since the film covering generated by the effusion array seems to be strongly deteriorated by the impinging gas flow and the slot flow does not reach this region, a feasible solution to increase the efficiency of the system could be aimed at enhancing the heat sink effect, for example increasing the perforation porosity leaving the same hole diameter, or enhancing the heat transfer on the cold side. It is worth to notice that the porosity of the effusion pattern has also positive consequences on the heat transfer on the annulus side [118].

Finally, the overall thermal performance of the last part of the liner could be improved using the solutions discussed in details in section 5.9 treasuring the results of the first experimental campaign. Double wall solutions or effusion liner with turbulators on the annulus side (Fig. 5.23) can deeply help to lower the wall temperature approaching the exit of combustor without increasing the coolant consumption.

Per correr miglior acque alza le vele
omai la navicella del mio ingegno,
che lascia dietro a sé mar sí crudele

Dante Alighieri, Divina Commedia (Purgatorio, Canto I)

Conclusions

The present work collects a large part of the activities performed during the Ph.D. course on the topic of liner cooling system. Conclusions of the present investigation are now drawn, trying to trace a brief outline of the performed study, focussing on main achievements as well as discussing which aspects would be studied in further investigations.

Present research activity dealt with two experimental campaigns on effusion cooling schemes designed for aero-engine combustor liner applications. Effusion cooling is a very efficient cooling strategy based on the use of multi-perforated liners, where metal temperature is lowered by the combined protective effect of coolant film and heat removal through forced convection inside each hole. Beyond that, multi-perforated liners act also as passive devices to mitigate thermoacoustic phenomena. Effusion systems represents the current state-of-art of liner cooling technology for lean burn swirl stabilized combustor architectures.

The work aimed at deepening the knowledge of effusion systems from a thermal point of view. In the first part, seven multi-perforated planar test plates, which represent portions of liner geometries, were tested in terms of adiabatic effectiveness distributions and local values of overall effectiveness, imposing several working conditions. The survey allowed to explore the impact of the main geometrical and fluid dynamics parameters, including the effect of density ratio, on thermal performance.

To enhance the TRL (Technology Readiness Level) of the first analysis, a planar sector test rig, equipped with three AVIO Aero PERM (Partially Evaporated and Rapid Mixing) injector systems and working at atmospheric conditions, was considered in the second part of the work, performing heat

transfer coefficient and adiabatic effectiveness measurements. The test rig allowed to reproduce a representative flow field on the gas side and to test the complete liner cooling scheme composed by a slot system, that reproduced the exhaust dome cooling mass flow, and an effusion array on liner wall.

Detailed bidimensional maps of heat transfer coefficient have been obtained with a steady-state technique, using TLC (Thermochromic Liquid Crystals) in a wide band formulation; while adiabatic effectiveness distributions have been estimated using the PSP (Pressure Sensitive Paint) technique, developed and tuned by the author within the Ph.D. course. The PSP technique was proved to be the superior steady state method to estimate adiabatic film cooling distributions. Pressure sensitive paint capability is due to the use of heat and mass transfer analogy, which allows to avoid problems associated with the heat transfer methods. In flow conditions which satisfy the hypothesis of the analogy, this method allows to reproduce a real adiabatic experiments, thus the results are estimated directly from data acquisition without any correction in the data post-processing.
Local values of overall effectiveness has been measured through steady state conductive tests using thermocouples embedded in the test samples. Regarding the flow field generated by the PERM injectors, it has been investigated by a 2D PIV (Particle Image Velocimetry) analysis performed on several measurements planes focussing on the near wall effects and coolant/mainstream interactions.

As far as the tests with uniform mainstream conditions are concerned, the effect of free-stream turbulence on film cooling was investigated on a reference geometry with two different level of turbulence ($Tu = 1.5\%$ and 17%). In the penetration regime, the augmentation of mixing and lateral spreading of the jet due to an higher turbulence level improved the wall film protection.

The comparison of geometries with different hole inclination showed that for low blowing ratio the geometry with tilted holes had a best wall protection. On the other hand for high blowing ratios the normal hole array provided a slightly better overall effectiveness. This behaviour was ascribable to the low mainstream heat transfer coefficient augmentation and to

the higher, with respect to the configurations with slant-hole injection, heat transfer coefficient inside hole due to the entrance effects.

A reduced effect of hole spacing pattern variation, when changing the value of S_x/S_y from 1.24 to 1.93 and keeping constant all the remaining geometric features, was observed. The impact on the η_{ov} results is roughly 2% at $BR = 5$.

The results have shown the influence of density ratio on adiabatic effectiveness distributions: this parameter has a strong impact on film protection especially at BR between mixing and penetration regime, where it influences the lateral spreading of the coolant jets and their capability to remain attached to the wall. Nevertheless, in full penetration regime ($BR > 2$) measurements indicated that the effect of density ratio vanishes.

A data reduction strategy was carried out for the tilted geometries, in order to point out the thermal performances normalizing the weight of coolant consumption. It suggested a possible optimization strategy, working with an higher porosity than the usual range required for the cooling and a lower blowing ratio to guarantee the correct air-split in the combustion chamber. Beyond that the parameter l/d, actually fixed by manufacturer capabilities, has a beneficial impact on cooling performance. The proposed design guideline seems to be promising also from the acoustic damping requirements.

With respect to the measurements performed with swirled mainstream conditions, the PIV measurements highlighted a flow field in the combustion chamber characterized by an expanding swirled flow with high momentum jets that impinge on the liner surface and generate a large central recirculation zone and a corner vortex. The impingement area was characterized by flow unsteadiness, shear layer and strong gradient of axial velocity. The injection of coolant deeply altered the corner vortex region, the insertion of effusion cooling flow produced a vortex structure under the swirler jet that helps the film covering generated by the slot system; moreover, when both effusion and slot systems were activated it was not possible to recognize negative axial velocity components near the wall.

Concerning the heat transfer measurements, laterally averaged distribu-

tions have pointed out that the HTC is low at the entrance of the test section but quickly reaches a maximum value, after which it slowly decays. Distributions and 1D trends of heat transfer coefficient have shown that the presence of slot injection inhibits the heat transfer; while, as expected, opposite behaviour was reported in case of effusion injection. The impact of effusion flow on HTC distributions was more pronounced at the inlet and at the outlet of the test section. On the other hand, in the stagnation region the heat transfer was driven by impingement phenomena and a reduced effect of cooling injection was reported.

Regarding the adiabatic effectiveness results, 2D maps have pointed out a central region with low effectiveness, that corresponded to the area with high heat transfer coefficient. Downstream this zone, thanks to the superposition effect, the effectiveness grew almost linearly supported by the pressure drop across the perforation. The slot system produced a non uniform protection on lateral direction, its effect was relevant up to $x/S_x = 5$ while downstream it was practically negligible. Despite the slot effectiveness decayed rapidly in axial direction, it was an effective method to reduce the surface heat load as raised up by the $NHFR$ trends.

The analysis of the experimental results, considering also the finding of the first part of the current research, has suggested possible optimizations of the cooling system. A contouring of the slot exit could help the film protection, while coolant flow could be saved reducing the porosity of the first rows of holes. Other possible improvement solutions for the slot system are the introduction of an extended slot lip up to the jet stagnation region or the design of an heat shield with inclined lip near the slot exit.
The central part of the liner is characterized by a region with high heat flux where the film covering seems to be strongly deteriorated by the impinging gas flow. A feasible solution to lower the metal temperature could be aimed at enhancing the heat sink effect or the heat transfer on the cold side. The heat sink effect can be easily improved increasing the perforation porosity leaving the same hole diameter. Finally, the thermal behaviour of the portion of the liner close to the test section exit could be improved, treasuring the findings of the first part of the research, by means of different solutions

such as double wall with impingement on the cold side or liner with turbulator on the annulus side.

Effusion cooling is undoubtedly an excellent technique to protect liner of low-NOx combustor chambers, as it allows to meet the requirements of an high efficiency cooling scheme with a reduced cooling air consumption. Nevertheless the research has raised aspects and proposed new cooling solutions that require further investigations. First of all, perforation with normal holes, as they meet most of the industrial requirements in terms of simplicity and cost, must be tested in experimental apparatus with representative mainstream conditions on the gas side to get a proper comparison with tilted arrays. Moreover, new test campaigns should be set up to study the thermal effectiveness of the proposed cooling scheme based on a double wall configuration or multi-perforated liner with turbulator on the cold side, optimized porosity distribution of the effusion perforation and innovative solutions of slot system. These new experimental survey will allow to perform an adequate comparison with the current engine configuration, tested in second part of the research, and to asses benefits in term of thermal performance.

List of Figures

List of Tables

Bibliography

[1] Intemational Civil Aviation Organization. Outlook for air transport to the year 2003. *ICAO Circular 252- ATI103*, 1995.

[2] Advisory Council for Aeronautical Research in Europe. Strategic research agenda. Technical report, ACARE, 2000.

[3] G. Wilfert, J. Sieber, A. Rolt, N. Baker, A. Touyeras, and S. Colantuoni. New environmental friendly aero engine core concepts. *Proceedings of the 18th ISABE conference*, ISABE-2007(1120), 2007.

[4] Y. Zeldovich, D. Frank-Kamenetskii, and P. Sadovnikov. *Oxidation of Nitrogen in Combustion*. Publ. House of the Acad of Sciences of USSR, 1947.

[5] S. M. Correa. A review of nox formation under gas-turbine combustion conditions. *Combustion Science and Technology*, 87(1-6):329–362, 1993. doi: 10.1080/00102209208947221.

[6] A. H. Lefebvre. *Gas Turbine Combustion*. Taylor & Francis, 1998.

[7] A.M. Mellor. *Design of modern turbine combustors*. Combustion treatise. Academic Press, 1990. ISBN 9780124900554.

[8] S.A. Mosier and R.M. Pierce. Advanced combustion systems for stationary gas turbine engines. Technical Report Final Report FR-11405, U.S. Environmental Protection Agency, 1980.

[9] Y. Huang and V. Yang. Dynamics and stability of lean-premixed swirl-stabilized combustion. *Progress in Energy and Combustion Science*, 35 (4):293–364, 2009. ISSN 0360-1285.

[10] C. L. Ford, J. F. Carrotte, and A. D. Walker. The impact of compressor exit conditions on fuel injector flows. *Journal of Engineering for Gas Turbines and Power*, 134:111504–111504, 2012. doi: 10.1115/1.4007025.

[11] Sanjay M. Correa. Carbon monoxide emissions in lean premixed combustion. *Journal of Propulsion and Power*, 8(6):1144–1151, November 1992. ISSN 0748-4658. doi: 10.2514/3.11455.

[12] Sulabh K. Dhanuka, Jacob E. Temme, and James Driscoll. Unsteady aspects of lean premixed prevaporized gas turbine combustors: Flame-flame interactions. *Journal of Propulsion and Power*, 27(3):631–641, May 2011. ISSN 0748-4658. doi: 10.2514/1.B34001.

[13] M. Brandt, K. O. Gugel, and C. Hassa. Experimental investigation of the liquid fuel evaporation in a premix duct for lean premixed and prevaporized combustion. *Journal of Engineering for Gas Turbines and Power*, 119(4):815–821, October 1997. ISSN 0742-4795. doi: 10.1115/1.2817059.

[14] B. Lazaro, E. Gonzalez, J. Alfaro, P. Rodriguez, and A. Lecuona. Turbulent structure of generic lpp gas turbine combustors. *UT0 AVT Symposium on Gas Turbine Engine Combustion, Emissions and Alternative Fuels*, 1998.

[15] J. Fritz, M. Kröner, and T. Sattelmayer. Flashback in a swirl burner with cylindrical premixing zone. *Journal of Engineering for Gas Turbines and Power*, 126(2):276–283, June 2004. ISSN 0742-4795. doi: 10.1115/1.1473155.

[16] Clayton S. Cooper and Normand M. Laurendeau. Quantitative measurements of nitric oxide in high-pressure (2-5 atm), swirl-stabilized

spray flames via laser-induced fluorescence. *Combustion and Flame*, 123:175–188, 2000. ISSN 0010-2180.

[17] D. N. Anderson. Ultra lean combustion at high inlet temperatures. *ASME Paper*, 81-GT(44), 1981.

[18] H. S. Alkabie, G. E. Andrews, and N. T. Ahmad. Lean low nox primary zones using radial swirlers. *ASME Paper*, 88-GT(245), 1988.

[19] S.W. Shaffer and G.S Samuelsen. A liquid fueled, lean burn gas turbine combustor injector. *Combustion Science and Technology*, 139:41–47, 1998.

[20] T. Terasaki and S. Hayashi. Lean non-premixed combustion for low-nox gas turbine combustor. *Yokohama International Gas Turbine Congress*, 1995.

[21] R. Tacina, Chien-Pei Mao, and C. Wey. Experimental investigation of a multiplex fuel injector module for low emission combustors. In *Aerospace Sciences Meetings*. American Institute of Aeronautics and Astronautics, 2003. doi: 10.2514/6.2003-827.

[22] J. Cai, S.-M. Jeng, and R. Tacina. Multi-swirler aerodynamics - experimental measurements. In *Joint Propulsion Conferences*. American Institute of Aeronautics and Astronautics, 2001. doi: 10.2514/6.2001-3574.

[23] R. Tacina, C. Wey, P. Laing, and A. Mansour. Sector tests of a low nox, lean-direct-injection, multipoint integrated module combustor concept. In -, pages –. ASME, 2002.

[24] C. M. Heath, R. Y. Hicks, R. Anderson, and R. J. Locke. *Optical characterization of a multipoint lean direct injector for gas turbine combustors: Velocity and fuel drop size measurements*. National Aeronautics and Space Administration, Glenn Research Center, 2010.

[25] M. Kern, S. Marinov, P. Habisreuther, N. Zarzalis, A. Peschiulli, and F. Turrini. Characteristics of an ultra-lean swirl combustor flow by

les and comparison to measurements. *ASME Conference Proceedings*, GT2011(45300), 2011.

[26] S. Marinov, M. Kern, K. Merkle, N. Zarzalis, A. Peschiulli, and F. Turrini. On swirl stabilized flame characteristics near the weak extinction limit. *ASME Conference Proceedings*, GT2010(22335), 2010.

[27] T. Lieuwen, Y. Neumeier, and B. T. Zinn. The role of unmixedness and chemical kinetics in driving combustion instabilities in lean premixed combustors. *Combustion Science and Technology*, 135(1-6):193–211, June 1998. ISSN 0010-2202. doi: 10.1080/00102209808924157.

[28] T. Schuller, D. Durox, and S. Candel. Self-induced combustion oscillations of laminar premixed flames stabilized on annular burners. *Combustion and Flame*, 135(4):525–537, December 2003. ISSN 0010-2180.

[29] K. R. McManus, T. Poinsot, and S. M. Candel. A review of active control of combustion instabilities. *Progress in Energy and Combustion Science*, 19:1–29, 1993. ISSN 0360-1285.

[30] G. A. Richards, M. Janus, and E. H. Robey. Control of flame oscillations with equivalence ratio modulation. *Journal of Propulsion and Power*, 15(2):232–240, 1999. ISSN 0748-4658. doi: 10.2514/2.5417.

[31] K.T. Padmanabhan, C.T. Bowman, and J.D. Powell. An adaptive optimal combustion control strategy. *Combustion and Flame*, 100:101–110, 1995. ISSN 0010-2180.

[32] L. D. J. Dupère and A. P. Dowling. The use of helmholtz resonators in a practical combustor. *Journal of Engineering for Gas Turbines and Power*, 127(2):268–275, 2005. ISSN 0742-4795. doi: 10.1115/1.1806838.

[33] R. Corà, C. A. Martins, and P. T. Lacava. Acoustic instabilities control using helmholtz resonators. *Applied Acoustics*, 77:1–10, 2014. ISSN 0003-682X.

[34] J. Klaus, I. Bork, M. Graf, and G. P. Ostermeyer. On the adjustment of helmholtz resonators. *Applied Acoustics*, 77:37–41, 2014. ISSN 0003-682X.

[35] C. H. Sohn and J. H. Park. A comparative study on acoustic damping induced by half-wave, quarter-wave, and helmholtz resonators. *Aerospace Science and Technology*, 15(8):606–614, 2011. ISSN 1270-9638.

[36] Sir F. Whittle. *Gas Turbine Aero-Thermodynamics*. Pergamon Press, 1981.

[37] S. M. Correa. Power generation and aeropropulsion gas turbines: From combustion science to combustion technology. *Symposium (International) on Combustion*, 27(2):1793–1807, 1998. ISSN 0082-0784.

[38] D.G. Lilley. Swirl flows in combustion: a review. *AIAA J.*, 15(8), 1977.

[39] O. Lucca-Negro and T. O'Doherty. Vortex breakdown: a review. *Progress in Energy and Combustion Science*, 27(4):431–481, 2001. ISSN 0360-1285.

[40] N. Syred, T. O'Doherty, and D. Froud. The interaction of the precessing vortex core and reverse flow zone in the exhaust of a swirl burner. *Proceedings of the Institution of Mechanical Engineers, Part A: Journal of Power and Energy*, 208:pp. 27–36, 1994.

[41] B.T. Vu and F.C. Gouldin. Flow measurement in a model swirl combustor. *AIAA J.*, 20:pp. 642–651, 1982.

[42] D.L. Rhode, D.G. Lilley, and D.K. McLaughlin. Mean flowfields in axisymmetric combustor geometries with swirl. *AIAA J.*, 21:pp. 593–600, 1983.

[43] G.B. Ferrell, M.T. Abujelala, A.A. Busnaina, and D.G. Lilley. Lateral jet injection into typical combustor flowfields. *AIAA 22nd Aerospace Sciences Meeting, Reno, NV, Jan.*, 1984.

[44] A. Spencer, D. Hollis, and J. Carrotte. Piv measurements of combustor turbulence fields. *ASME Conference Proceedings*, GT2007(28050), 2007.

[45] A. Spencer, D. Hollis, and S. Gashi. Investigation of the unsteady aerodynamics of an annular combustor using piv and les. *ASME Conference Proceedings*, GT2008(50277), 2008.

[46] M. Gnirb and C. Tropea. Simultaneous piv and concentration measurements in a gas-turbine combustor model. *Exp Fluids*, 45(4):643–656, 2008. ISSN 0723-4864.

[47] B. Wurm, A. Schulz, and H.J. Bauer. A new test facility for investigating the interaction between swirl flow and wall cooling films in combustors. *ASME Conference Proceedings*, GT2009(59961), 2009.

[48] E.V. Shisnova, P.S. Roganova, S.I. Grabarnika, and V.P. Zabolotskya. Heat transfer in the recirculating region formed by a backward-facing step. *International Journal of Heat and Mass Transfer*, 31:1557–1562, 1988.

[49] J. C. Vogel and J. K. Eaton. Combined heat transfer and fluid dynamic measurements downstream of a backward-facing step. *International Journal of Heat and Mass Transfer*, 107:922–929, 1985.

[50] A.K. Pozarlik, D. Panara, J.B.W. Kok, and T.H. van der Meer. Heat transfer in a recirculation zone at steady-state and oscillating conditions-the back facing step test case. *5th European Thermal-Sciences Conference*, 2008.

[51] S. Patil, T. Sedalor, D. Tafti, S. Ekkad, Y. Kim, P. Dutta, H.K. Moon, and R. Srinivasan. Study of flow and convective heat transfer in a simulated scaled up low emission annular combustor. *Journal of Thermal Science and Engineering Applications*, 3, 2011. doi: 10.1115/1.4004531.

[52] H. Memar, J.P. Holman, and P.A. Dellenback. The effect of a swirled annular jet on convective heat transfer in confined coaxial jet mixing.

International Journal of Heat and Mass Transfer, 36(16):3921–3930, 1993. ISSN 0017-9310.

[53] A. Schulz. Combustor liner cooling technology in scope of reduced pollutant formation and rising thermal efficiencies. *Annals of the New York Academy of Sciences*, 934(1):135–146, May 2001. ISSN 1749-6632.

[54] F. Moskal. Manufacturing of effusion cooled combustors. *SAE Technical Paper 911141*, 1991. doi: 10.4271/911141.

[55] R. Krewinkel. A review of gas turbine effusion cooling studies. *International Journal of Heat and Mass Transfer*, 66(0):706–722, November 2013. ISSN 0017-9310.

[56] K. M. B. Gustafsson and T.G. Johansson. An experimental study of surface temperature distribution on effusion-cooled plates. *ASME Journal of Engineering for Gas Turbine and Power*, 123:308–316, 2001.

[57] A. Andreini, G. Caciolli, B. Facchini, and L. Tarchi. Experimental evaluation of the density ratio effects on the cooling performance of a combined slot/effusion combustor cooling system. *ISRN Aerospace Engineering*, 2013:14, 2013. doi: 10.1155/2013/423190.

[58] P. D. Dean. Duct wall impedance control as an advanced concept for acoustic suppression enhancement. Technical Report 7903, National Aeronautics and Space Administration, Oct 1978.

[59] V. Bellucci, P. Flohr, and C. Paschereit. Impedance of perforated screen with bias flow. *AIAA Paper*, pages 2002 – 2437, 2002.

[60] J. Rupp, J. Carrotte, and A. Spencer. Interaction between the acoustic pressure fluctuations and the unsteady flow field through circular holes. *Journal of Engineering for Gas Turbines and Power*, 132(6):061501–061501, March 2010. ISSN 0742-4795. doi: 10.1115/1.4000114.

[61] J. Eldredge and A. Dowling. The absorption of axial acoustic waves by a perforated liner with bias flow. *Journal of Fluid Mechanics*, 485: 307–335, 2003.

[62] C. Heuwinkel, L. Enghardt, F. Bake, S. Sadig, and M. Gerendás. Establishment of a high quality database for the modelling of perforated liners. *ASME Conference Proceedings*, GT2010(43970):247–258, 2010. doi: 10.1115/GT2010-22329.

[63] A. Andreini, B. Facchini, L. Ferrari, G. Lenzi, F. Simonetti, and A. Peschiulli. Experimental investigation on effusion liner geometries for aero-engine combustors: Evaluation of global acoustic parameters. *ASME Conference Proceedings*, GT2012(6983), 2012.

[64] R. J. Goldstein. Film cooling. *Advances in Heat transfer*, 7:321–379, 1971.

[65] B. Lakshminarayana. *Fluid Dynamics and Heat Transfer of Turbomachinery*. John Wiley & Sons, Inc., 1996.

[66] B. Sen, D. L. Schmidt, and D. G. Bogard. Film cooling with compound angle holes: Heat transfer. *ASME J. Turbomach*, 118:800–806, 1996.

[67] D.E. Metzger, D.I. Takeuchi, and P.A. Kuenstler. Effectiveness and heat transfer with full-coverage film cooling. *ASME Journal of Engineering for Power*, 95:180–184, 1973.

[68] G. B. Kelly and D. G. Bogard. An investigation of the heat transfer for full coverage film cooling. *ASME Turbo Expo*, GT2003(38716), 2003.

[69] M. Sasaki, K. Takahara, T. Kumagai, and M. Hamano. Film cooling effectiveness for injection from multirow holes. *ASME Transactions Journal of Engineering Power*, 101:101–108, January 1979.

[70] R. E. Mayle and F. J. Camarata. Multihole cooling film effectiveness and heat transfer. *ASME Journal of Heat Transfer*, 97, 1975.

[71] G. E. Andrews, A. A. Asere, M. L. Gupta, and M. C. Mkpadi. Effusion cooling: the influence of number of hole. *Journal of Power and Energy*, 204, 1990.

[72] G. E. Andrews, F. Bazdidi-Tehrani, C. I. Hussain, and J. P. Pearson. Small diameter film cooling hole heat transfer: The influence of hole length. *ASME Paper*, 91-GT(344), 1991.

[73] M. K. Harrington, M. A. McWaters, D. G. Bogard, C. A. Lemmon, and K. A. Thole. Full-coverage film cooling with short normal injection holes. *ASME J. Turbomach*, 123:798–805, 2001.

[74] J. J. Scrittore, K. A. Thole, and S. W. Burd. Experimental characterization of film-cooling effectiveness near combustor dilution holes. *ASME Turbo Expo*, GT2005(68704), 2005.

[75] J. J. Scrittore, K. A. Thole, and S. W. Burd. Investigation of velocity profiles for effusion cooling of a combustor liner. *ASME Turbo Expo*, GT2006(90532), 2006.

[76] L. Arcangeli, B. Facchini, M. Surace, and L. Tarchi. Correlative analysis of effusion cooling systems. *ASME J. Turbomach*, 130(011016), 2008.

[77] P. Ligrani, M. Goodro, M. Fox, and Hee-Koo Moon. Full-coverage film cooling: Film effectiveness and heat transfer coefficients for dense and sparse hole arrays at different blowing ratios. *J TURBOMACH*, 134 (6):061039, 2012. doi: 10.1115/1.4006304.

[78] A. Martin and S. J. Thorpe. Experiments on combustor effusion cooling under conditions of very high free-stream turbulence. *ASME Conference Proceedings*, GT2012(68863), 2012.

[79] A. Ceccherini, B. Facchini, L. Tarchi, and L. Toni. Combined effect of slot injection, effusion array and dilution hole on the cooling performance of a real combustor liner. *ASME Turbo Expo*, GT2009(60047), 2009.

[80] Y. Lin, B. Song, B. Li, G. Liu, and Z. Wu. Investigation of film cooling effectiveness of full-coverage inclined multihole walls with different hole arrangements. *ASME Turbo Expo*, GT2003(38881), 2003.

[81] F. Maiuolo, B. Facchini, L. Tarchi, and D. Coutandin. Experimental investigation on the effects of a large recirculating area on the performance of an effusion cooled combustor liner. *Journal of Engineering for Gas Turbines and Power*, 134:041505–1–9, 2012.

[82] B. Wurm, A. Schulz, H.-J. Bauer, and M. Gerendas. Impact of swirl flow on the cooling performance of an effusion cooled combustor liner. *Journal of Engineering for Gas Turbines and Power*, 134(12):121503–121503, October 2012. ISSN 0742-4795. doi: 10.1115/1.4007332.

[83] B. Wurm, A. Schulz, H. J. Bauer, and M. Gerendas. Cooling efficiency for assessing the cooling performance of an effusion cooled combustor liner. *ASME Turbo Expo*, GT2013(94304), 2013.

[84] M.Raffel, C.E. Willert, and J. Kompenhans. *Particle Image Velocimetry - A Pratical Guide.* Springer, 2nd edition, 2007.

[85] R. D. Keane and R. J. Adrian. Theory of cross-correlation analysis of piv images. *Flow, Turbulence and Combustion*, 49(3):191–215, 1992. ISSN 0003-6994.

[86] K. R. Navarra. *Development of the Pressure-Sensitive-Paint Technique for Turbomachinery Applications.* Virginia Polytechnic Institute and State University, 1997.

[87] M. Jonsson. *Application of Photoluminescent Measurement Techniques for Quantitative Assessment of Turbine Film Cooling.* PhD thesis, École Polytechnique Fédérale De Lausanne, 2010.

[88] D. P. Narzary, K. C. Liu, A. P. Rallabandi, and J. C. Han. Influence of coolant density on turbine blade film-cooling using pressure sensitive paint technique. *Journal of Turbomachinery*, 134(3):031006–031006, July 2011. ISSN 0889-504X. doi: 10.1115/1.4003025.

[89] J. C. Han and P. Rallabandi. Turbine blade film cooling using psp technique. *Frontiers in Heat and Mass Transfer*, 1, 2010.

[90] R.J. Goldstein and H.H. Cho. A review of mass transfer measurements using naphthalene sublimation. *Experimental Thermal and Fluid Science*, 10(4):416 – 434, 1995. ISSN 0894-1777. doi: 10.1016/0894-1777(94)00071-F.

[91] R. L. Simpson and R. L. Field. A note on the turbulent schmidt and lewis numbers in a boundary layer. *International Journal of Heat and Mass Transfer*, 15:177–180, 1972.

[92] D. Charbonnier, P. Ott, M. Jonsson, F. Cottier, and T. Köbke. Experimental and numerical study of the thermal performance of a film cooled turbine platform. *ASME Conference Proceedings*, GT2009(60306): 1027–1038, 2009. doi: 10.1115/GT2009-60306.

[93] J.Ahn, M. T. Schobeiri, J. C. Han, and H. K. Moon. Film cooling effectiveness on the leading edge of a rotating turbine blade. *ASME Conference Proceedings*, GT2004(59852):565–574, 2004. doi: 10.1115/IMECE2004-59852.

[94] B. Facchini, A. Picchi, L. Tarchi, A. Ciani, M. D'Ercole, and L. Innocenti. Film-cooling adiabatic effectiveness measurements on a real high pressure turbine blade. *10th European Turbomachinery Conference*, ETC2013(143), 2013.

[95] T. V. Jones. Theory for the use of foreign gas in simulating film cooling. *International Journal of Heat and Fluid Flow*, 20:349–354, 1999.

[96] J. C. Han, S. Dutta, and S. Ekkad. *Gas Turbine Heat Transfer and Cooling Technology*. Taylor & Francis, 2000.

[97] L. M. Wright, Z. Gao, T. A. Varvel, and J. C. Han. Assessment of steady state psp, tsp, and ir measurement techniques for flat plate film cooling. *ASME Conference Proceedings*, HT2005-72363(47330):37–46, 2005. doi: 10.1115/HT2005-72363.

[98] G. Caciolli, B. Facchini, A. Picchi, and L. Tarchi. Comparison between psp and tlc steady state techniques for adiabatic effectiveness

measurement on a multiperforated plate. *Experimental Thermal and Fluid Science*, 48(0):122–133, July 2013. ISSN 0894-1777.

[99] A. Ceccherini, B. Facchini, L. Tarchi, and L. Toni. Adiabatic and overall effectiveness measurements of an effusion cooling array for turbine endwall application. *ASME Turbo Expo*, GT2008(50826), 2008.

[100] H. I. Oguntade, G. E. Andrews, A. D. Burns, D. B. Ingham, and M. Pourkashanian. Conjugate heat transfer predictions of effusion cooling: The influence of the coolant jet-flow direction on the cooling effectiveness. *ASME Conference Proceedings*, GT2012(68517), 2012.

[101] J.L. Hay and D.K. Hollingsworth. A comparison of trichromic systems for use in the calibration of polymer-dispersed thermochromic liquid crystals. *Experimental Thermal and Fluid Science*, 12(1):1–12, January 1996. ISSN 0894-1777.

[102] T. L. Chan, S. Ashforth-Frost, and K. Jambunathan. Calibrating for viewing angle effect during heat transfer measurements on a curved surface. *International Journal of Heat and Mass Transfer*, 44:2209–2223, 2001.

[103] D. J. Farina, J. M. Hacker, R. J. Moffat, and J. K. Eaton. Illuminant invariant calibration of thermochromic liquid crystals. *Experimental Thermal and Fluid Science*, 9(1):1 – 12, 1994. ISSN 0894-1777. doi: 10.1016/0894-1777(94)90002-7.

[104] S. Baldauf, M. Scheurlen, A. Schulz, and S. Wittig. Heat flux reduction from film cooling and correlation of heat transfer coefficients from thermographic measurements at enginelike conditions. *J TURBOMACH*, 124(4):699–709, 2002. doi: 10.1115/1.1505848.

[105] S. Bell. *A Beginner's Guide to Uncertainty of Measurement.* NPL National Physical Laboratory, 1999.

[106] S. J. Kline and F. A. McClintock. Describing uncertainties in single sample experiments. *Mechanical Engineering*, 75:3–8, Jan 1953.

[107] Ente Nazionale di Unificazione UNI. *Measurerement of fluid flow by means of pressure differential devices*, volume UNI EN ISO 5167-1. UNI, sept 1997.

[108] A. C. Nix, A. C. Smith, T. E. Diller, W.F. Ng, and K. A. Thole. High intensity, large length-scale freestream turbulence generation in a transonic turbine cascade. *ASME Conference Proceedings*, GT2002 (30523), 2002.

[109] P.E. Roach. The generation of nearly isotropic turbulence by means of grids. *International Journal of Heat and Fluid Flow*, 8(2):82 – 92, 1987. ISSN 0142-727X. doi: 10.1016/0142-727X(87)90001-4.

[110] H. H. Cho and R. J. Goldstein. Heat (mass) transfer and film cooling effectiveness with injection through discrete holes: Part i-within holes and on the back surface. *J TURBOMACH*, 117(3):440–450, 1995. doi: 10.1115/1.2835680.

[111] B. Facchini, F. Maiuolo, L. Tarchi, and D. Coutandin. Combined effect of slot injection, effusion array and dilution hole on the heat transfer coefficient of a real combustor liner: Part 1—experimental analysis. *ASME Conference Proceedings*, GT2010(22936):753–762, 2010. doi: 10.1115/GT2010-22936.

[112] J. E. Mayhew, J. W. Baughn, and A. R. Byerley. The effect of freestream turbulence on film cooling adiabatic effectiveness. *International Journal of Heat and Fluid Flow*, 24(5):669 – 679, 2003. doi: 10.1016/S0142-727X(03)00081-X.

[113] M. R. L'Ecuyer and F. O. Soechting. A model for correlating flat plate film cooling effectiveness for rows of round holes. *AGARD conference proceedings*, 1985(390):19.1–19.12, 1985. ISSN 0549-7191.

[114] J. P. Bons, C. D. MacArthur, and R. B. Rivir. The effect of high freestream turbulence on film cooling effectiveness. *J TURBOMACH*, 118 (4):814–825, 1996. doi: 10.1115/1.2840939.

[115] F. P. Incropera, D. P. DeWitt, L. T. Bergman, and A. S. Lavine. *Fundamentals of Heat and Mass Transfer*. Wiley & Sons, 2006.

[116] A. Andreini, C. Carcasci, A. Ceccherini, B. Facchini, M. Surace, D. Coutandin, S. Gori, and A. Peschiulli. Combustor liner temperature prediction: a preliminary tool development and its application on effusion cooling systems. *First CEAS European Air and Space Conference Century Perspectives*, 2007(Paper n.026), 2007.

[117] A. Andreini, A. Ceccherini, B. Facchini, F. Turrini, and I. Vitale. Assessment of a set of numerical tools for the design of aero-engines combustors: Study of a tubular test rig. *ASME Conference Proceedings*, 2009(48838):421–433, 2009. doi: 10.1115/GT2009-59539.

[118] E. Dorignac, J.-J. Vullierme, M. Broussely, C. Foulon, and M. Mokkadem. Experimental heat transfer on the windward surface of a perforated flat plate. *International Journal of Thermal Sciences*, 44(9):885 – 893, 2005. doi: 10.1016/j.ijthermalsci.2004.11.012.

[119] L. Toni. *Gas Turbine Aero-Engines Effusion Cooling Systems*. PhD thesis, Industrial Engineering and Energy Engineering University of Florence, 2008.

[120] M. Gritsch, A. Schulz, and S. Wittig. Effect of crossflows on the discharge coefficient of film cooling holes with varying angles of inclination and orientation. *ASME J. Turbomach*, 123:781–787, 2001.

[121] K. A. Thole, M. Gritsch, A. Schulz, and S. Wittig. Effect of a crossflow at the entrance to a film-cooling hole. *Journal of Fluids Engineering*, 119(3):533–540, September 1997. ISSN 0098-2202. doi: 10.1115/1.2819277.

[122] M. Martiny, A. Schulz, and S. Wittig. Full-coverage film cooling investigations: adiabatic wall temperatures and flow visualization. *ASME Conference Proceedings*, 95(WA/HT-4), 1995.

[123] V. U. Kakade, S. J. Thorpe, and M. Gerendas. Effusion-cooling performance at gas turbine combustor representative flow conditions. *ASME Conference Proceedings*, GT2012(68115), 2012.

[124] U. Bhayaraju, J. Schmidt, K. Kashinath, and S. Hochgreb. Effect of cooling liner on acoustic energy absorption and flame response. *ASME Con*, GT2010(22616), 2010.

[125] T. Behrendt and M. Gerendas. Characterization of the influence of moderate pressure fluctuations on the cooling performance of advanced combustor cooling concepts in a reacting flow. *ASME Conference Proceedings*, GT2012(68845), 2012.

[126] Q. Yang, Y. Lin, Q. Xu, C. Zhang, and Chih-Jen Sung. Cooling effectiveness of impingement/effusion cooling with and without turbulence promoter ribs. *ASME Conference Proceedings*, GT2012(69209), 2012.

[127] A. Andreini, B. Facchini, L. Mazzei, L. Bellocci, and F. Turrini. Assessment of aero-thermal design methodology for effusion cooled lean burn annular combustors. *ASME Conference Proceedings (IN PRESS)*, GT2014(26764), 2014.

[128] R. Becchi. Experimental analysis of the flow field of an aeronautic combustor injector: Effects on the heat exchange with liner wall (in italian). Master's thesis, Univeristy of Florence Ingegneria Energetica, 2013.

[129] S. Patil, S. Abraham, D. Tafti, S. Ekkad, Y. Kim, P. Dutta, H.K. Moon, and R. Srinivasan. Experimental and numerical investigation of convective heat transfer in a gas turbine can combustor. *J. TURBOMACH*, 133, 2011. doi: 10.1115/1.4001173.

[130] A. Ceccherini, B. Facchini, L. Tarchi, L. Toni, and D. Coutandin. Combined effect of slot injection, effusion array and dilution hole on the cooling performance of a real combustor liner. *ASME Conference Proceedings*, 2009(48845):1431–1440, 2009. doi: 10.1115/GT2009-60047.